COLLEGE PARK CAMPUS

POLLUTION ERROR IN THE h-VERSION OF THE FINITE ELEMENT METHOD AND THE LOCAL QUALITY OF A-POSTERIORI ERROR ESTIMATORS

by

I. Babuška
T. Strouboulis
A. Mathur
C. S. Upadhyay

Technical Note BN-1163

and

CMC Report No. 94-01
Texas Engineering Experiment Station
The Texas A&M University System

February 1994

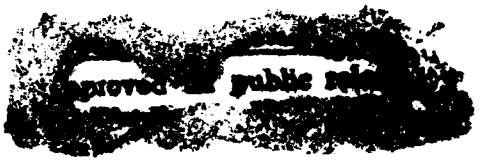

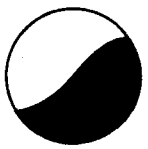

INSTITUTE FOR PHYSICAL SCIENCE
AND TECHNOLOGY

SECURITY CLASSIFICATION OF THIS PAGE (When Data Entered)

REPORT DOCUMENTATION PAGE

READ INSTRUCTIONS BEFORE COMPLETING FORM

1. REPORT NUMBER: Technical Note BN-1163	2. GOVT ACCESSION NO.
3. RECIPIENT'S CATALOG NUMBER	
4. TITLE (and Subtitle): Pollution Error in the h-Version of the Finite Element Method and the Local Quality of A-Posteriori Error Estimators	5. TYPE OF REPORT & PERIOD COVERED: Final Life of Contract
6. PERFORMING ORG. REPORT NUMBER	
7. AUTHOR(s): [1]I. Babuska - [2]T. Strouboulis, A. Mathur and C. S. Upadhyay	8. CONTRACT OR GRANT NUMBER(s): [1]N00014-90-J-1030/ONR CCR-88-20279/NSF [2]See Page 1
9. PERFORMING ORGANIZATION NAME AND ADDRESS: Institute for Physical Science and Technology, University of Maryland, College Park, MD 20742-2431	10. PROGRAM ELEMENT, PROJECT, TASK AREA & WORK UNIT NUMBERS
11. CONTROLLING OFFICE NAME AND ADDRESS: Department of the Navy, Office of Naval Research, Arlington, VA 22217	12. REPORT DATE: February 1994
	13. NUMBER OF PAGES: 159
14. MONITORING AGENCY NAME & ADDRESS(if different from Controlling Office)	15. SECURITY CLASS. (of this report)
	15a. DECLASSIFICATION/DOWNGRADING SCHEDULE

16. DISTRIBUTION STATEMENT (of this Report)

Approved for public release: distribution unlimited

17. DISTRIBUTION STATEMENT (of the abstract entered in Block 20, if different from Report)

18. SUPPLEMENTARY NOTES

19. KEY WORDS (Continue on reverse side if necessary and identify by block number)

20. ABSTRACT

In this work we study the pollution-error in the *h*-version of the finite element method and its effect on the local quality of a-posteriori error estimators. We show that the pollution-effect in an interior subdomain depends on the relationship between the mesh inside and outside the subdomain and the smoothness of the exact solution. We also demonstrate that it is possible to guarantee the quality of local error-estimators in the interior of a finite-element mesh-patch of interest by employing meshes which are sufficiently refined outside the patch.

DD FORM 1 JAN 73 1473 EDITION OF 1 NOV 65 IS OBSOLETE

S N 0102-LF-014-6601

SECURITY CLASSIFICATION OF THIS PAGE (When Data Entered)

Pollution Error in the h-Version of the Finite Element Method and the Local Quality of A-Posteriori Error Estimators

I. Babuška[1]
Institute for Physical Science and Technology and Department of Mathematics,
University of Maryland, College Park, MD 20742, U.S.A.

T. Strouboulis[2], A. Mathur[2] and C.S. Upadhyay[2]
Department of Aerospace Engineering, Texas A&M University,
College Station, TX 77843, U.S.A.

February 1994

[1]The work of this author was supported by the U.S. Office of Naval Research under Contract N00014-90-J-1030 and by the National Science Foundation under Grant CCR-88-20279.

[2]The work of these authors was supported by the U.S. Army Research Office under Grant DAAL03-G-028, by the National Science Foundation under Grant MSS-9025110 and by the Texas Advanced Research Program under Grant TARP-71071.

Abstract

In this work we study the pollution-error in the h-version of the finite element method and its effect on the local quality of a-posteriori error estimators. We show that the pollution-effect in an interior subdomain depends on the relationship between the mesh inside and outside the subdomain and the smoothness of the exact solution. We also demonstrate that it is possible to guarantee the quality of local error-estimators in the interior of a finite-element mesh-patch of interest by employing meshes which are sufficiently refined outside the patch.

1 Introduction

The design and certification procedures for aerospace structures require an accurate stress analysis capability. Detailed stress analyses of complex aircraft structures and their subcomponents are required, especially during the certification phase of the analysis. The finite element method has become the method of choice for the analysis of complex structures such as aircraft, nuclear power plant components and automobiles. Before manufacturing a component, the designer must be able to predict its behavior. This prediction is based on a formulation of a mathematical model, its computational analysis, experiments, and experience with existing constructions and their failures. Because of various uncertainties which necessarily occur, the goals of advanced design analyses (in aircraft, nuclear industries, etc.) are often stipulated in the design codes (which are changing over time). The question of the principles of safety is directly related to these codes. For example, in the design code USAF-MIL-A-83444, used in military aircraft design, it is required that components based on the principles of "non-inspectable slow crack growth" must be designed under the assumption that,

a) the as-fabricated structure contains flaws of a size just smaller than the non-destructive maximum undetectable flaw-size;

b) the flaws are assumed to exist in the form of crack-like defects with most unfavorable location and orientation.

The design code requires that the mathematical formulation and its computational analysis must reliably and conservatively predict both the sizes of the growing cracks and the residual strength of the component.

As a result of the requirements of the design code many times it becomes necessary to analyze a small portion of the structure, such as a stress critical component, in greater detail, e.g. the fuselage of an aircraft may be subjected to accurate analysis in the neighborhood of structural details like openings, cracks, etc. A standard procedure is to analyze the entire structure using a global discretization which is often referred to as *global analysis* and to further analyze the structure near critical regions, identified by the global analysis, by performing *local analyses*. Such procedures, which are known as *global/local analysis*, are becoming quite popular in engineering practice.

1.1 Generalities about global/local analysis

We would like to discuss further some of the ideas involved in the technologies of global/local analysis. In the literature of global/local analysis one often encounters the terms *global model* and *local model*. We would now like to comment on the meaning of the word *model* which is often used with different meanings in the

engineering community. There are two interpretations of the finite element method (see also [1]). The first one considers the method as an extension of the standard method of structural analysis in which the original (physical) problem is replaced by another (physical) problem which is finite dimensional and can be computationally analyzed. For example, in the late 50's it was common practice to "model" the two-dimensional elastic continuum by a system of trusses connected by shear-panels. This physical "modelling" method was called *finite element modelling*. The second interpretation is to understand the finite element method as an *approximation method* for solving mathematical problems. The second interpretation is the main interpretation today, although the (misleading) term "finite element modelling" is still used, especially in engineering. *A model is a continuous mathematical problem and is approximated by a finite element method which employs meshes.*

It follows from the above discussion that, if the same mathematical model is solved during the global and the local analysis, the terms "global model" and "local model" are misleading; instead the terms *global mesh* and *local mesh* must be used. The objective of global/local analyses of this type is to obtain accurate approximations of the solution quantities of engineering importance (stresses, thermal fluxes) in local regions of interest, or, in other words, *to obtain an approximate solution of the mathematical model with error less than a specified tolerance in the region of interest (for a measure of error which is dictated by the goals of the analysis)*.

It is also possible to attach another meaning to the term global/local analysis. For example a 3-D (three-dimensional) elastic continuum in a thin domain may be analyzed using different plate models in different regions in order to meet desired levels of accuracy with respect to the exact solution of the problem of 3-D elasticity. In this case the terms "global model" and "local model" may be appropriate. This methodology is known as *hierarchical modelling* [1, 2, 3, 4, 5] and its objectives are to approximate the solution of an exact mathematical model (for example the problem of 3-D elasticity) by employing solutions of approximate mathematical models (e.g. plate or shell theories) in order to meet specified error tolerances with respect to the solution of the exact mathematical model, in the regions of interest. The approximate models are continuous mathematical problems which are derived from the exact mathematical model using certain simplifying assumptions.

As discussed above, the term global/local analysis has been employed in two different contexts in practical engineering computations.

(1) In one context, the global and local analyses are refined or enriched mesh-techniques often employed in order to approximate the solution of a single mathematical model throughout the domain. An example of this type of analysis is given in [6]: In that work a methodology is outlined in which a relatively coarse global mesh is used to analyze a complex structure. The critical regions requiring a more detailed analysis are subsequently identified and interpolation regions are then defined around these regions and an interpolation procedure is employed to determine the boundary conditions for the

local meshes. The local meshes which lie within the interpolation region are independent of the global mesh and are more refined than the global mesh. In some analyses of this type the discrete problems in the local meshes may be also fully coupled with the discrete problem in the global mesh.

(2) In another context, the global and local analyses are performed by solving different mathematical problems in different parts of the domain. In [7] such an approach was employed in order to resolve crack-tip fields in fibrous composites. This technique which in [7] is called the *mesh-superposition method* may be described as follows: A composite plate, which may include cracks, is first analyzed as a homogeneous orthotropic continuum using a finite element mesh which is called the *macro-mesh*. The local behavior on the scale of the heterogeneous constituents is then analyzed using a separate finite-element mesh called the *micro-mesh* which employs elements which are small enough to reflect the micro variations in material behavior and is superimposed on the macro-mesh in the neighborhoods of the crack-tips where the critical behavior is expected.

From a study of the literature it is clear that the emphasis of the research in global/local analysis has been on:

(i). Postprocessing the results of the global analysis in order to determine the subregions requiring detailed analysis;

(ii). Generating refined and/or enriched meshes in the local areas of interest;

(iii). Imposing interface-conditions at the interface between the global and local meshes (or global and local mathematical models);

(iv). Developing solutions strategies for the linear algebra problems which result in this type of analyses.

Very little attention has been paid on ensuring good quality (i.e. accuracy) of the finite element solution in the region of interest.

In this paper we will demonstrate that the accuracy of the approximate solution in a subdomain of interest depends on the relationship between the mesh used inside and outside the subdomain where the detailed analysis is required or in other words *accuracy of the local analyses depends on the accuracy of the global analysis.*

To illustrate this point we give the following example: Let us consider Laplace's equation in the L-shaped domain shown in Figs. 1a-1d with boundary conditions consistent with the singular solution $u(r,\theta) = r^{\frac{1}{3}} \sin(\frac{\theta}{3})$ in the infinite wedge (see also Section 2). We assumed that we are interested only in the solution in the hollow square subdomain, which is shown with thick perigram in the upper right corner of the domain in Figs. 1a-1d. We computed finite-element solutions of the

Laplacian using the standard displacement method and we employed four meshes of linear elements, as shown in Figs. 1a-1d. In these meshes the grid in the subdomain was kept fixed while the mesh employed outside the subdomain was coarsened in order to illustrate the effect of the outside grid on the accuracy of the finite-element solution in the subdomain. In Fig. 1.1a we show an adaptive finite-element mesh of linear elements which was generated using a remeshing algorithm, over the domain. For this mesh an accuracy of 1.09% for the relative error in the energy-norm over the subdomain was achieved in the hollow square subdomain. In Figs. 1.1b, 1.1c, 1.1d we show grids in which the mesh outside the subdomain was progressively coarsened while the mesh inside the subdomain was kept fixed as in Fig. 1a. Using the grids shown in Figs. 1.1b, 1.1c and 1.1d we computed approximate solutions for Laplace's equation and we found that the exact relative error in the energy norm over the subdomain is 4.67%, 12.24% and 23.9%, respectively.

From this example, it is clear that the accuracy of the finite-element solution in any subdomain depends on the mesh outside the subdomain and that *in order to increase the accuracy of the finite-element solution in a subdomain of interest one has to employ meshes which are sufficiently refined inside and outside the subdomain*. Hence, in general *we cannot say that a refined mesh in a subdomain can guarantee a better solution in the interior of the subdomain*. The situation is very similar, but more complex, in the case of hierarchical modelling and will not be addressed here.

Based on these initial observations it is clear that if a detailed analysis is carried out by employing a refined or enriched mesh in a local region of interest with no regard to the mesh outside that region, no gain in the local accuracy may be obtained. Hence the idea of global/local analysis makes sense only if it is based on *algorithms which achieve the desired accuracy in regions of interest by controlling the relationship between the inside and outside meshes in order to employ nearly minimal total number of degrees of freedom*. The objective of this work is to make initial progress towards this goal.

1.2 Introductory remarks about error estimation

A-posteriori error estimation is the only rational means for checking the local quality of approximate solutions. Therefore it is important to know *under what conditions the error estimators are reliable and how to design the meshes in order to guarantee the reliability of local error-estimation*.

The design and verification of error estimators for approximate solutions of elliptic boundary-value problems has been the focus of intensive research; see for example [8-43] and the citations in these papers. Studies of the factors which affect the local quality of error estimators are given in [41-45]. These factors are:

1. *The geometry of the grid*: By geometry we mean the *topology* of the grid

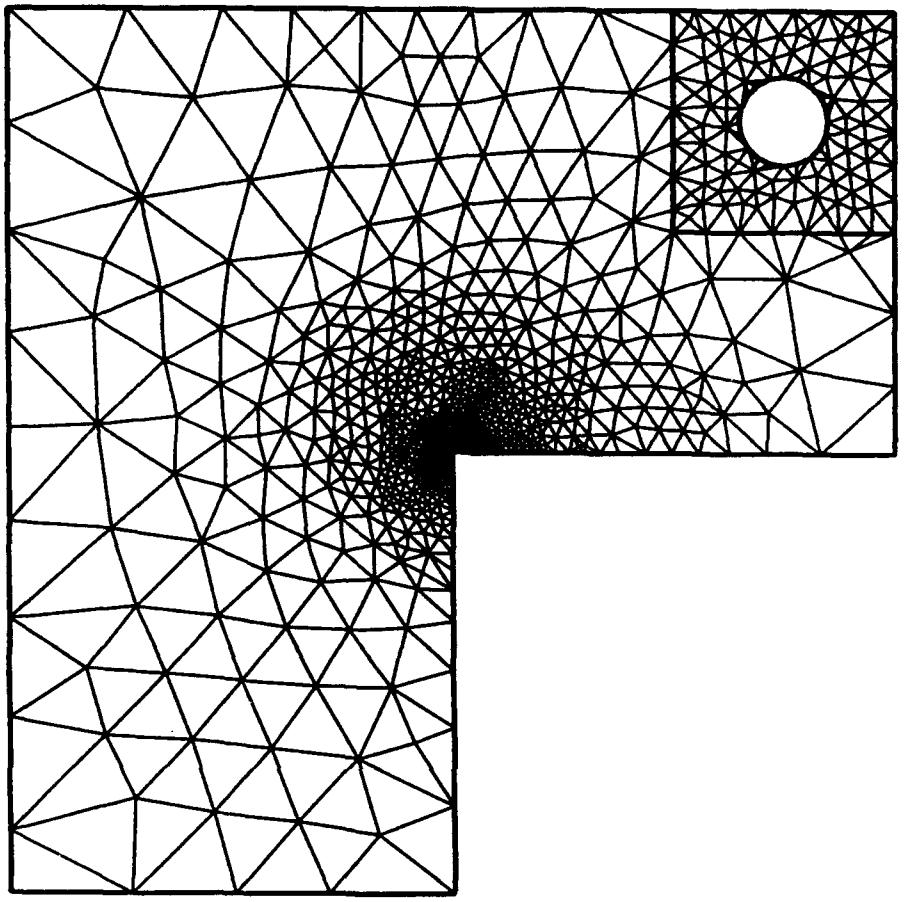

(a)

Figure 1.1. Effect of the outside grid on the accuracy of the finite-element solution in a region of interest. The hollow subdomain is shown with black perigram in the upper right corner of the L-shaped domain. The subdomain was meshed with a quasi-uniform mesh which was kept fixed while various meshes were employed in the rest of domain. (a) A mesh for which an accuracy of 1.09% was achieved in the subdomain. (b) A mesh for which an accuracy of 4.67% was achieved in the subdomain. (c) A mesh for which an accuracy of 12.24% was achieved in the subdomain. (d) A mesh for which an accuracy of 23.97% was achieved in the subdomain. It is clear that the accuracy of the finite-element solution in the subdomain depends strongly on the mesh outside the subdomain.

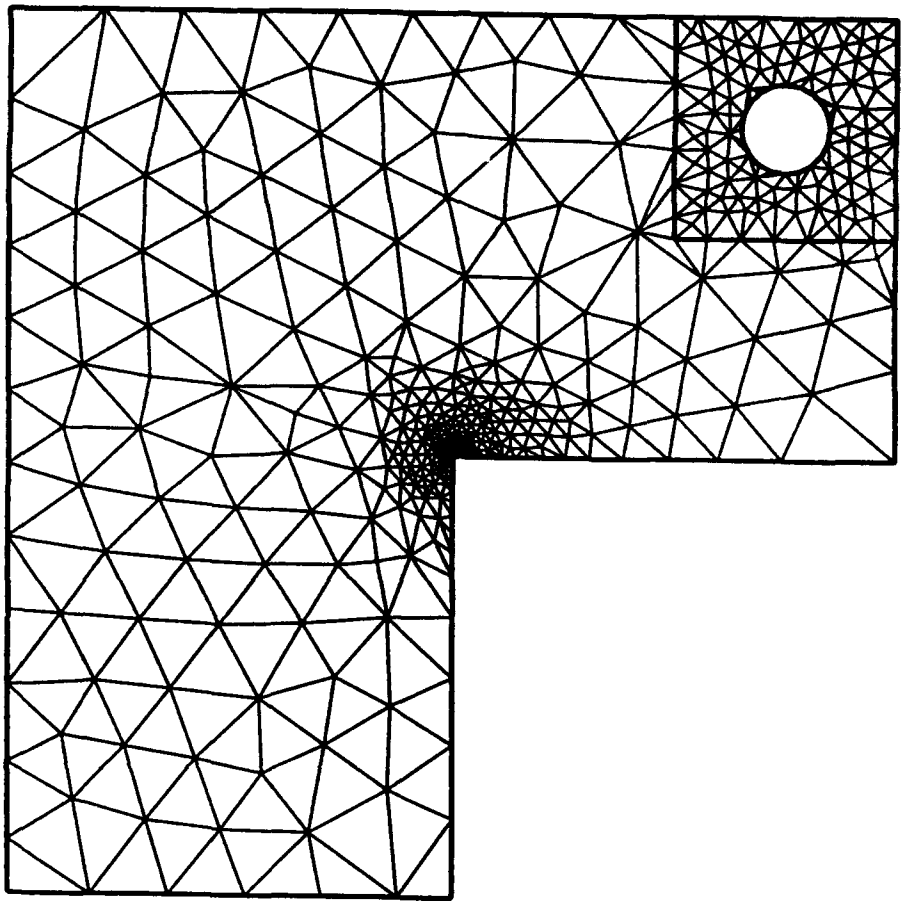

(b)

Figure 1.1 (continued)

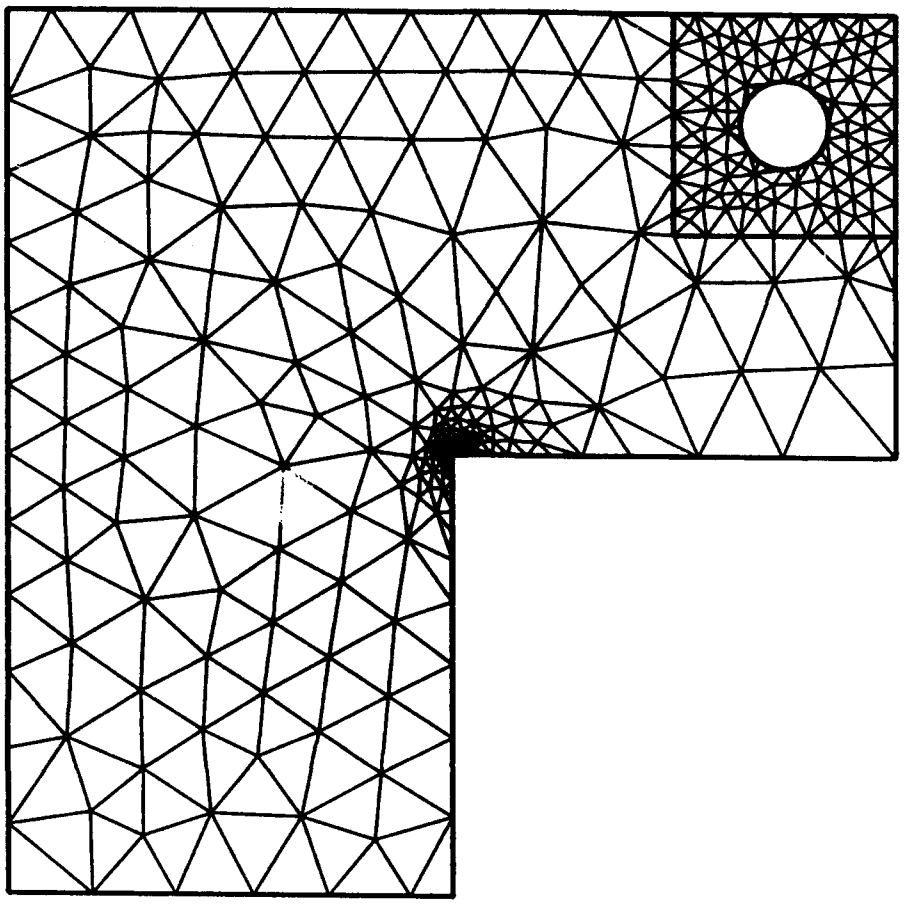

(c)

Figure 1.1 (continued)

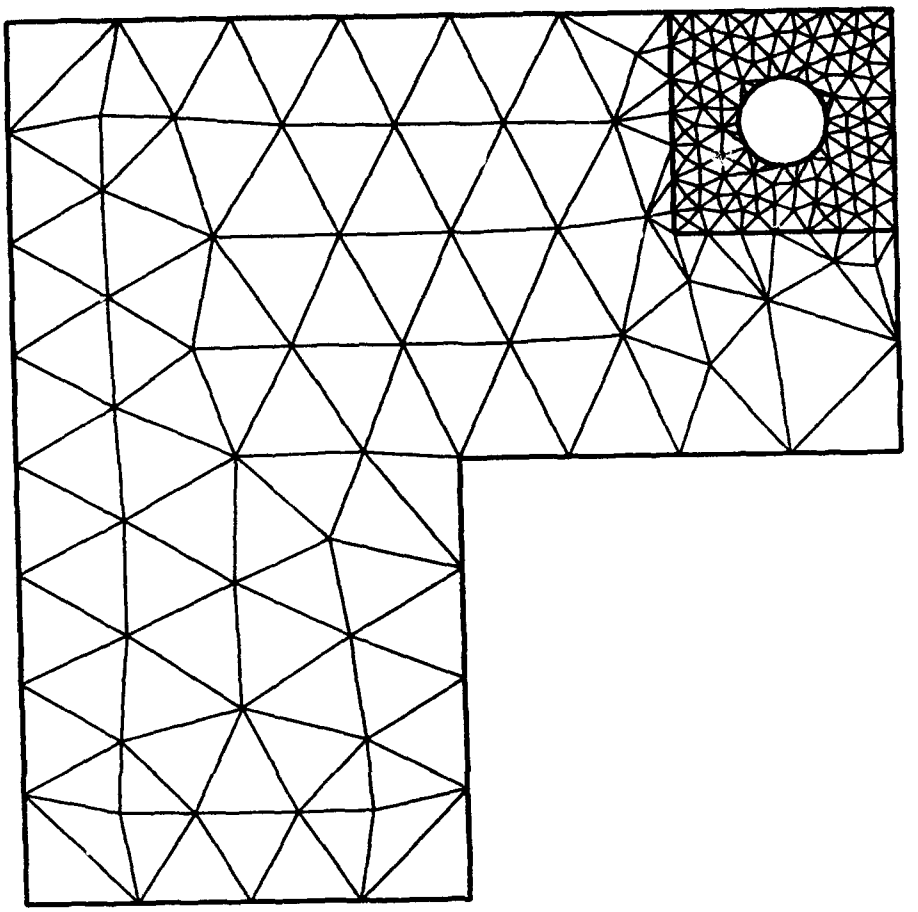

(d)

Figure 1.1 (continued)

and the *distortion* of the elements; the geometry has to be understood in connection with the differential operator (e.g. [41]).

2. *The smoothness of the solution*: The smoothness is characterized by the *regularity* of the solution (see [46]-[56]) which depends on the differential operator, the loads, the geometry of the boundary of the domain and the geometry of the material interfaces. For further details about the smoothness of solutions of linear elliptic boundary-value problems in polygonal domains see [49]-[56].

3. *The pollution error*: By pollution error we characterize the errors in the approximation which emanate from singular points, boundary-conditions, mesh- and material-interfaces and which may affect the order of convergence of the approximation throughout the domain (see [57]-[66]).

In [44] and [45] we presented a theoretical framework and a computer-based approach for checking the local quality of estimators. The methodology in [44], [45] enables one to obtain a quantitative measure of the quality for any error estimator for interior *mesh-cells* ω_0^h in the interior of the grid (an example of an interior mesh-cell is given in Fig. 1.2; the mesh-cells are patches from the mesh which may consist of a few elements, possibly one). In [45] we studied the robustness of several error estimators (which are used in practice) for interior mesh-cells for the complex grids which are employed in practical engineering computations and we identified several robust estimators.

The theoretical framework of the methodology for checking the local quality of estimators (which was employed in the study of estimators in [44] and [45]) assumes that *the pollution-error in the mesh-cell* ω_0^h *is negligible* with respect to the error in the best-approximation defined over a slightly bigger mesh-cell $\tilde{\omega}^h$ which includes ω_0^h and a few mesh-layers around it. This assumption implies a proper relationship (which depends on the exact solution and hence on the data of the problem) between the mesh-size inside and outside the mesh-cell ω_0^h. In this work we show that this assumption is necessary (is not a technicality in the proofs given in [44]) i.e. if the pollution-effect in ω_0^h is large (with respect to the error in the local best-approximation), nothing can be said about the reliability of any error estimator which is based on local computations in ω_0^h. Moreover we demonstrate that *it is possible to control the pollution-error in any interior mesh-cell by proper design of the mesh and hence it is possible to ensure the reliability of the error estimators in any region of interest.*

In this work we will study the effect of the pollution error, due to singularities introduced by rough domains (domains with corner-points) or abrupt changes in the boundary-conditions, on the quality of error estimators for interior mesh-cells. Singularities of this type occur in typical two-dimensional geometrical idealizations of problems in solid mechanics and heat-transfer. Moreover it is well known

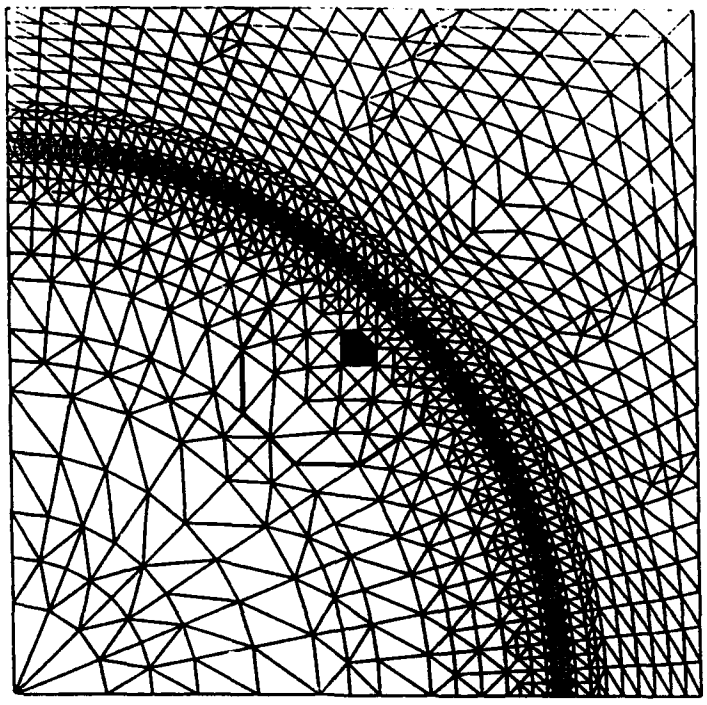

(a)

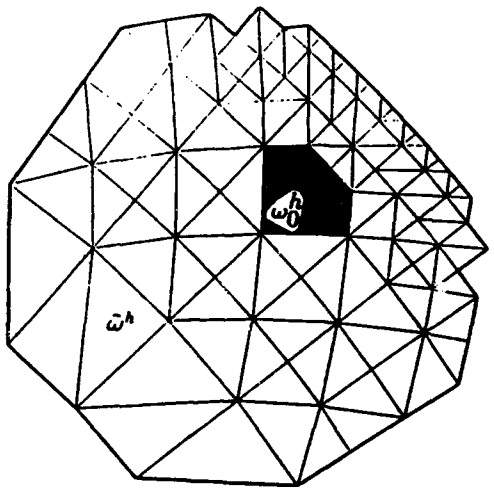

(b)

Figure 1.2. (a) A finite-element grid with an interior mesh-cell ω_0^h (shown shaded gray) surrounded by the mesh-cell $\tilde{\omega}^h$ and three mesh-layers around it; (b) Close-up view of the mesh-cells.

(e.g. [64], [65]) that singularities of this type pollute the approximation throughout the domain while singularities introduced by rough right-hand sides (concentrated loads) affect the approximation only in the neighborhood of the singular points. Therefore the pollution error caused by such singularities (due to rough domains or rough boundary-conditions) is of great importance in practical computations.

In this work we will analyze the pollution error due to rough domains and rough boundary-data in the h-version of the finite element method, its effect on local error-estimation for interior mesh-cells and how the pollution-error can be controlled to guarantee the reliability of local error estimation. We considered only interior mesh-cells for simplicity; the conclusions of this study are also true for mesh-cells which abutt to the boundary of the domain and for mesh-cells near or at singular points.

The main points of the work are:

1. For quasi-uniform meshes (often used in practical computations) the pollution error could be significant throughout the domain depending on the data of the problem and the polynomial degree of the elements employed in the mesh.

2. When the mesh is refined locally (in a region of interest only) the pollution-effect may dominate the computation and there may be no gain in the accuracy in the region of interest.

3. All practical error estimators are based on local computations and therefore cannot detect the pollution error.

4. When the mesh is nearly equilibrated in the energy-norm the pollution-effect in the derivatives is negligible.

5. The pollution-effect in an interior subdomain can be controlled by employing meshes which are coarser (outside the subdomain of interest) than the globally nearly equilibrated grids.

Following this Introduction, in Section 2 we describe the model elliptic problem and two error estimators which were employed in the numerical examples. In Section 3 we give numerical examples and the analysis of the pollution-effect for uniform meshes and introduce the notions of near-field and far-field pollution. In Section 4 we give examples that demonstrate that when the grid is nearly equilibrated in the energy-norm the pollution-effect is negligible. In Section 5 we demonstrate that, when the mesh is refined locally in a subdomain of interest, there may be no gain in the accuracy in the interior of the subdomain and in Section 6 we give numerical examples which indicate that it is possible to control the pollution-error in a subdomain of interest by employing grids which are less refined (outside the subdomain) than the nearly-equilibrated grids (i.e. the globally-adaptive grids).

2 Preliminaries

2.1 The model problem

Let $\Omega \subseteq \mathbf{R}^2$ denote a polygonal domain with boundary $\partial\Omega = \Gamma = \bigcup_{i=1}^{M} \bar{\Gamma}_i$, where Γ_i, $i = 1, \ldots, M$ are the open straight edges connecting the endpoints A_i and A_{i+1} ($A_1 = A_{M+1}$) (see Fig. 2.1). We will denote the internal angles at the vertices by $\varphi_1, \ldots, \varphi_M$ ($0 < \varphi_i \leq 2\pi$; if $\varphi_i = 2\pi$ we have a *slit-domain*). Let further $\Gamma = \bar{\Gamma}_D \cup \bar{\Gamma}_N$, $\Gamma_D \cap \Gamma_N = \emptyset$ where Γ_D is the *Dirichlet*- and Γ_N is the *Neumann*-boundary.

By $H^m(\Omega)$, m is positive integer, we denote the Sobolev space of functions with square integrable derivatives up to order m with the norm, seminorm

$$\|u\|^2_{H^m(\Omega)} := \sum_{0 \leq k \leq m} \|\mathcal{D}^k u\|^2_\Omega , \qquad |u|^2_{H^m(\Omega)} := \|\mathcal{D}^m u\|^2_\Omega$$

$$(\mathcal{D}^m u)(x) := \left[\left(\sum_{|\alpha|=m} |D^\alpha u|^2 \right)(x) \right]^{\frac{1}{2}} , \qquad D^\alpha u := \frac{\partial^{|\alpha|} u}{\partial x_1^{\alpha_1} \partial x_2^{\alpha_2}}$$

where $\alpha := (\alpha_1, \alpha_2)$, $\alpha_i \geq 0$, integers, $i = 1, 2$, $|\alpha| := \alpha_1 + \alpha_2$. Here $\|\cdot\|_\Omega$ denotes the L^2-norm over Ω.

Let $\mathcal{T} := \{T_h\}$ be a *regular* family of triangulations of Ω (the minimal angle of all the triangles is bounded below by a positive constant, the same for all meshes). The meshes are not assumed to be quasi-uniform. We let E (resp. E_{int}) denote the set of edges (resp. interior-edges) in the triangulation. We will consider the mixed boundary-value problem for the Laplacian:

$$L(u) := -\nabla \cdot \nabla u = -\Delta u = 0 \qquad \text{in } \Omega \tag{2.1a}$$

$$u = 0 \qquad \text{on } \Gamma_D \tag{2.1b}$$

$$\frac{\partial u}{\partial n} := \nabla u \cdot n = g \qquad \text{on } \Gamma_N \tag{2.1c}$$

Here u is the solution; n denotes the exterior unit-normal on Γ_N; $g \in L^2(\Gamma_N)$ and is analytic in each Γ_j, $j = 1, \ldots, M$.

In the neighborhood $O(x_\ell; r_0) = \Omega \cap \left\{ x \;\middle|\; |x - x_\ell|_{\mathbf{R}^2} < r_0 \right\}$ of the vertex A_ℓ (x_ℓ is the position-vector of A_ℓ), the exact solution can be written in the form (for *homogeneous* boundary-conditions in the neighborhood of the vertex A_ℓ)

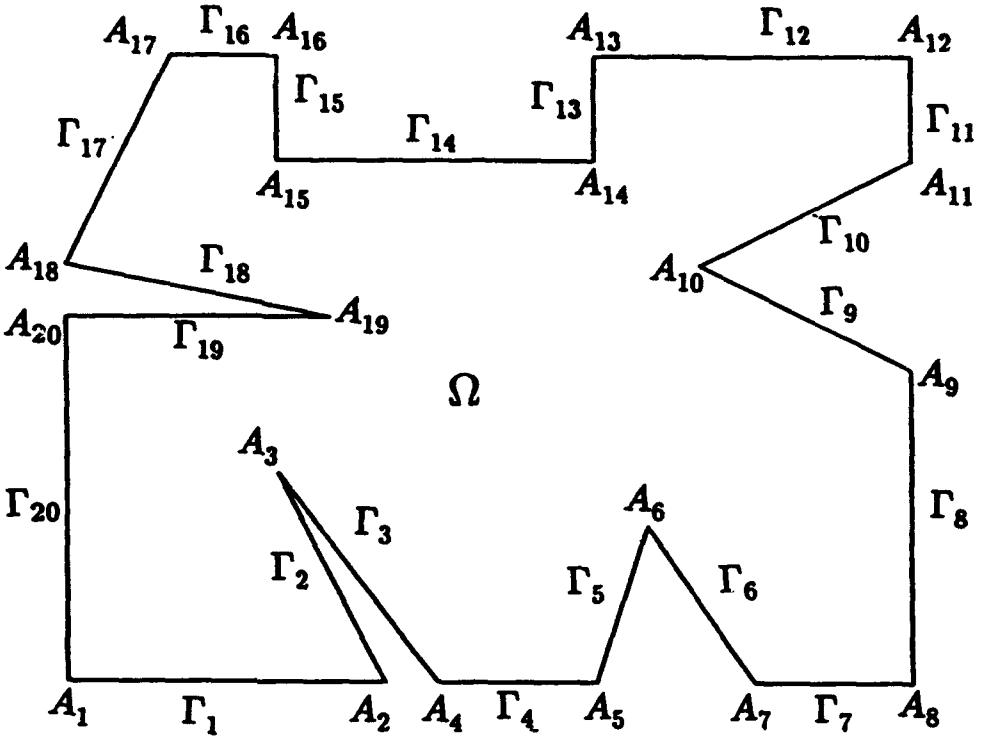

Figure 2.1. An example of a polygonal domain Ω with boundary segments Γ_i and vertices A_i, $i = 1, \ldots, 20$.

$$u(r_\ell, \theta_\ell) = \sum_{j=1}^{Q_\ell} c_j \psi_j(\theta_\ell) r_\ell^{\alpha_j} + u_0(r_\ell, \theta_\ell) \quad , \tag{2.2a}$$

with $u_0(r_\ell, \theta_\ell)$ smoother than the first term, where (r_ℓ, θ_ℓ) are the polar coordinates with respect to the vertex A_ℓ. The functions ψ_j and the exponents α_j are

$$\psi_j(\theta_\ell) = \begin{cases} \sin(\alpha_j \theta_\ell) \, , & \text{for the Dirichlet or mixed problem} \, , \\ \cos(\alpha_j \theta_\ell) \, , & \text{for the Neumann problem} \, , \end{cases} \tag{2.2b}$$

$$\alpha_j = \begin{cases} \dfrac{j\pi}{\varphi_\ell} \, , & \text{for the Dirichlet or Neumann boundary conditions} \, , \\ \dfrac{(2j-1)\pi}{2\varphi_\ell} \, , & \text{for mixed boundary-conditions} \, , \end{cases} \tag{2.2c}$$

(The mixed problem here means homogeneous Dirichlet conditions for $\theta_\ell = 0$ and homogeneous Neumann conditions for $\theta_\ell = \varphi_\ell$).

Remark 2.1. In the numerical examples we considered specially unsmooth solutions of the type given by (2.2a)-(2.2c) because such solutions occur typically as solutions of practical boundary-value problems.

We let $H^1_{\Gamma_D} := \left\{ u \in H^1(\Omega) \;\middle|\; u = 0 \text{ on } \Gamma_D \right\}$. The variational formulation of the model problem (2.1) is: Find $u \in H^1_{\Gamma_D}$ such that

$$B(u, v) = \int_{\Gamma_N} gv \qquad \forall \; v \in H^1_{\Gamma_D} \tag{2.3a}$$

where

$$B_\Omega(u, v) := \int_\Omega \nabla u \cdot \nabla v \, , \qquad u \, , \; v \in H^1_{\Gamma_D} \tag{2.3b}$$

If $\Gamma_D = \emptyset$ then the usual restrictions on the data are imposed and the solution u is determined up to an arbitrary constant. We let

$$|||v|||_S := (B_S(v, v))^{\frac{1}{2}} = \left(\int_S |\nabla v|^2 \right)^{\frac{1}{2}} \tag{2.4}$$

denote the energy-norm over S.

Let $u_h \in S^p_{h,\Gamma_D} := \left\{ v \in H^1_{\Gamma_D} \;\middle|\; v\,|_\tau \in \mathcal{P}_p(\tau) \;\; \forall\, \tau \in T_h,\; v = 0 \;\text{ on }\; \Gamma_D \right\}$ be the piecewise p-degree finite element approximation of the solution of (2.1) and (2.2) which satisfies:

Find $u_h \in S^p_{h,\Gamma_D}$ such that

$$B_\Omega(u_h, v_h) = \int_{\Gamma_N} g\, v_h \qquad \forall\; v^h \in S^p_{h,\Gamma_D} \tag{2.5}$$

The error is $e_h := u - u_h$ and satisfies the *residual-equation*:

Find $e_h \in H^1_{\Gamma_D}$ such that

$$B_\Omega(e_h, v) = \sum_{\tau \in T_h} F_\tau(v) \qquad \forall\; v \in H^1_{\Gamma_D} \tag{2.6}$$

where $F_\tau :\; H^1_{\Gamma_D} \to \mathbf{R}$ is the *residual functional* given by

$$F_\tau(v) := \int_\tau v r_\tau + \frac{1}{2} \sum_{\epsilon \subseteq \partial\tau} \int_\epsilon v J_\epsilon \,, \qquad v \in H^1_{\Gamma_D} \tag{2.7}$$

Here $r_\tau := \Delta u_h$ denotes the *interior-residual* in element τ and J_ϵ is the *inter-element-jump in the normal derivative*

$$J_\epsilon := \begin{cases} [\nabla(u_h\,|_{\tau_{\text{in}}}) - \nabla(u_h\,|_{\tau_{\text{out}}})] \cdot n \,, & \epsilon \in E_{\text{int}} \\ 2\Big(g - \dfrac{\partial u_h}{\partial n}\Big) \,, & \epsilon \subseteq \Gamma_N \\ 0 \,, & \epsilon \subseteq \Gamma_D \end{cases} \tag{2.8}$$

where n is the unit-normal assigned to the edge ϵ (in an arbitrary but unique way) and τ_{out}, τ_{in} are defined as in Fig. 2.2.

2.2 The error estimators

We summarize the definitions of the error estimators employed in the numerical examples below (see also [44] and [45]).

2.2.1 Implicit element-residual estimator

Let us define the *equilibrated* residual functional

$$F^{\text{EQ}}_\tau(v) := F_\tau(v) + \int_{\partial\tau} v\, \theta_\tau \,, \qquad v \in H^1(\tau) \tag{2.9}$$

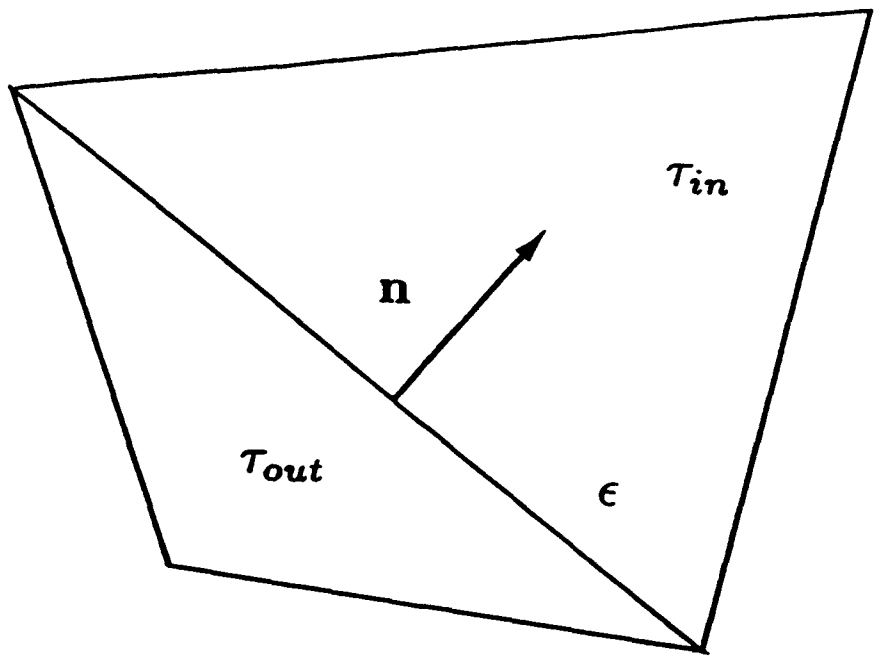

Figure 2.2. An edge ϵ with its normal n and the elements τ_{out}, τ_{in} connected to it.

Here $\theta_\tau \in (L^2(\partial\tau))^2$ is the *correction* of the edge-residuals which is determined such that

$$F_\tau^{RQ}(v) = 0 \qquad \forall\ v \in \mathcal{P}_p(\tau) \tag{2.10}$$

Definitions of θ_τ which satisfy (2.10) for linear elements are given in [14], [15], [24], [25], [28]; in the numerical implementations for linear elements we employ the definition given in [14]. We define the *element error-indicator function* e_τ as the solution (which is unique up to a constant) of the *local problem*:

Find $\tilde{e}_\tau \in H_\tau$ such that

$$B_\tau(\tilde{e}_\tau, v_\tau) = F_\tau^{RQ}(v_\tau) \qquad \forall\ v_\tau \in H_\tau \tag{2.11}$$

Here $H_\tau = H^1(\tau)$. We then define the *element error-indicators* η_τ for the energy-norm of the error by

$$\eta_\tau := \sqrt{B_\tau(e_\tau, e_\tau)} \tag{2.12}$$

In the computations below we approximated the solutions of the local problems by using a finite dimensional space of polynomials of degree $(p+1)$ in the element, namely

$$B_\tau^{p+1} := \left\{ w \in \mathcal{P}_{p+1}(\tau) \,\middle|\, \Pi_\tau^p w = 0 \right\} \tag{2.13}$$

where $\Pi_\tau^p : \mathcal{P}_{p+1}(\tau) \longrightarrow \mathcal{P}_p(\tau)$ is an interpolation-operator defined (see [19], [20]) over the element τ. The space B_τ^{p+1} is often referred to as the *bubble-space* (see [19]). In the sequel, we will call *ER*-estimators (element-residual-estimators) the estimators determined from (2.12) by computing approximate solutions of (2.11) from the bubble-space.

We now describe how the corrections for the edge-residuals θ_τ are constructed. We let

$$\theta_\tau|_\epsilon = \zeta_\tau^\epsilon \left(\theta_\epsilon^1 \psi_1^\epsilon + \theta_\epsilon^2 \psi_2^\epsilon \right), \qquad \epsilon \subseteq \partial\tau \tag{2.14}$$

where

$$\zeta_\tau^\epsilon = \begin{cases} +1, & \text{if } \tau = \tau_{in}, \\ -1, & \text{if } \tau = \tau_{out}, \end{cases} \tag{2.15}$$

Here it is assumed that an edge-normal n has been assigned to the edge ϵ in an arbitrary but unique way and τ_{in} and τ_{out} are defined as shown in Fig. 2.2. Here

$$\psi_1^\epsilon := \frac{2}{|\epsilon|}(2\lambda_1^\epsilon - \lambda_2^\epsilon) \ , \qquad \psi_2^\epsilon := \frac{2}{|\epsilon|}(2\lambda_2^\epsilon - \lambda_1^\epsilon) \tag{2.16}$$

where λ_k^ϵ, $k = 1, 2$ are the linear shape-functions defined over the edge ϵ, and

$$\theta_\epsilon^k := \int_\epsilon \theta_\tau|_\epsilon \ \lambda_k^\epsilon \quad , \qquad k = 1, 2 \quad , \qquad \epsilon \subseteq \partial\tau \tag{2.17}$$

The integrals θ_ϵ^k in (2.17) are obtained from the linear system (see Ladeveze and Leguillon [14] and Bank and Weiser [15] for the details)

$$\int_{\partial\tau_k^X} \theta_{\tau_k^X} \Phi_X = -F_\tau(\Phi_X) \quad , \quad k = 1, \ldots, (ne)_X \tag{2.18}$$

where Φ_X denotes the elementwise affine basis function, which corresponds to the vertex X, shown in Fig. 2.3b; τ_k^X denotes the k-th element connected to the vertex X; $(ne)_X$ is the total number of elements connected to the vertex X.

The procedure outlined above has been developed by Ladeveze [14]. The linear system (2.18) has a one parameter family of solutions. Specific choices of solutions are suggested in [14] and [15]. In the numerical implementations we employed the choice given in [14]. Below we give the definition of the edgewise-linear corrections θ_τ which result by using the equilibration procedures of [14].

Let us consider the vertex X and let N_X denote the total number of the edges (or the elements) connected to the vertex as shown in Fig. 2.3a. Let us also denote by τ_i and ϵ_i, $i = 1, \ldots, N_X$ the elements and the edges connected to X. We determined the coefficients $\theta_\epsilon^{\nu(\epsilon,X)}$ which are associated with the edge ϵ and the vertex X and are employed in (2.14); here the index-function $\nu(\epsilon, X)$ identifies the node X in the local enumeration used in (2.14) for the unknowns associated with the edge. The values of the coefficients are (see also [14]):

$$\theta_{\epsilon_1}^{\nu(\epsilon_1,X)} = \theta_{\epsilon_N}^{\nu(\epsilon_N,X)} - F_{\tau_1}(\Phi_X) \ , \quad \theta_{\epsilon_N}^{\nu(\epsilon_N,X)} = \frac{1}{N}\sum_{i=1}^{N}(N - i + 1)\, F_{\tau_i}(\Phi_X) \tag{2.20a}$$

$$\theta_{\epsilon_i}^{\nu(\epsilon_i,X)} = \theta_{\epsilon_{i-1}}^{\nu(\epsilon_{i-1},X)} - F_{\tau_i}(\Phi_X) \ , \qquad i = 2, 3, \ldots, (N-1) \tag{2.20b}$$

The edge-coefficients $\theta_{\epsilon_i}^{\nu(\epsilon_i,X)}$ are computed based on the edge-normals which rotate counterclockwise around the vertex X as shown in Fig. 2.3a.

Remark 2.2. It is also possible to define the equilibration for polynomial spaces up to degree p (where p denotes the polynomial degree of the elements).

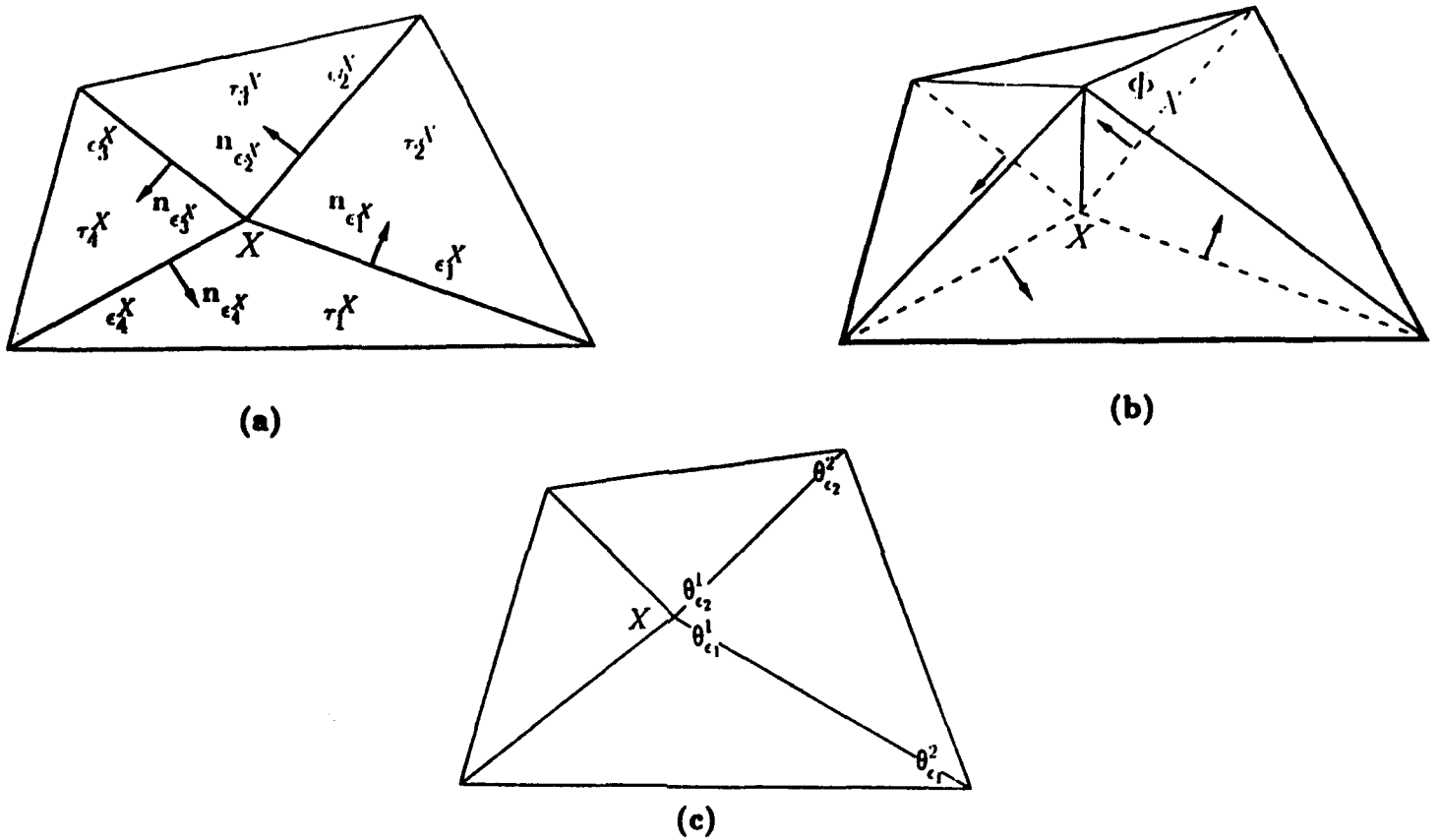

Figure 2.3. (a) The vertex X with the element τ_k^X and the edges ϵ_k^X attached to it; (b) The graph of the elementwise linear global basis functions Φ_X corresponding to the node X; (c) The local enumeration for the degrees of freedom of the correction θ for the edges connected to node X.

2.2.2 Error estimator based on patch-averaging

Here we outline an error-estimator based on local averaging which was introduced by Zienkiewicz and Zhu [36, 37]. This estimator will be called the *ZZ*-estimator in the examples below.

Let $\omega_X := \bigcup_{X \in N(\tau')} \tau'$ denote the *patch* of elements connected to vertex X. For each patch ω_X we recover the *patch-projections* σ^*_X, by solving the following least-squares problem:

$$J(\sigma^*_X - \nabla u_h) = \inf_{\sigma \in (\mathcal{P}_p)^2} J_\sigma(\sigma - \nabla u_h), \qquad J(\sigma) := \sum_{m=1}^{nsp} \left[\sum_{i=1}^{2} (\sigma_i(y_m))^2 \right] \tag{2.21}$$

Here y_m, $m = 1, \ldots, nsp$ denotes a set of *sampling-points* in the patch ω_X.

The element error indicators for the *ZZ*-estimator are given by

$$\eta_\tau := \|\sigma^{ZZ} - \nabla u_h\|_\tau \tag{2.22}$$

Here σ^{ZZ} denotes the *recovered gradient* which is obtained by averaging the patch-projections σ^*_X. For the grids of triangular elements employed in this study a continuous recovered flux σ^{ZZ} is obtained by taking appropriate averages of the flux recovered from the three patches associated with the element. In this work we implemented the *ZZ*-estimator for elements of degree $p = 1$, 2, and 3 as follows:

a. Linear elements ($p = 1$).

The nodal values of σ^{ZZ} are recovered from the patches corresponding to each node. The recovered C^0-continuous piecewise-linear flux-field σ^{ZZ} over the domain is constructed as

$$\sigma^{ZZ}(x) = \sum_X \sigma^*_X\big|_X \, \Phi_X(x) \tag{2.23}$$

Here σ^*_X is the recovered flux field over the patch ω_X and $\sigma^*_X\big|_X$ is the value of the recovered flux-field at the vertex X and Φ_X is the piecewise-linear basis function associated with the vertex X.

b. Quadratic elements ($p = 2$).

A piecewise quadratic Langrangian representation of σ^{ZZ} is constructed from

$$\sigma^{ZZ}(x) = \sum_X \sigma^*_X\big|_X \, \Phi_X(x) + \sum_Y \frac{1}{2}\left(\sigma^*_{X_1}\big|_Y + \sigma^*_{X_2}\big|_Y\right) \Phi_Y(x) \tag{2.24}$$

where Y is used to denote the midside nodes for the edges; Φ_X, Φ_Y are the Langrangian quadratic basis functions associated with the nodes X, Y respectively;

X_1, X_2 are the vertices at the endpoints of the side which includes the midside node Y.

c. Cubic elements ($p = 3$).

A piecewise cubic Langrangian representation of σ^{ZZ} is constructed from

$$\sigma^{ZZ}(x) = \sum_X \sigma^*_X\big|_X \, \Phi_X(x) + \frac{1}{2} \sum_{Y \in \{Y_1 \ldots Y_6\}} \left(\sigma^*_{X_1}\big|_Y + \sigma^*_{X_2}\big|_Y\right) \Phi_Y(x)$$

$$+ \frac{1}{3}\left(\sigma^*_{X_1}\big|_{Y_7} + \sigma^*_{X_2}\big|_{Y_7} + \sigma^*_{X_3}\big|_{Y_7}\right) \Phi_{Y_7}(x) \tag{2.25}$$

where $Y_1, \ldots, Y_6$ are used to denote the nodes for the Lagrangian cubic element on the edges and Y_7 denotes the interior node at the centroid of the element; Φ_X and Φ_Y are the cubic Langrangian basis functions associated with the nodes X and Y respectively; X_1, X_2, X_3 are the vertices of the triangular element.

Zienkiewicz and Zhu [36, 37] proposed two types of least-square problems for the recovery of σ^*_X namely a *discrete* and a *continuous* least-squares patch-projection. Here we used the discrete least-squares patch projection and we employed the sampling points shown in Fig. 2.4a, Fig. 2.4b and Fig. 2.4c for linear, quadratic and cubic triangles, respectively.

2.3 Definition of the effectivity index

The quality of an error estimator in a mesh-cell ω_0^h is measured by the *effectivity index*

$$\kappa_{\omega_0^h} := \frac{\mathcal{E}_{\omega_0^h}}{\|e_h\|_{\omega_0^h}} \quad , \qquad \mathcal{E}_{\omega_0^h} := \left\{ \sum_{\substack{\tau \in T_h \\ \tau \subseteq \omega_0^h}} \eta_\tau^2 \right\}^{\frac{1}{2}} \tag{2.26}$$

Here T_h denotes the finite-element mesh which includes the mesh-cell ω_0^h in its interior, as shown in Fig. 1.2, $\|e_h\|_{\omega_0^h}$ is the norm (of interest) of the error e_h over ω_0^h, $\mathcal{E}_{\omega_0^h}$ is an error estimator for this norm which is computed in terms of *element error-indicators* η_τ associated to every element τ of the mesh T_h.

In [44], [45] it was demonstrated that, when the pollution error is negligible, the value of the effectivity index $\kappa_{\omega_0^h}$ in the mesh-cell ω_0^h is influenced (for all practical purposes) by the geometry of the mesh in a *mesh-patch* $\tilde{\omega}^h$ which includes ω_0^h and a few mesh-layers around it. The *asymptotic range* of the effectivity index in the cell

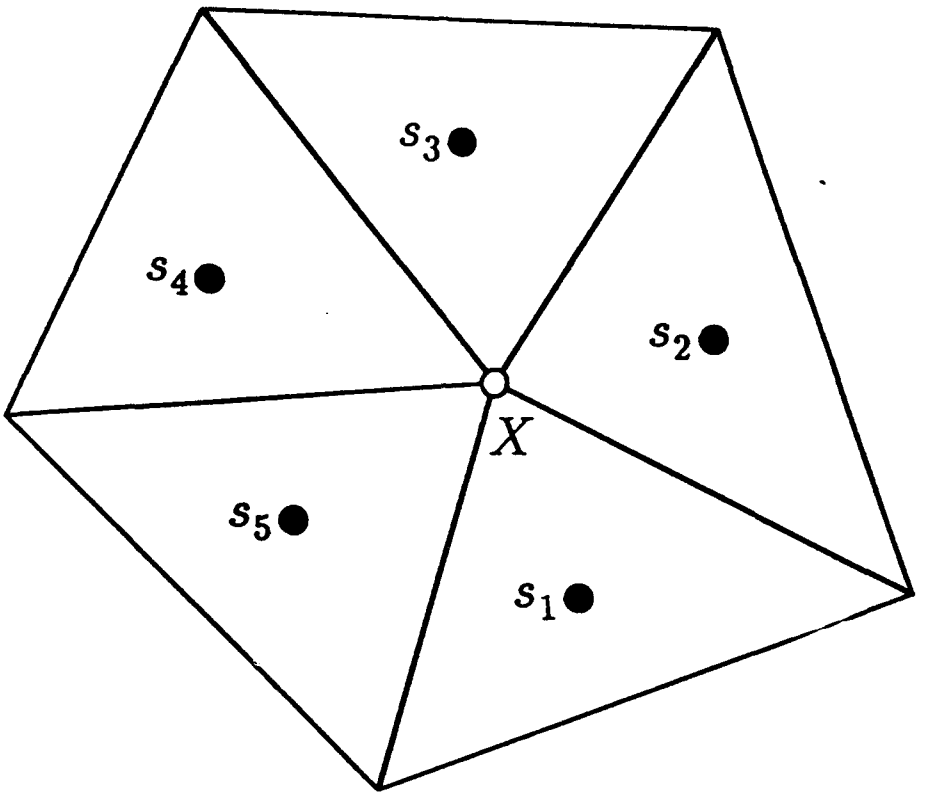

(a)

Figure 2.4. Location of the sampling points employed by the discrete ZZ-estimator in the interior mesh-patches. (a) Sampling points for linear elements; these points are located at the centroids of the elements; (b) Sampling points for quadratic elements; the points are ocated at the midpoints of the sides of the elements; (c) Sampling points for cubic elements; the points are located at the vertices, at the midpoints of the sides and at the centroid of the elements.

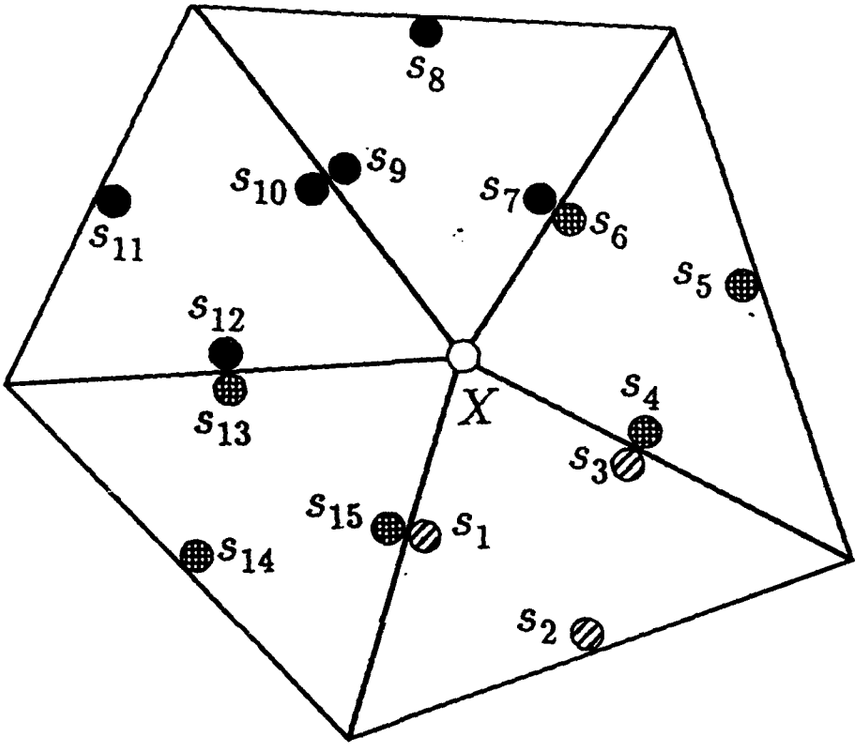

(b)

Figure 2.4. (continued)

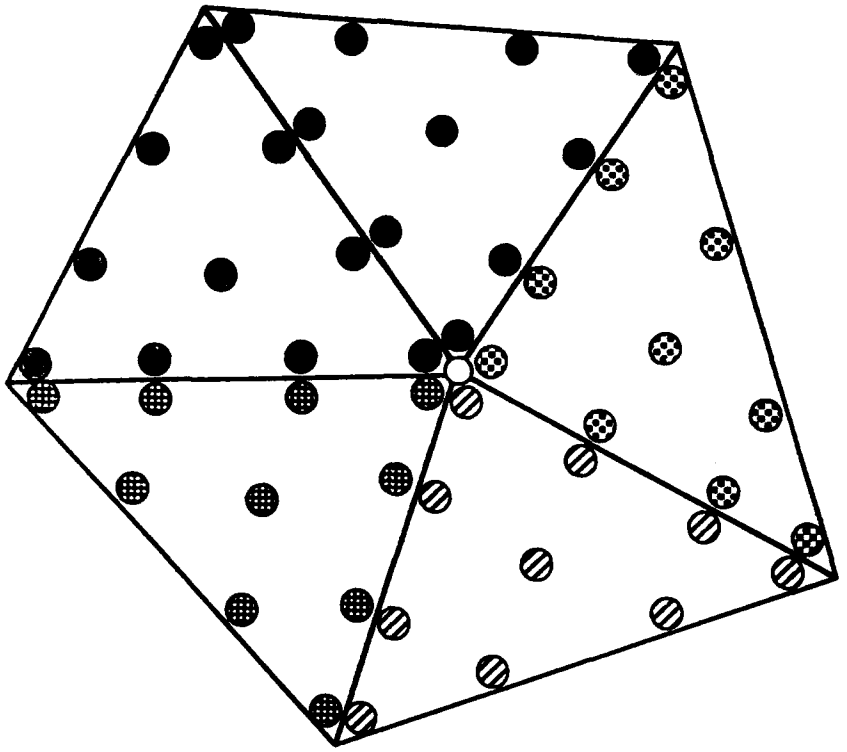

(c)

Figure 2.4. (continued)

$$0 \leq C_L^{\omega_0^h} \leq \kappa_{\omega_0^h} \leq C_U^{\omega_0^h} \tag{2.27}$$

is defined in terms of the constant $C_L^{\omega_0^h}$, $C_U^{\omega_0^h}$, which can be determined by a *computer-based approach* (see [44], [45]). Inequality (2.27) can also be written in the form

$$\frac{1}{C_U^{\omega_0^h}} \mathcal{E}_{\omega_0^h} \leq \|e_h\|_{\omega_0^h} \leq \frac{1}{C_L^{\omega_0^h}} \mathcal{E}_{\omega_0^h} \tag{2.28}$$

which expresses the *equivalence* between the norm of the error and the estimator in the mesh-cell ω_0^h.

For example, for linear elements ($p = 1$) and for the Regular mesh-pattern shown in Fig. 2.5a, the values of the constants are (see [44]) $C_L^{\omega_0^h} = C_U^{\omega_0^h} = 1.00$ for both the *ER* and the *ZZ* estimator while for the Criss-Cross mesh-pattern shown in Fig. 2.5b, the values are, $C_L^{\omega_0^h} = 1.00$, $C_U^{\omega_0^h} = 1.414$ for the *ER* estimator without equilibration, $C_L^{\omega_0^h} = C_U^{\omega_0^h} = 1.00$ for the *ZZ* estimator and the *ER* estimator with equilibration. Further results about the above and other estimators for various mesh-patterns are given in [44, 45]. From these results it is clear that the *ER* estimator with equilibrated data and the *ZZ* estimator are *robust* estimators ($C_L^{\omega_0^h} \approx C_U^{\omega_0^h} \approx 1$) for typical meshes used in engineering computations. As it was pointed out earlier the constants $C_L^{\omega_0^h}$, $C_U^{\omega_0^h}$ can be determined under the assumption that the pollution error is negligible in a neighborhood of the mesh-cell of interest (see [44] for the mathematical analysis). In this work we demonstrate that:

1. The assumption on the pollution error is necessary (i.e. when the pollution error is significant in the mesh-cell ω_0^h (with respect to the error in the best-approximation in $\tilde{\omega}^h$), (2.28) does not hold).

2. Robust a-posteriori error estimation in a mesh-cell ω_0^h (and hence the validity of (2.28)) is possible by controlling the pollution error in ω_0^h through proper design of the mesh outside ω_0^h.

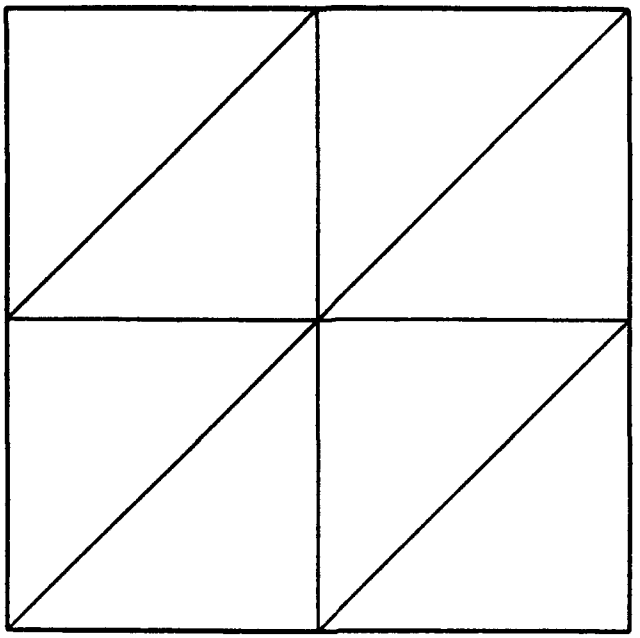

(a)

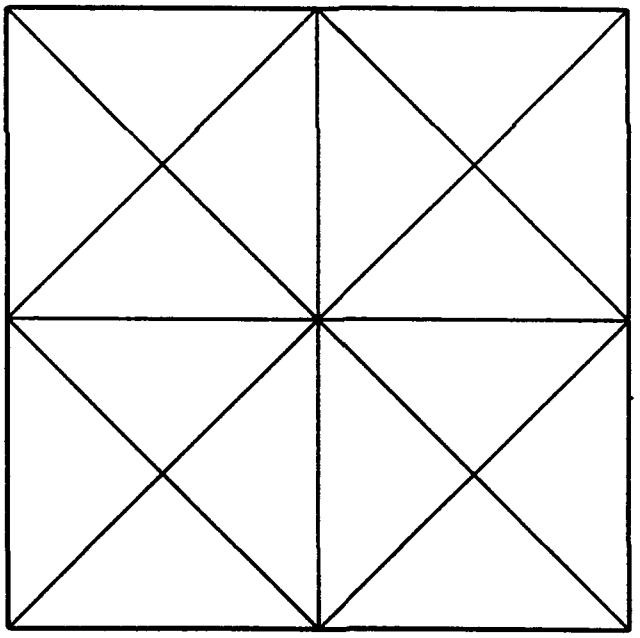

(b)

Figure 2.5. (a) Basic mesh-cell of the Regular mesh-pattern (b) Basic mesh-cell from the Criss-Cross mesh-pattern.

3 The pollution-effect for uniform meshes

Practical computations in elasticity and heat-transfer are often performed using meshes which are nearly uniform (quasi-uniform). It is therefore important to understand the pollution-effect for such meshes. Below we give numerical examples which demonstrate the pollution-effect for uniform-meshes of linear, quadratic and cubic triangles.

3.1 Numerical examples of the pollution-effect for uniform meshes

Here we present numerical examples which demonstrate that for the class of uniform meshes and the class of specially unsmooth solutions (with algebraic singularities of the type given in (2.2a)-(2.2c)) the pollution-effect depends on the relationship between the values of the exponents of the algebraic singularities and the polynomial degree of the elements.

3.1.1 Uniform meshes of linear elements

We considered the mixed boundary-value problems for the Laplace equation in the L-shaped domain $\left(\varphi_1 = \frac{3\pi}{2}\right)$ shown in Fig. 3.1a. We applied boundary-conditions consistent with the exact solution $u(r,\theta) = r^\alpha \sin(\alpha\theta)$, for $\alpha = \frac{\pi}{2\varphi_1} = \frac{1}{3}$ and $\alpha = \frac{\pi}{\varphi_1} = \frac{2}{3}$ $\Big($for $\alpha = \frac{1}{3}$ homogeneous mixed boundary-conditions (resp. for $\alpha = \frac{2}{3}$ homogeneous Dirichlet boundary-conditions) were applied on the edges A_1A_2, A_1A_6 which emanate from the singular-point while Neumann boundary-conditions were applied on the rest of the boundary; see also Section 2$\Big)$, and we computed finite element solutions using uniform meshes of linear triangles. In Table 3.1 (resp. Table 3.2) we give the effectivity indices for the mesh layers ω_n, $n = 1, \ldots, \frac{1}{h}$ (a typical mesh-layer is shown in Fig. 3.1a) for $\alpha = \frac{2}{3}$ $\left(\text{resp. } \alpha = \frac{1}{3}\right)$. We note that the effectivity indices $\kappa_{\omega_n}^{ER}$ for the ER-estimator and $\kappa_{\omega_n}^{ZZ}$ for the ZZ-estimator are practically the same in the interior-layers. We also note that for $\alpha = \frac{2}{3}$ $\left(\text{resp. } \alpha = \frac{1}{3}\right)$ the effectivity indices in the layers *at a fixed distance from the singularity* converge to one (resp. zero) as the mesh-size h tends to zero.

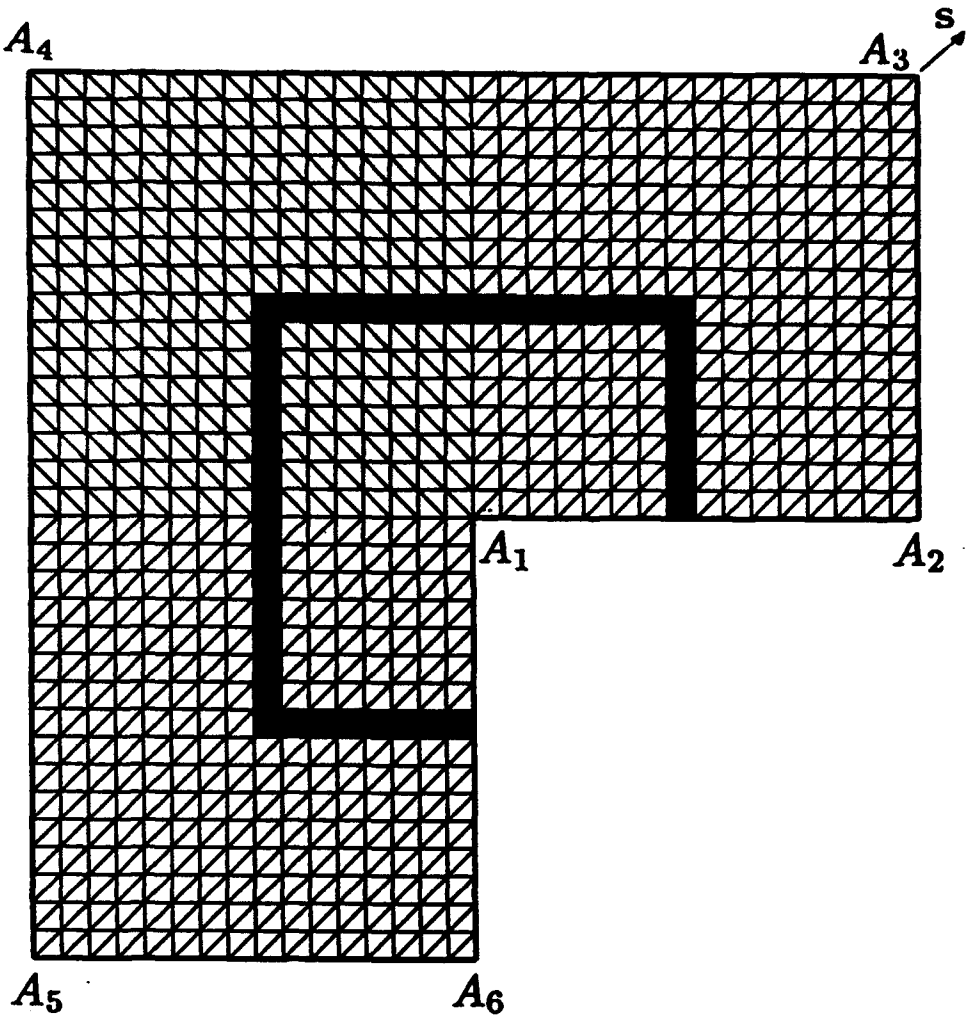

(a)

Figure 3.1. (a) The L-shaped domain with boundary $A_1A_2 \ldots A_6A_1$, meshed with a uniform grid of triangular elements in which the eighth mesh-layer is shaded gray; (b) The convex domain with boundary $A_1A_2 \ldots A_4A_1$, meshed with a uniform grid of triangular elements in which the eighth mesh-layer is shaded gray; (c) The triangular domain with boundary $A_1A_2 \ldots A_3A_1$ meshed with a a uniform grid of triangular elements in which the sixth mesh-layer is shaded gray.

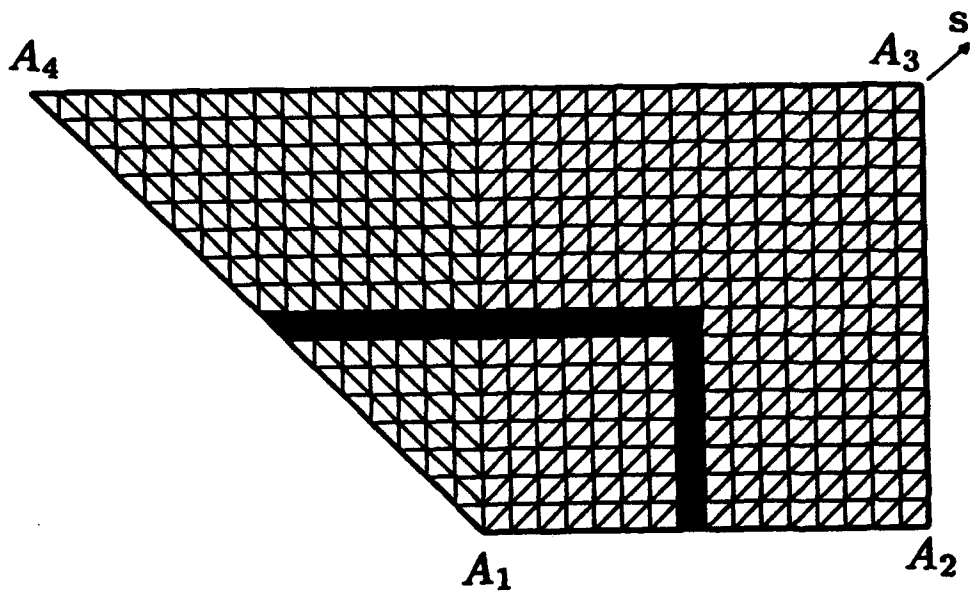

(b)

Figure 3.1. (continued)

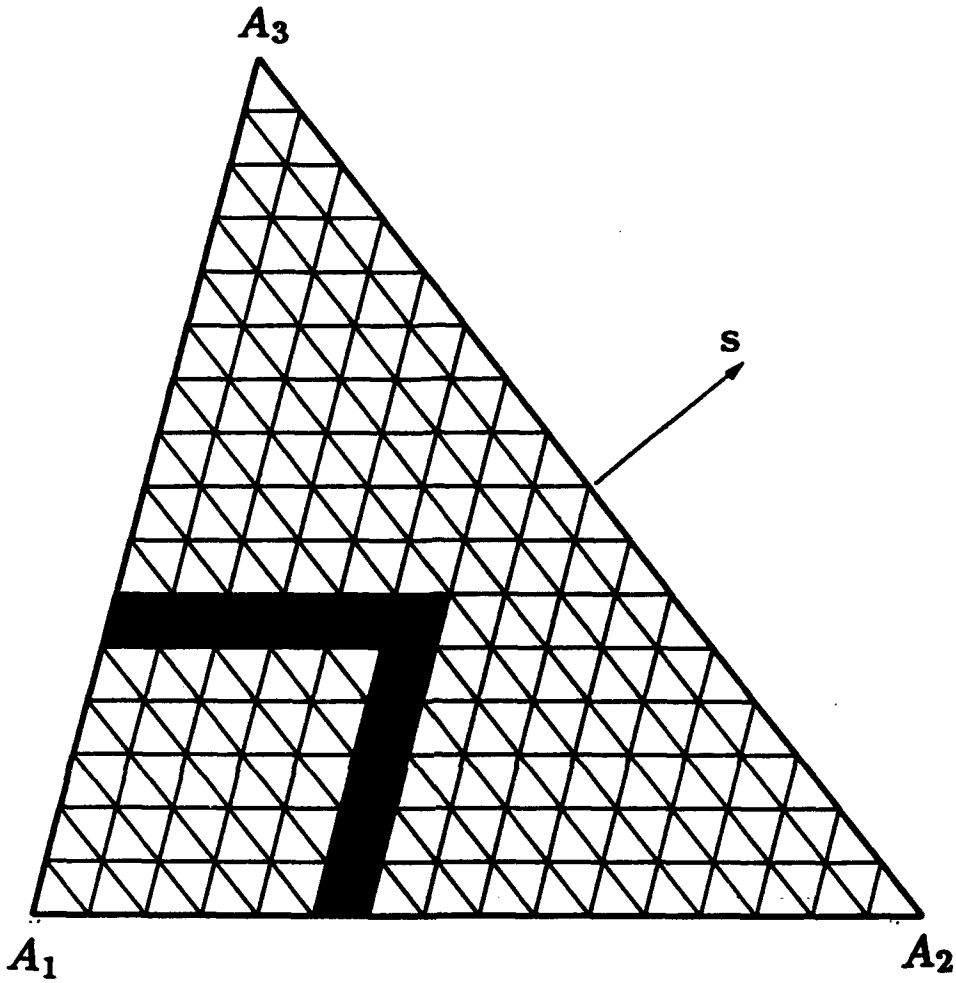

(c)

Figure 3.1. (continued)

Table 3.1. Pollution error for uniform grids. L-shaped domain shown in Fig. 3.1a, $\alpha = \frac{2}{3}$, $p = 1$ $(2\alpha > p)$. Effectivity index for the element-residual and ZZ error estimators for each mesh-layer ω_n. Note that the effectivity indices in the interior mesh-layers are close to one.

Effectivity index for each mesh-layer									
Exact solution $u(r,\theta) = r^{\frac{1}{3}}\sin(\frac{2\theta}{3})$; linear elements									
Layer number n	$h = \frac{1}{4}$			$h = \frac{1}{8}$			$h = \frac{1}{16}$		
	$\kappa^{ZZ}_{\omega_n}$	$\kappa^{ER}_{\omega_n}$	$\frac{\|\|e_h\|\|_{\omega_n}}{\|\|e_h\|\|_\Omega}\cdot 100$	$\kappa^{ZZ}_{\omega_n}$	$\kappa^{ER}_{\omega_n}$	$\frac{\|\|e_h\|\|_{\omega_n}}{\|\|e_h\|\|_\Omega}\cdot 100$	$\kappa^{ZZ}_{\omega_n}$	$\kappa^{ER}_{\omega_n}$	$\frac{\|\|e_h\|\|_{\omega_n}}{\|\|e_h\|\|_\Omega}\cdot 100$
1	0.663	0.684	86.23	0.666	0.686	83.88	0.667	0.687	82.50
2	1.176	1.056	40.11	1.183	1.062	39.01	1.185	1.063	38.38
3	0.989	0.981	24.74	1.004	0.995	23.98	1.006	0.997	23.56
4	0.970	0.991	18.49	0.971	0.972	17.77	0.976	0.977	17.43
5				0.959	0.962	14.33	0.966	0.969	14.03
6				0.951	0.955	12.10	0.962	0.965	11.83
7				0.945	0.949	10.53	0.959	0.963	10.27
8				0.948	0.984	9.39	0.956	0.960	9.12
9							0.954	0.958	8.22
10							0.952	0.956	7.50
11							0.950	0.953	6.91
12							0.948	0.951	6.42
13							0.945	0.948	6.00
14							0.943	0.945	5.64
15							0.939	0.941	5.33
16							0.939	0.978	5.06

Table 3.1. (continued)

Effectivity index for each mesh-layer			
Exact solution $u(r,\theta) = r^{\frac{2}{3}}\sin(\frac{2\theta}{3})$; linear elements			
Layer number n	$h = \frac{1}{32}$		
	$\kappa_{\omega_n}^{ZZ}$	$\kappa_{\omega_n}^{ER}$	$\frac{\|\|e_h\|\|_{\omega_n}}{\|\|e_h\|\|_{\Omega}} \cdot 100$
1	0.667	0.688	81.64
2	1.185	1.064	37.99
3	1.007	0.998	23.32
4	0.976	0.977	17.25
5	0.967	0.971	13.87
6	0.964	0.967	11.69
7	0.962	0.965	10.15
8	0.960	0.964	9.00
9	0.959	0.962	8.11
10	0.957	0.960	7.40
11	0.956	0.959	6.81
12	0.954	0.957	6.32
13	0.953	0.955	5.90
14	0.951	0.954	5.54
15	0.950	0.952	5.23
16	0.948	0.950	4.95
17	0.946	0.948	4.71
18	0.945	0.947	4.49
19	0.943	0.944	4.29
20	0.941	0.943	4.12
21	0.939	0.941	3.96
22	0.937	0.939	3.81
23	0.935	0.937	3.68
24	0.933	0.935	3.55
25	0.932	0.933	3.44
26	0.930	0.931	3.33
27	0.927	0.929	3.23
28	0.926	0.927	3.14
29	0.923	0.925	3.06
30	0.921	0.922	2.97
31	0.918	0.919	2.90
32	0.917	0.956	2.83

Table 3.2. Pollution error for uniform grids. L-shaped domain shown in Fig. 3.1a, $\alpha = \frac{1}{3}$, $p = 1$ $(2\alpha < p)$. Effectivity index for the element-residual and ZZ error estimators for each mesh-layer ω_n. Note that the effectivity indices in the interior mesh-layers are significantly smaller than one.

Effectivity index for each mesh-layer									
Exact solution $u(r,\theta) = r^{\frac{1}{3}}\sin(\frac{\theta}{3})$; linear elements									
Layer number n	$h = \frac{1}{4}$			$h = \frac{1}{8}$			$h = \frac{1}{16}$		
	$\kappa^{ZZ}_{\omega_n}$	$\kappa^{ER}_{\omega_n}$	$\frac{\|\|e_h\|\|_{\omega_n}}{\|\|e_h\|\|_\Omega} \cdot 100$	$\kappa^{ZZ}_{\omega_n}$	$\kappa^{ER}_{\omega_n}$	$\frac{\|\|e_h\|\|_{\omega_n}}{\|\|e_h\|\|_\Omega} \cdot 100$	$\kappa^{ZZ}_{\omega_n}$	$\kappa^{ER}_{\omega_n}$	$\frac{\|\|e_h\|\|_{\omega_n}}{\|\|e_h\|\|_\Omega} \cdot 100$
1	0.748	0.637	89.20	0.772	0.659	87.64	0.787	0.671	86.89
2	0.774	0.796	35.59	0.807	0.830	34.63	0.823	0.846	34.32
3	0.575	0.581	22.06	0.624	0.629	20.73	0.649	0.654	20.13
4	0.483	0.507	16.98	0.519	0.523	15.44	0.552	0.557	14.68
5				0.457	0.461	12.64	0.495	0.499	11.80
6				0.414	0.418	10.86	0.454	0.458	10.00
7				0.382	0.385	9.65	0.423	0.426	8.77
8				0.357	0.377	8.91	0.397	0.399	7.86
9							0.375	0.377	7.16
10							0.357	0.359	6.61
11							0.340	0.342	6.15
12							0.326	0.328	5.77
13							0.312	0.314	5.45
14							0.300	0.302	5.20
15							0.287	0.289	5.00
16							0.274	0.291	4.89

Table 3.2. (continued)

Effectivity index for each mesh-layer			
Exact solution $u(r,\theta) = r^{\frac{1}{3}}\sin(\frac{\theta}{3})$; linear elements			
Layer number n	$h = \frac{1}{32}$		
	$\kappa_{\omega_n}^{ZZ}$	$\kappa_{\omega_n}^{ER}$	$\frac{\|\|\|e_h\|\|\|_{\omega_n}}{\|\|\|e_h\|\|\|_\Omega} \cdot 100$
1	0.796	0.678	86.52
2	0.830	0.853	34.26
3	0.661	0.666	19.92
4	0.567	0.572	14.37
5	0.515	0.519	11.42
6	0.478	0.482	9.57
7	0.450	0.453	8.30
8	0.427	0.429	7.37
9	0.407	0.409	6.65
10	0.390	0.392	6.09
11	0.375	0.375	5.63
12	0.361	0.362	5.25
13	0.348	0.349	4.93
14	0.337	0.337	4.66
15	0.326	0.327	4.42
16	0.316	0.317	4.21
17	0.308	0.308	4.02
18	0.299	0.300	3.86
19	0.292	0.292	3.71
20	0.285	0.285	3.58
21	0.278	0.278	3.45
22	0.272	0.272	3.35
23	0.266	0.266	3.24
24	0.260	0.261	3.15
25	0.255	0.255	3.07
26	0.250	0.250	2.98
27	0.244	0.244	2.92
28	0.239	0.239	2.86
29	0.233	0.234	2.81
30	0.228	0.228	2.76
31	0.221	0.222	2.74
32	0.215	0.226	2.72

3.1.2 Uniform meshes of quadratic elements

We considered the mixed boundary-value problem for the Laplace equation in the convex domain $\left(\varphi_1 = \frac{3\pi}{4}\right)$ shown in Fig. 3.1b and applied boundary-conditions consistent with the exact solution $u(r,\theta) = r^\alpha \sin(\alpha\theta)$ for $\alpha = \frac{\pi}{2\varphi_1} = \frac{2}{3}$ and $\alpha = \frac{\pi}{\varphi_1} = \frac{4}{3}$ $\left($for $\alpha = \frac{2}{3}$ homogeneous mixed boundary conditions (resp. for $\alpha = \frac{4}{3}$ homogeneous Dirichlet boundary-conditions) were applied on the edges A_1A_2, A_1A_4 which emanate from the singular point, while Neumann boundary conditions consistent with the exact solution were applied on the rest of the boundary$\right)$ and we computed finite element solutions using uniform meshes of quadratic triangles. In Table 3.3 (resp. Table 3.4) we give the effectivity indices κ_{ω_n} for both estimators in the mesh-layers ω_n, $n = 1,\ldots, \frac{1}{h}$, for $\alpha = \frac{4}{3}$ $\left($resp. $\alpha = \frac{2}{3}\right)$. We note that for $\alpha = \frac{4}{3}$ $\left($resp. $\alpha = \frac{2}{3}\right)$ the effectivity indices in the layers at a fixed distance from the singularity for both estimators converge to one (resp. zero) as the mesh is refined.

3.1.3 Uniform meshes of cubic elements

We also considered the mixed boundary-value problem for the Laplace equation in the triangular domain shown in Fig. 3.1c $\left(\varphi_1 = \frac{5\pi}{12}\right)$ with exact solution $u(r,\theta) = r^\alpha \sin(\alpha\theta)$ for $\alpha = \frac{\pi}{2\varphi_1} = \frac{6}{5}$ and $\alpha = \frac{\pi}{\varphi_1} = \frac{12}{5}$ $\left($for $\alpha = \frac{6}{5}$ homogeneous mixed boundary conditions (resp. for $\alpha = \frac{12}{5}$ homogeneous boundary-conditions) were applied on the edges A_1A_2, A_1A_3 which emanate from the singular point while Neumann boundary conditions consistent with the exact solution were applied on $A_2A_3\right)$ and we computed finite element solutions using uniform meshes of cubic triangles. In Table 3.5 (resp. Table 3.6) we give the effectivity indices for the mesh-layers ω_n for $\alpha = \frac{12}{5}$ $\left($resp. $\alpha = \frac{6}{5}\right)$. We observe that for $\alpha = \frac{12}{5}$ $\left($resp. $\alpha = \frac{6}{5}\right)$ the effectivity indices in the layers at a fixed distance from the singularity converge to one (resp. zero) as the mesh is refined.

3.1.4 Summary of numerical results

From the results we make the following observations. For uniform meshes:

Table 3.3. Pollution error for uniform grids. Convex domain shown in Fig. 3.1b, $\alpha = \frac{4}{3}$, $p = 2$ $(2\alpha > p)$. Effectivity index for the element-residual and ZZ error estimators for each mesh-layer ω_n. Note that the effectivity indices in the interior mesh-layers are close to one.

Effectivity index for each mesh-layer									
Exact solution $u(r,\theta) = r^{\frac{1}{3}}\sin(\frac{4\theta}{3})$; quadratic elements									
Layer number n	$h = \frac{1}{4}$			$h = \frac{1}{8}$			$h = \frac{1}{16}$		
	$\kappa^{ZZ}_{\omega_n}$	$\kappa^{ER}_{\omega_n}$	$\frac{\|\|e_h\|\|_{\omega_n}}{\|\|e_h\|\|_\Omega} \cdot 100$	$\kappa^{ZZ}_{\omega_n}$	$\kappa^{ER}_{\omega_n}$	$\frac{\|\|e_h\|\|_{\omega_n}}{\|\|e_h\|\|_\Omega} \cdot 100$	$\kappa^{ZZ}_{\omega_n}$	$\kappa^{ER}_{\omega_n}$	$\frac{\|\|e_h\|\|_{\omega_n}}{\|\|e_h\|\|_\Omega} \cdot 100$
1	0.663	0.684	86.13	0.666	0.682	82.78	0.667	0.687	82.62
2	0.975	0.956	40.01	0.993	1.062	38.07	1.085	1.063	38.43
3	0.982	0.981	24.14	0.984	0.985	22.18	0.996	0.997	23.62
4	0.971	0.989	18.29	0.975	0.978	16.27	0.976	0.977	17.46
5				0.962	0.964	14.03	0.966	0.969	14.57
6				0.952	0.953	12.15	0.962	0.965	11.23
7				0.945	0.947	10.23	0.959	0.963	10.54
8				0.950	0.976	9.19	0.956	0.960	9.30
9							0.954	0.958	8.41
10							0.952	0.956	7.79
11							0.950	0.953	7.01
12							0.948	0.951	6.23
13							0.945	0.948	5.94
14							0.943	0.945	5.46
15							0.939	0.941	5.21
16							0.939	0.978	5.02

Table 3.3. (continued)

Effectivity index for each mesh-layer			
Exact solution $u(r,\theta) = r^{\frac{2}{3}}\sin(\frac{2\theta}{3})$; quadratic elements			
Layer number n	$h = \frac{1}{32}$		
	$\kappa^{ZZ}_{\omega_n}$	$\kappa^{ER}_{\omega_n}$	$\frac{\|\|\|e_h\|\|\|_{\omega_n}}{\|\|\|e_h\|\|\|_{\Omega}} \cdot 100$
1	0.647	0.682	81.64
2	0.995	1.064	37.99
3	0.997	0.998	23.32
4	0.976	0.977	17.25
5	0.967	0.971	13.87
6	0.964	0.967	11.69
7	0.962	0.965	10.15
8	0.960	0.964	9.00
9	0.959	0.962	8.11
10	0.957	0.960	7.40
11	0.956	0.959	6.81
12	0.954	0.957	6.32
13	0.953	0.955	5.90
14	0.951	0.954	5.54
15	0.950	0.952	5.23
16	0.948	0.950	4.95
17	0.946	0.948	4.71
18	0.945	0.947	4.49
19	0.943	0.944	4.29
20	0.941	0.943	4.12
21	0.939	0.941	3.96
22	0.937	0.939	3.81
23	0.935	0.937	3.68
24	0.933	0.935	3.55
25	0.932	0.933	3.44
26	0.930	0.931	3.33
27	0.927	0.929	3.23
28	0.926	0.927	3.14
29	0.923	0.925	3.06
30	0.921	0.922	2.97
31	0.918	0.919	2.90
32	0.917	0.956	2.83

Table 3.4. Pollution error for uniform grids. Convex domain shown in Fig. 3.1b, $\alpha = \frac{2}{3}$, $p = 2$ $(2\alpha < p)$. Effectivity index for the element-residual and ZZ error estimators for each mesh-layer ω_n. Note that the effectivity indices in the interior mesh-layers are close to zero.

Effectivity index for each mesh-layer									
Exact solution $u(r,\theta) = r^{\frac{2}{3}}\sin(\frac{2\theta}{3})$; quadratic elements									
Layer number n	$h = \frac{1}{4}$			$h = \frac{1}{8}$			$h = \frac{1}{16}$		
	$\kappa^{ZZ}_{\omega_n}$	$\kappa^{ER}_{\omega_n}$	$\frac{\|\|e_h\|\|_{\omega_n}}{\|\|e_h\|\|_\Omega}\cdot 100$	$\kappa^{ZZ}_{\omega_n}$	$\kappa^{ER}_{\omega_n}$	$\frac{\|\|e_h\|\|_{\omega_n}}{\|\|e_h\|\|_\Omega}\cdot 100$	$\kappa^{ZZ}_{\omega_n}$	$\kappa^{ER}_{\omega_n}$	$\frac{\|\|e_h\|\|_{\omega_n}}{\|\|e_h\|\|_\Omega}\cdot 100$
1	0.763	0.635	98.27	0.764	0.635	97.90	0.764	0.635	97.47
2	1.173	0.861	15.37	1.183	0.867	15.22	1.185	0.868	15.13
3	0.588	0.535	8.13	0.599	0.546	7.95	0.601	0.548	7.88
4	0.387	0.352	6.24	0.401	0.382	6.02	0.403	0.384	5.95
5				0.288	0.278	5.15	0.290	0.281	5.09
6				0.218	0.212	4.65	0.220	0.214	4.58
7				0.172	0.168	4.32	0.174	0.170	4.24
8				0.156	0.129	4.08	0.142	0.139	3.99
9							0.118	0.116	3.79
10							0.100	0.099	3.64
11							0.087	0.085	3.50
12							0.076	0.075	3.38
13							0.067	0.066	3.28
14							0.060	0.059	3.19
15							0.054	0.053	3.11
16							0.046	0.045	3.04

Table 3.4. (continued)

Effectivity index for each mesh-layer			
Exact solution $u(r,\theta) = r^{\frac{2}{3}}\sin(\frac{2\theta}{3})$; quadratic elements			
Layer number n	$h = \frac{1}{32}$		
	$\kappa_{\omega_n}^{ZZ}$	$\kappa_{\omega_n}^{ER}$	$\frac{\|\|e_h\|\|_{\omega_n}}{\|\|e_h\|\|_{\Omega}} \cdot 100$
1	0.764	0.635	96.94
2	1.186	0.869	15.04
3	0.602	0.548	7.84
4	0.404	0.384	5.91
5	0.291	0.281	5.05
6	0.221	0.215	4.55
7	0.175	0.170	4.21
8	0.142	0.139	3.96
9	0.118	0.116	3.67
10	0.101	0.099	3.61
11	0.087	0.086	3.47
12	0.076	0.075	3.35
13	0.067	0.066	3.25
14	0.060	0.059	3.16
15	0.054	0.053	3.08
16	0.049	0.048	3.01
17	0.045	0.044	2.94
18	0.041	0.040	2.88
19	0.037	0.037	2.83
20	0.035	0.034	2.77
21	0.032	0.032	2.73
22	0.030	0.030	2.68
23	0.028	0.028	2.64
24	0.026	0.026	2.60
25	0.025	0.025	2.56
26	0.023	0.023	2.53
27	0.022	0.022	2.50
28	0.021	0.021	2.48
29	0.019	0.019	2.46
30	0.016	0.016	2.44
31	0.013	0.013	2.43
32	0.011	0.011	2.42

Table 3.5. Pollution error for uniform grids. Triangular domain shown in Fig. 3.1c, $\alpha = \frac{12}{5}$, $p = 3$ ($2\alpha > p$). Effectivity index for the element-residual and ZZ error estimators for each mesh-layer ω_n. Note that the effectivity indices in the interior mesh-layers are close to one.

Effectivity index for each mesh-layer									
Exact solution $u(r,\theta) = r^{\frac{12}{5}} \sin(\frac{12\theta}{5})$; cubic elements									
Layer number n	$h = \frac{1}{4}$			$h = \frac{1}{8}$			$h = \frac{1}{16}$		
	$\kappa^{ZZ}_{\omega_n}$	$\kappa^{ER}_{\omega_n}$	$\frac{\|\|e_h\|\|_{\omega_n}}{\|\|e_h\|\|_\Omega} \cdot 100$	$\kappa^{ZZ}_{\omega_n}$	$\kappa^{ER}_{\omega_n}$	$\frac{\|\|e_h\|\|_{\omega_n}}{\|\|e_h\|\|_\Omega} \cdot 100$	$\kappa^{ZZ}_{\omega_n}$	$\kappa^{ER}_{\omega_n}$	$\frac{\|\|e_h\|\|_{\omega_n}}{\|\|e_h\|\|_\Omega} \cdot 100$
1	0.763	0.784	86.23	0.766	0.786	83.88	0.767	0.787	82.50
2	0.996	0.996	40.11	0.993	0.992	39.01	0.985	0.983	38.38
3	0.984	0.983	24.74	0.985	0.986	23.98	0.987	0.988	23.56
4	0.970	0.991	18.49	0.971	0.972	17.77	0.976	0.977	17.43
5				0.959	0.962	14.33	0.966	0.969	14.03
6				0.951	0.955	12.10	0.962	0.965	11.83
7				0.945	0.949	10.53	0.959	0.963	10.27
8				0.948	0.984	9.39	0.956	0.960	9.12
9							0.954	0.958	8.22
10							0.952	0.956	7.50
11							0.950	0.953	6.91
12							0.948	0.951	6.42
13							0.945	0.948	6.00
14							0.943	0.945	5.64
15							0.939	0.941	5.33
16							0.939	0.978	5.06

Table 3.6. Pollution error for uniform grids. Triangular domain shown in Fig. 3.1c, $\alpha = \frac{6}{5}$, $p = 3$ ($2\alpha < p$). Effectivity index for the element-residual and ZZ error estimators for each mesh-layer ω_n. Note that the effectivity indices in the interior mesh-layers are close to zero.

Effectivity index for each mesh-layer									
Exact solution $u(r,\theta) = r^{\frac{6}{5}}\sin(\frac{6\theta}{5})$; cubic elements									
Layer number n	$h = \frac{1}{4}$			$h = \frac{1}{8}$			$h = \frac{1}{16}$		
	$\kappa^{ZZ}_{\omega_n}$	$\kappa^{ER}_{\omega_n}$	$\frac{\|\|e_\Delta\|\|_{\omega_n}}{\|\|e_\Delta\|\|_\Omega} \cdot 100$	$\kappa^{ZZ}_{\omega_n}$	$\kappa^{ER}_{\omega_n}$	$\frac{\|\|e_\Delta\|\|_{\omega_n}}{\|\|e_\Delta\|\|_\Omega} \cdot 100$	$\kappa^{ZZ}_{\omega_n}$	$\kappa^{ER}_{\omega_n}$	$\frac{\|\|e_\Delta\|\|_{\omega_n}}{\|\|e_\Delta\|\|_\Omega} \cdot 100$
1	0.663	0.535	99.07	0.664	0.535	97.90	0.664	0.535	97.47
2	0.863	0.761	14.87	0.883	0.767	15.22	0.885	0.768	15.13
3	0.481	0.441	8.53	0.499	0.446	7.95	0.401	0.448	7.88
4	0.227	0.232	6.54	0.301	0.282	6.02	0.303	0.284	5.95
5				0.188	0.178	5.15	0.190	0.181	5.09
6				0.118	0.112	4.65	0.120	0.114	4.58
7				0.072	0.068	4.32	0.074	0.070	4.24
8				0.056	0.029	4.08	0.042	0.039	3.99
9							0.018	0.016	3.79
10							0.009	0.009	3.64
11							0.008	0.008	3.50
12							0.007	0.007	3.38
13							0.007	0.006	3.28
14							0.006	0.006	3.19
15							0.005	0.005	3.11
16							0.005	0.005	3.04

(i). The pollution-effect depends on a relationship between the exponent α of the singularity and the polynomial degree p of the elements.

(ii). The pollution-effect for fixed mesh-size h and for fixed exponent α becomes more significant as the polynomial degree p of the elements is increased.

(iii). For elements of quadratic degree or higher the pollution-effect in finite-element solutions of the Laplacian exists even for convex domains.

The same conclusions are expected to hold for the class of quasi-uniform meshes which are often used in practical computations.

3.2 Analysis of the pollution-effect for uniform meshes.

3.2.1 Preliminaries

Let us assume that the mesh is uniform as in the examples. (The analysis holds for the broader class of quasi-uniform meshes. The majority of the grids employed in the practical computations are quasiuniform). The error $e_h = u - u_h$ is the solution of the following boundary-value problem

$$-\Delta e_h = \sum_{\tau \in T_h} \Big(\sum_{\epsilon \subseteq \partial \tau} \bar{J}_\epsilon^\tau + r_\tau \Big) \quad \text{in} \quad \Omega \tag{3.1a}$$

$$\frac{\partial e_h}{\partial n} = 0 \qquad \text{on} \quad \Gamma_N \tag{3.1b}$$

$$e_h = 0 \qquad \text{on} \quad \Gamma_D \tag{3.1c}$$

The variational form of this problem was given above in (2.6) (the residual equation). Here by $\bar{J}_\epsilon^\tau$ we denote the Dirac function (line-load) on the edge ϵ associated with the element τ i.e.

$$\int_\tau v \bar{J}_\epsilon^\tau = \sum_{\epsilon \subseteq \partial \tau} \int_\epsilon v \, \frac{1}{2} \, J_\epsilon \tag{3.2}$$

where J_ϵ was defined in (2.7). By the equilibration procedure described in Section 2.2.1 (which can be extended to elements of any degree p) we can rewrite (the right-hand side of) (3.1a) in the form

$$-\Delta e_h = \sum_{\tau \in T_h} \rho_\tau \tag{3.3a}$$

where

$$\rho_\tau = r_\tau + \sum_{\epsilon \subsetneq \partial\tau} \hat{J}_\epsilon^\tau \tag{3.3b}$$

where $\hat{J}_\epsilon^\tau$ are the Dirac functions analogous as before and such that

$$\int_\tau v\hat{J}_\epsilon^\tau = \sum_{\epsilon \subsetneq \partial\tau} \int_\epsilon v\left(\frac{1}{2}J_\epsilon + \theta_\tau\right) \tag{3.4a}$$

and

$$\int_\tau \rho_\tau v = 0 \qquad \forall\ v \in \mathcal{P}_p \tag{3.4b}$$

as a result of the equilibrations (here we assume p-degree equilibrations of the residuals). From (3.4) it follows that $\int_\tau \rho_\tau = 0$ and hence there exists $\tilde{e}_\tau \in H^1(\tau)$ such that

$$B_\tau(\tilde{e}_\tau, v) = \int_\tau \rho_\tau v \qquad \forall\ v \in H^1(\tau) \tag{3.5}$$

Further we have

$$|||e_h|||_\Omega = \sup_{v \in H^1_{\Gamma_D}} \frac{\left|\sum_{\tau \in T_h} \int_\tau \rho_\tau v\right|}{|||v|||_\Omega} = \sup_{v \in H^1_{\Gamma_D}} \frac{\left|\sum_{\tau \in T_h} B_\tau(\tilde{e}_\tau, v)\right|}{|||v|||_\Omega} \leq \left(\sum_{\tau \in T_h} |||\tilde{e}_\tau|||_\tau^2\right)^{\frac{1}{2}} \tag{3.6}$$

where $\tilde{e}_\tau$ denotes the exact solution of the *equilibrated element residual problem* (3.5).

Let us now define $W_\tau \in H^1_{\Gamma_D}$ such that

$$-\Delta W_\tau = \rho_\tau \quad \text{in} \quad \Omega \tag{3.7a}$$

$$\frac{\partial W_\tau}{\partial n} = 0 \quad \text{on} \quad \Gamma_N \tag{3.7b}$$

$$W_\tau = 0 \quad \text{on} \quad \Gamma_D \tag{3.7c}$$

We have by *superposition*

$$e_h(x) = \sum_{\tau \in T_h} W_\tau(x) \qquad \forall\ x \in \Omega \tag{3.8}$$

Let τ_0 be an element of interest and denote by $\Phi^{(m)}(\tau_0)$ the set of elements in m-layers around τ_0, including τ_0

$$\Phi^{(m)}(\tau_0) := \left\{ \tau \in T_h \quad | \quad \tau \subseteq \mathcal{N}_h^m(\tau_0) \right\}, \qquad \Phi^{(0)}(\tau_0) := \left\{ \tau_0 \right\} \tag{3.9a}$$

where

$$\mathcal{N}_h^m(\tau_0) := \bigcup_{\tau' \in \Phi^{(m-1)}(\tau_0)} \left(\bigcup_{X \in N(\tau')} \mathcal{N}_X \right), \quad \mathcal{N}_h^0(\tau_0) = \tau_0, \quad \mathcal{N}_X := \bigcup_{X \in N(\tau'')} \tau'' \tag{3.9b}$$

Here $N(\tau)$ is the set of the three vertices of triangle τ. We let

$$V_1^{(m)}(\tau_0) := \sum_{\tau \in \Phi^{(m)}(\tau_0)} W_\tau, \qquad V_2^{(m)}(\tau_0) := \sum_{\tau \notin \Phi^{(m)}(\tau_0)} W_\tau \tag{3.10a}$$

and by superposition

$$V_1^{(m)}(\tau_0) + V_2^{(m)}(\tau_0) = e_h \tag{3.10b}$$

We define the norms

$$\Psi_1^{(m)}(\tau_0) := |||V_1^{(m)}(\tau_0)|||_{\tau_0}, \qquad \Psi_2^{(m)}(\tau_0) := |||V_2^{(m)}(\tau_0)|||_{\tau_0}, \tag{3.11a}$$

$$\Psi(\tau_0) = |||V_1^{(m)}(\tau_0) + V_2^{(m)}(\tau_0)|||_{\tau_0} = |||e_h|||_{\tau_0} \tag{3.11b}$$

It is easy to see that, from the complementary variational principle,

$$\eta_\tau := |||\tilde{e}_{\tau_0}|||_{\tau_0} \geq \Psi_1^{(0)}(\tau_0) \tag{3.12}$$

where $\tilde{e}_{\tau_0}$ denotes the *exact solution* of the local problem (3.4).

Remark 3.1. Here $V_1^{(m)}(\tau_0)$ is the component of the error which is due to the residuals in the element τ_0 and m-layers of elements around it. Analogously, $V_2^{(m)}(\tau_0)$ is the component of the error due to the residuals in the elements outside the m-layer neighborhood $\Phi^{(m)}(\tau_0)$ of τ_0.

3.2.2 The near-field pollution

In general, the error in an element is influenced by the residuals in the entire mesh. However, when the solution is smooth, and the mesh is uniform, the error in an element τ_0 is, for all practical purposes, influenced only by the residuals in τ_0 and in a few mesh-layers of elements around τ_0. The effect of the residuals in a few mesh-layers of elements around τ_0 on the error in τ_0 will be referred to as the *near-field pollution*. Analogously the influence of the residuals beyond a few mesh-layers of elements around τ_0 on the error in τ_0 will be referred to as the *far-field pollution*. Below we show results which indicate that *the near-field pollution is fully accounted for by robust local error estimators.*

We considered various meshes shown in Fig. 3.2a-3.2d, in which the element τ_0 is shaded black and a few mesh-layers around τ_0 are shaded gray. We computed the norms defined in (3.11a) first by considering only the residuals in the element τ_0 and then, in progression, the residuals in all the elements in $\bar{\Phi}^{(m)}(\tau_0)$ for $m = 1, 2, 3, \ldots$. We computed the values of the *pollution factor for the energy*:

$$\mu_{\tau_0}^{2,(m)}\% := \frac{|||V_1^{(m)}(\tau_0)|||^2}{|||V_1^{(m)}(\tau_0)|||^2 + |||V_2^{(m)}(\tau_0)|||^2} \cdot 100 \tag{3.13}$$

In Table 3.7a we give the values of $\mu_{\tau_0}^{2,(m)}\%$ for $p = 1$, 2, 3 for the Regular mesh-pattern shown in Fig. 3.2a. In Table 3.7b we give the values of $\mu_{\tau_0}^{2,(m)}\%$ for $p = 1$, 2, 3 for the Criss-Cross mesh-pattern shown in Fig. 3.2b. In Table 3.7c we give the results for $p = 1$, 2, 3 for the mesh-pattern shown in Fig. 3.2c and in Table 3.7d we give the values of $\mu_{\tau_0}^{2,(m)}\%$ for $p = 1$, 2, 3 for the mesh-pattern shown in Fig. 3.2d. We also see that $\Psi_1^{(0)}(\tau_0)$ is significantly smaller than the exact values of $|||e_h|||_{\tau_0}$. Note that the factor $\mu_{\tau_0}^{2,(m)\%}$ converges to 100% when the residuals in two layers of elements around τ_0 are considered. Also note that as the polynomial degree p of the elements is increased, the ratio $\mu_{\tau_0}^{2,(m)}\%$ is practically equal to 100% for $m \geq 1$.

Hence we have $\Psi_1^{(2)}(\tau_0) \approx |||e_h|||_{\tau_0}$ for the mesh-patterns considered and since $\frac{1}{C_U^{\tau_0}} |||e_h|||_{\tau_0} \leq \eta_{\tau_0} \leq \frac{1}{C_L^{\tau_0}} |||e_h|||_{\tau_0}$ for constants $C_L^{\tau_0}$, $C_U^{\tau_0}$ close to 1, (see Section 2.3) we have $\eta_{\tau_0} \approx |||V_1^{(2)}(\tau_0)|||_{\tau_0}$, for both the *ER*-estimator with equilibrated data and the *ZZ*-estimator. Moreover since $|||e_h|||_{\tau_0} = |||V_1^{(m)}(\tau_0) + V_2^{(m)}(\tau_0)|||_{\tau_0}$ we have $\eta_{\tau_0} \approx |||e_h|||_{\tau_0}$ only if $|||V_2^{(m)}|||_{\tau_0} \ll |||V_1^{(m)}|||_{\tau_0}$. Hence $|||V_2^{(m)}|||_{\tau_0}$ expresses the far-field pollution, or, in other words η_{τ_0} is an estimate of $|||u_h - (u - V_2^{(m)})|||_{\tau_0}$ i.e. it estimates how close u_h is to $u - V_2^{(m)}$ (where $m = 2$ for the mesh-patterns considered here).

From the numerical results of this Section we can infer that: When the solution is smooth and the mesh is periodic we have

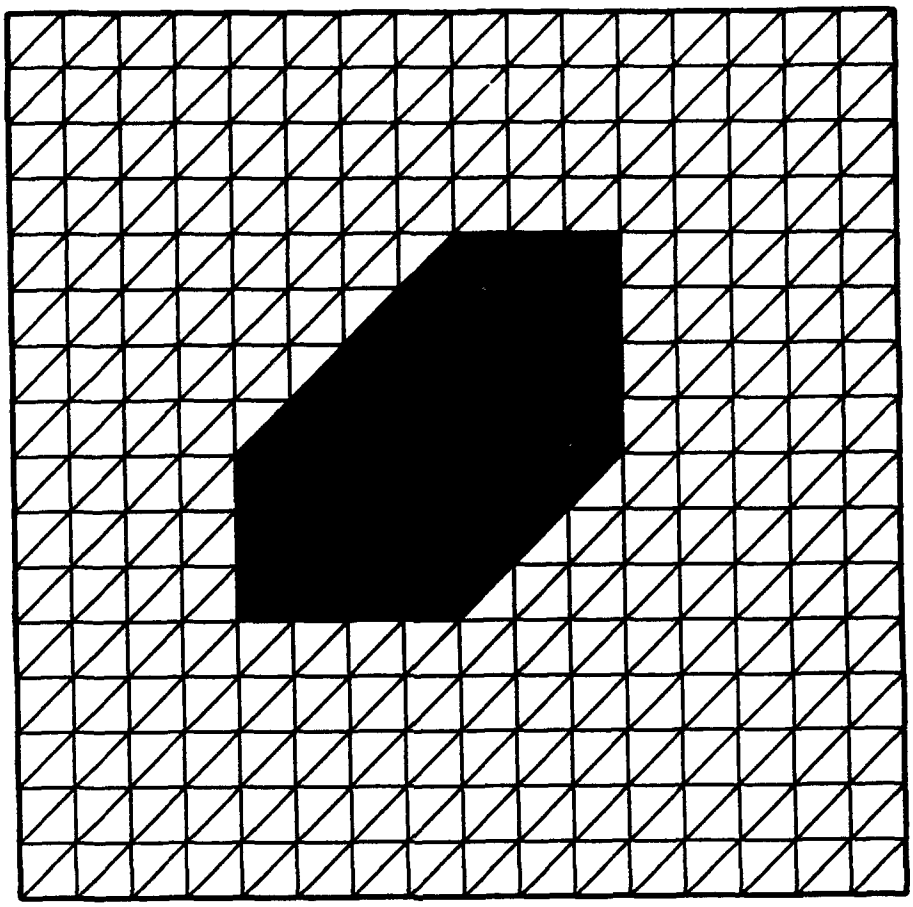

(a)

Figure 3.2. Uniform grids of different patterns with the element τ_0 shaded black and a few mesh-layers around τ_0 shaded in different shades of gray. (a) Regular mesh-pattern; (b) Criss-Cross mesh-pattern; (c) Special mesh-pattern 1; (d) Special-mesh-pattern 2.

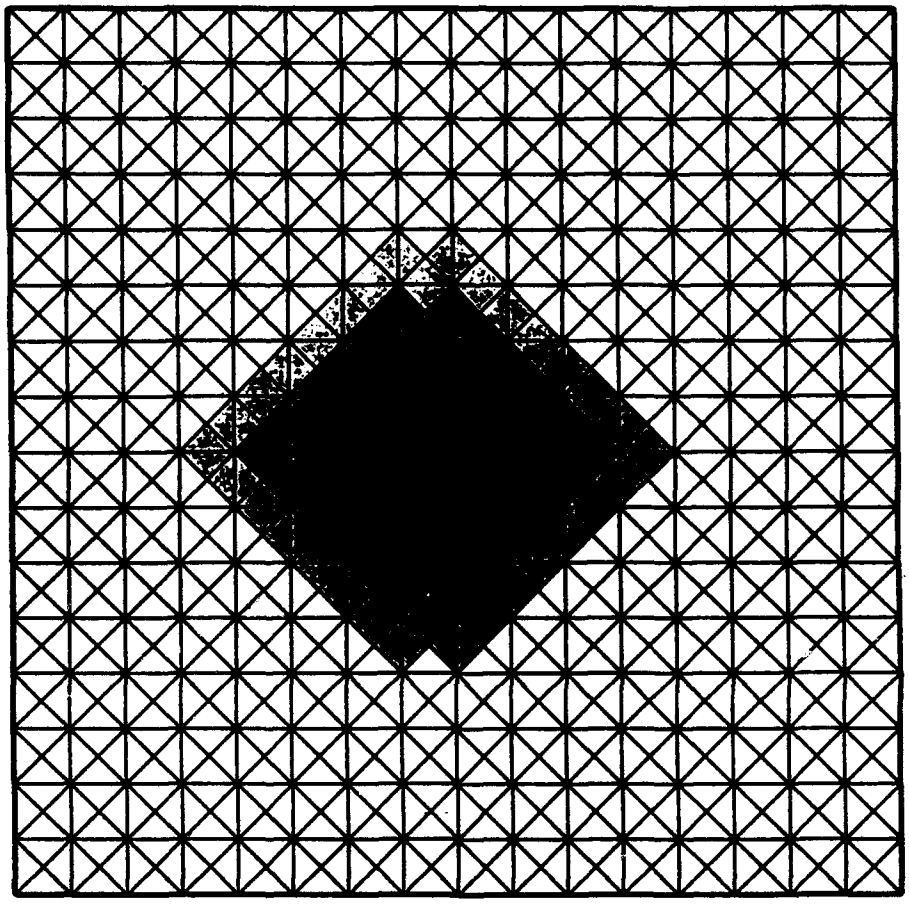

(b)

Figure 3.2. (continued)

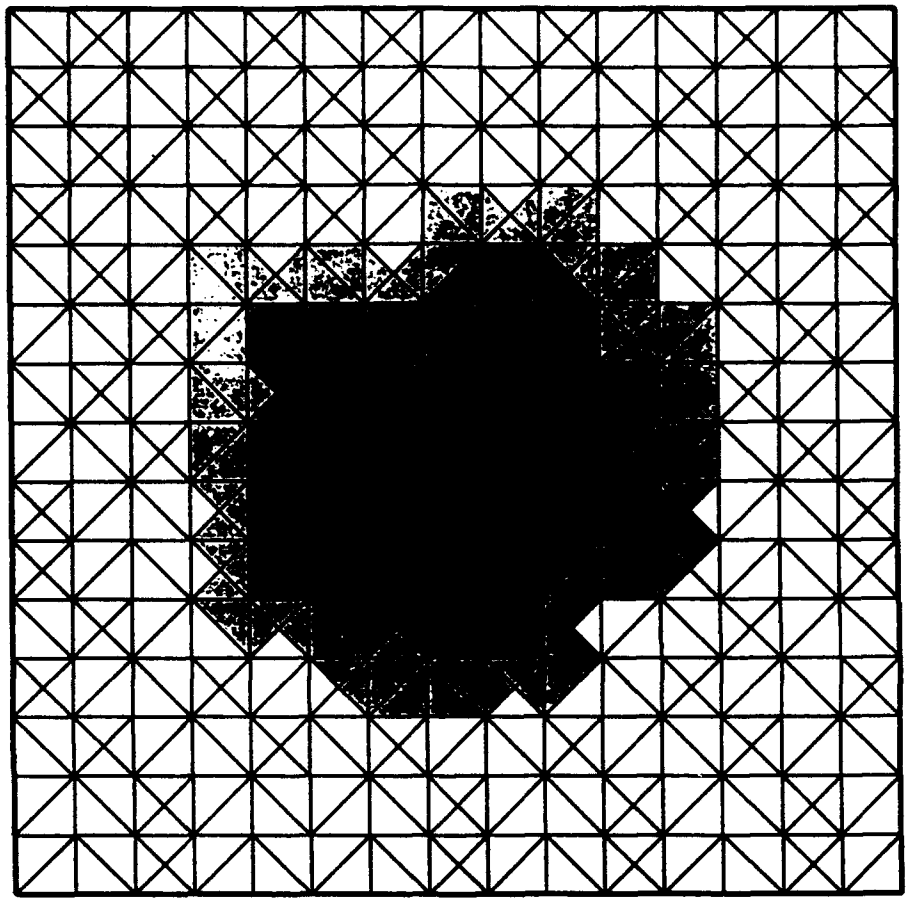

(c)

Figure 3.2. (continued)

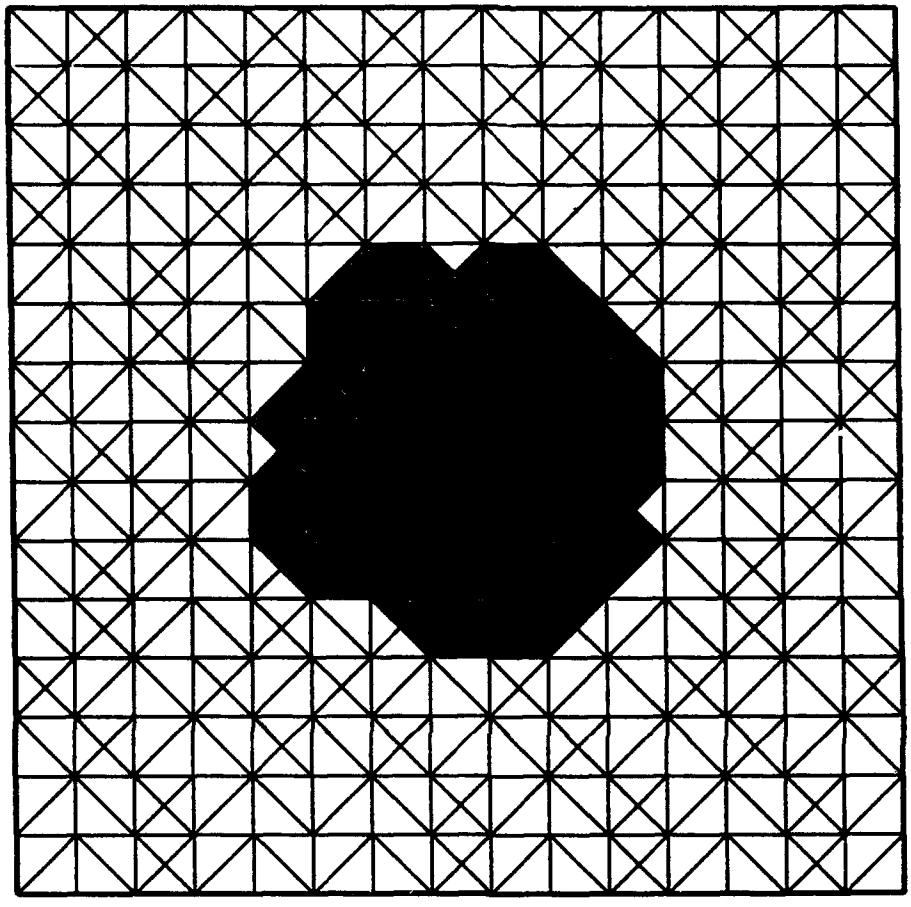

(d)

Figure 3.2. (continued)

Table 3.7a. Effect of the near field pollution: Pollution factor for the energy of the error in the element τ_0 due to the residuals in m mesh-layers surrounding τ_0 for the mesh shown in Fig. 3.2a. Note that the percentage of the energy of the error in τ_0 approaches 100% when the residuals in the first layer surrounding τ_0 are included.

Pollution factor for the energy of the error in the element τ_0 due to the residuals in m mesh-layers around τ_0.			
Regular mesh-pattern			
Number of Layers m	$\frac{\|\|\|V_1^{(m)}(\tau_0)\|\|\|^2}{\|\|\|V_1^{(m)}(\tau_0)\|\|\|^2 + \|\|\|V_2^{(m)}(\tau_0)\|\|\|^2} \times 100$		
	$p=1$	$p=2$	$p=3$
0	66.92	74.87	76.64
1	84.44	97.60	99.99
2	99.98	99.99	99.99
3	99.99	99.99	99.99

Table 3.7b. Effect of the near field pollution: Pollution factor for the energy of the error in the element τ_0 due to the residuals in m mesh-layers surrounding τ_0 for the mesh shown in Fig. 3.2b. Note that the percentage of the energy of the error in τ_0 approaches 100% when the residuals in two layers surrounding τ_0 are included.

Pollution factor for the energy of the error in the element τ_0 due to the residuals in m mesh-layers around τ_0.			
Criss-Cross mesh-pattern			
Number of Layers m	$\frac{\|\|\|V_1^{(m)}(\tau_0)\|\|\|^2}{\|\|\|V_1^{(m)}(\tau_0)\|\|\|^2 + \|\|\|V_2^{(m)}(\tau_0)\|\|\|^2} \times 100$		
	$p=1$	$p=2$	$p=3$
0	77.07	69.28	78.86
1	94.03	96.03	99.99
2	99.99	99.99	99.99
3	99.99	99.99	99.99

Table 3.7c. Effect of the near field pollution: Pollution factor for the energy of the error in the element τ_0 due to the residuals in m mesh-layers surrounding τ_0 for the mesh shown in Fig. 3.2c. Note that the percentage of the energy of the error in τ_0 approaches 100% when the residuals in two layers surrounding τ_0 are included.

Pollution factor for the energy of the error in the element τ_0 due to the residuals in m mesh-layers around τ_0.			
Special mesh-pattern shown in Fig. 3.2c			
Number of Layers m	$\dfrac{\|\|\|V_1^{(m)}(\tau_0)\|\|\|^2}{\|\|\|V_1^{(m)}(\tau_0)\|\|\|^2 + \|\|\|V_2^{(m)}(\tau_0)\|\|\|^2} \times 100$		
	$p=1$	$p=2$	$p=3$
0	66.73	78.94	79.43
1	92.00	94.06	98.00
2	99.99	99.99	99.99
3	99.99	99.99	99.99

Table 3.7d. Effect of the near field pollution: Pollution factor for the energy of the error in the element τ_0 due to the residuals in m mesh-layers surrounding τ_0 for the mesh shown in Fig. 3.2d. Note that the percentage of the energy of the error in τ_0 approaches 100% when the residuals in two layers surrounding τ_0 are included.

Pollution factor for the energy of the error in the element τ_0 due to the residuals in m mesh-layers around τ_0.			
Special mesh-pattern shown in Fig. 3.2d			
Number of Layers m	$\dfrac{\|\|\|V_1^{(m)}(\tau_0)\|\|\|^2}{\|\|\|V_1^{(m)}(\tau_0)\|\|\|^2 + \|\|\|V_2^{(m)}(\tau_0)\|\|\|^2} \times 100$		
	$p=1$	$p=2$	$p=3$
0	74.56	82.15	83.04
1	93.89	97.97	98.36
2	99.98	99.99	99.99
3	99.99	99.99	99.99

$$\eta_{\tau_0} \approx |||V_1^{(m)}(\tau_0)|||_{\tau_0} \approx |||e_h|||_{\tau_0}, \qquad \text{for} \quad m \geq m_0$$

for every interior element $\tau_0 \in T_h$ where m_0 denotes the numbers of layers of elements around τ_0 (including τ_0) for which the element-residuals are responsible (for all practical purposes) for the error in τ_0 (for the meshes considered above it is sufficient to take $m_0 = 2$). In other words when the solution is smooth and the mesh is periodic, an error estimator takes into account the residuals in all mesh-layers around any interior element.

So far we addressed the energy-norm $|||\cdot|||_{\tau_0}$ in an element τ_0; of course the result will hold if we replace τ_0 by a patch of elements ω^h and replace $\Phi^{(m)}(\tau_0)$ by $\Phi^{(m)}(\omega^h)$ with the obvious meaning.

3.2.3 Asymptotics of the pollution-effect for uniform meshes

Let us now analyze the asymptotics of the pollution. Given $x \in \Omega$ we can write

$$\frac{\partial V_1^{(m)}}{\partial x_i}(\tau_0)(x) = \sum_{\tau \in \Phi^{(m)}(\tau_0)} \int_\tau \rho_\tau \, G_i(x), \qquad i = 1, 2 \tag{3.14a}$$

$$\frac{\partial V_2^{(m)}}{\partial x_i}(\tau_0)(x) = \sum_{\tau \notin \Phi^{(m)}(\tau_0)} \int_\tau \rho_\tau \, G_i(x), \qquad i = 1, 2 \tag{3.14b}$$

where $G_i(x)$ is the x_i-derivative of the Green's function and the integrals have to be understood in the proper sense. We have for $m > 0$

$$|D^m G_i(x)| \leq \frac{C}{R^m} \qquad \text{on} \quad \Omega(x; R) := \Omega - O(x; R) \tag{3.15}$$

provided that Ω is a rectangle and either $\Gamma_N = \emptyset$ or $\Gamma_D = \emptyset$. (For general polygonal domains (3.15) holds for $m < \bar{m}$, where $\bar{m}$ depends on the angles and the type of boundary-conditions.)

Assuming that the exact solution u is smooth we have

$$C_1 h^p \leq \Big(\sum_{\tau \in T_h} \eta_\tau^2 \Big)^{\frac{1}{2}} \leq C_2 h^p \tag{3.16}$$

Assume now that $\bigcup_{\tau \in \Phi^{(m)}(\tau_0)} \bar{\tau} \supset O(x, R)$ and using (3.4) we have

$$\Big| \frac{\partial V_2^{(m)}}{\partial x_i}(\tau_0)(x) \Big| = \Big| \sum_{\tau \in \Phi^{(m)}(\tau_0)} \int_\tau \rho_\tau G_i(x) \Big| = \Big| \sum_{\tau \in \Phi^{(m)}(\tau_0)} \rho_\tau (G_i(x) - \chi) \Big| \tag{3.17}$$

for every $\chi \in S^p_{h,\Gamma_D}$. Now using (3.15) we see that we can select χ_0 such that on τ_0 we have

$$\int_{\tau_0} (G_i^x - \chi_0) = 0 \tag{3.18a}$$

and

$$\left|\frac{\partial}{\partial x_i} G_i(x) - \chi_0\right| \leq C \frac{h^p}{R^{p+1}} \tag{3.18b}$$

Hence

$$\left|\frac{\partial V_2^{(m)}}{\partial x_i}(\tau_0)(x)\right| = \left| \sum_{\substack{\tau \in T_h \\ \tau \notin \phi^{(m)}(\tau_0)}} \int_\tau \rho_\tau (G_i(x) - \chi_0)\right| =$$

$$= \left| \sum_{\substack{\tau \in T_h \\ \tau \notin \phi^{(m)}(\tau_0)}} B_\tau(\tilde{e}_\tau, G_i(x) - \chi_0)\right| \leq \Big(\sum_{\substack{\tau \in T_h \\ \tau \notin \phi^{(m)}(\tau_0)}} \eta_\tau^2 \Big)^{\frac{1}{2}} C \frac{h^p}{R^{p+1}} \leq C h^{2p} \tag{3.19}$$

and hence

$$\left\| \frac{\partial}{\partial x_i} V_2^{(m)}(\tau_0)\right\|_\tau \leq C \frac{h^{2p+1}}{R^{p+1}} \tag{3.20}$$

Because $|||e_h||| \geq C h^{p+1}$ we see that if we select $R \geq h^{\frac{p-i}{p+1}}$ the pollution is negligible asymptotically.

In the above argument we used the assumption that the solution u was smooth $\Big($and hence $(\sum_{\tau \in T_h} \eta_\tau^2)^{\frac{1}{2}} \leq C h^p\Big)$. If the domain is convex and either Γ_N or Γ_D is empty then (3.16) holds for $p = 1$. Assume now that the domain is not convex or that we have mixed boundary-conditions. Then we have

$$\left|\frac{\partial V_2^{(m)}}{\partial x_1}(\tau_0)(x)\right| \leq \frac{C h^{2\alpha}}{R^2}, \qquad i = 1, 2 \tag{3.21}$$

and hence

$$|||V_2^{(m)}(\tau_0)|||_{\tau_0} \leq \frac{C h^{2\alpha+1}}{R^2} \tag{3.22}$$

Because

$$|||e_h|||_{\tau_0} \geq Ch^{p+1} \tag{3.23}$$

we see that if $\alpha < \frac{1}{2p}$ then the pollution may be significant.

Remark 3.2. In the proof of (3.22) we employed the fact that the Green's function $G(x)$ and its derivatives $G_i(x)$, $i = 1, 2$, are singular in the neighborhood of the vertices A_i (see Fig. 2.1). Because of this singular behavior the exponent $(2\alpha + 1)$ in (3.22) is independent of p. We have proven in (3.21) the upper estimate. It is possible to prove similarly, as in the theorem 13.1 of [65], that the estimate (3.21) is sharp i.e. that the coefficient 2α cannot be improved, in general.

Remark 3.3. The estimation of V_2 in a non-asymptotic way can be made only using an a-posteriori method. This will be addressed in a forthcoming paper.

3.2.4 Discussion of the numerical results in the context of the asymptotic analysis.

In Section 3.1 we gave numerical results which indicate the effect of the pollution error on the local quality of the error estimators. We now discuss the results of Section 3.1 based on the asymptotic analysis given above.

We define the *pollution factors* for a mesh-cell ω^h

$$\mu_{\omega^h}^{(m)}\% = \frac{|||V_2^{(m)}(\omega^h)|||_{\omega^h}}{\sqrt{|||V_1^{(m)}(\omega^h)|||_{\omega^h}^2 + |||V_2^{(m)}(\omega^h)|||_{\omega^h}^2}} 100\% \tag{3.24}$$

and

$$\xi_{\omega^h}^{(m)}\% = \frac{|||V_2^{(m)}(\omega^h)|||_{\omega^h}}{|||V_1^{(m)}(\omega^h)|||_{\omega^h}^2} 100\% \tag{3.25}$$

Obviously if $\xi_{\omega^h}^{(m)}$ is small then $\mu_{\omega^h}^{(m)} \approx \xi_{\omega^h}^{(m)}$. We see now that the pollution in ω^h is negligible if $\mu_{\omega^h}^{(m)}$ and $\xi_{\omega^h}^{(m)}$ are small (more precisely if $\xi_{\omega^h}^{(m)} \longrightarrow 0$ as $h \longrightarrow 0$).

According to the asymptotic analysis the effect of the pollution is negligible asymptotically only when $2\alpha > p$. On the other hand when $2\alpha < p$ the pollution error is the significant part of the total error (asymptotically) in the interior of the mesh; in that case the effectivity index for any estimator (which is based on local computations), for elements in the interior of the mesh, converges to zero.

For the example problems given in Section 3.1 we considered interior mesh-cells ω_0^h and we computed the components $V_1^{(m)}(\omega_0^h)$ and $V_2^{(m)}(\omega_0^h)$ of the error e_h and their energies $|||V_1^{(m)}(\omega_0^h)|||_{\omega_0^h}^2$, $|||V_2^{(m)}(\omega_0^h)|||_{\omega_0^h}^2$. Let Ω_0 denote a fixed subdomain

which includes ω_0^h in its interior; we may assume that the mesh T_h is such that Ω_0 is always exactly covered by the elements which intersect it. We let

$$V_1(\Omega_0)(x) := \sum_{\substack{\tau \in T_h \\ \tau \subseteq \Omega_0}} \int_\tau \rho_\tau \, G(x), \qquad V_2(\Omega_0)(x) := \sum_{\substack{\tau \in T_h \\ \tau \not\subseteq \Omega_0}} \int_\tau \rho_\tau \, G(x) \tag{3.26}$$

Below, for simplicity, we will omit Ω_0 from most appearances of V_1, V_2. We note that V_1 and V_2 satisfy the following variational problems:

(a) Find $V_1 \in H^1_{\Gamma_D}(\Omega)$, and

$$B_\Omega(V_1, v) = \sum_{\substack{\tau \subseteq \Omega_0 \\ \tau \in T_h}} F_\tau(v) \qquad \forall\ v \in H^1_{\Gamma_D} \tag{3.27a}$$

(b) Find $V_2 \in H^1_{\Gamma_D}(\Omega)$ such that

$$B_\Omega(V_2, v) = \sum_{\tau \subseteq \Omega - \Omega_0} F_\tau(v) \qquad \forall\ v \in H^1_{\Gamma_D} \tag{3.27b}$$

We note that for mesh-cells $\omega_0^h \subset \Omega_0$ which are separated by two (or more) mesh-layers from the boundary of Ω_0 we have

$$V_1^{(2)}(\omega_0^h) \approx V_1(\Omega_0)\big|_{\omega_0^h}, \qquad V_2^{(2)}(\omega_0^h) \approx V_2(\Omega_0)\big|_{\omega_0^h} \tag{3.28}$$

Thus, the functions V_1 and V_2 are practically the same as $V_1^{(2)}(\omega_0^h)$, $V_2^{(2)}(\omega_0^h)$, for all mesh-cells ω_0^h which are separated by two or more mesh-layers from the boundary of the subdomain Ω_0. Based on the analysis given above we say that the pollution is significant if the ratio $\mu^{\%}_{\omega_0^h}$ is close to 100%. (The pollution-factor is defined as in (3.24) where $V_1(\Omega_0)\big|_{\omega_0^h}$, $V_2(\Omega_0)\big|_{\omega_0^h}$ may be employed instead of $V_1^{(m)}(\omega_0^h)$, $V_2^{(m)}(\omega_0^h)$.) We will refer to $\mu^{\%}_{\omega_0^h}$ as the *percentage of pollution* in the mesh-cell ω_0^h.

We considered a *shrinking* eight element mesh-cell $\omega_0^h \subset \Omega_0$ which consists of the eight elements in the h-neighborhood of the center x^0 of the subdomain Ω_0

$$S(x^0, h) := \left\{ x = (x_1, x_2) \,\middle|\, \max(|x_1 - x_1^0|,\ |x_2 - x_2^0|) < h \right\} \tag{3.29}$$

(Note that in all the examples below we consider square subdomains Ω_0). We computed V_1 and V_2 in two different ways:

a. Least-squares fit (smoothing)

We let $V_2 = u - w$ and $V_1 = e_h - V_2$, where w is the limit function to which u_h converges in the neighborhood of x^0 as h tends to zero. The function w is approximated by letting

$$w(x) \approx \alpha_0 + \sum_{k=1}^{q} \left(\alpha_1^k Q_1^k(x - x^0) + \alpha_2^k Q_2^k(x - x^0) \right), \qquad (3.30a)$$

where

$$Q_1^k(x) = \mathcal{R}e(z^k), \quad Q_2^k(x) = \mathcal{I}m(z^k), \quad z = x_1 + ix_2, \; x = (x_1, x_2) \qquad (3.30b)$$

and by employing a least-squares fit of the above expression to the values of u_h in Ω_0 to determine the coefficients.

b. Approximation of V_1, V_2 using a global higher-order approximation

We can approximate V_1, V_2 by solving directly the residual equations (3.28a) (resp. (3.28b)) satisfied by V_1 (resp. V_2) using a finite-element approximation of degree $q > p$ on the same mesh used to approximate u_h (we call this q-degree approximation an *overkill*).

In the results below we report the values of the pollution factors $\mu_{\omega_0^h}\%$, $\xi_{\omega_0^h}^{\%}$, the effectivity index $\kappa_{\omega_0^h}$ and the effectivity index $\kappa'_{\omega_0^h} := \dfrac{\mathcal{E}_{\omega_0^h}}{|||V_1|||_{\omega_0^h}}$ for the shrinking eight-element mesh-cell located at the center of the subdomain Ω_0.

3.2.4.1. Uniform meshes of linear elements.

In Tables 3.8a, 3.8b we give the values of $|||V_1|||^2_{\omega_0^h}$, $|||V_2|||^2_{\omega_0^h}$ and $\int_{\omega_0^h} \nabla V_1 \cdot \nabla V_2$, the values of the pollution factors $\mu^{\%}_{\omega_0^h}$ and $\xi^{\%}_{\omega_0^h}$, and the effectivity indices $\kappa_{\omega_0^h}$ and $\kappa'_{\omega_0^h}$ for the two estimators for linear elements ($p = 1$) and $\alpha = \dfrac{2}{3}$ ($2\alpha > p$). Note that the pollution factors $\mu^{\%}_{\omega_0^h}$ and $\xi^{\%}_{\omega_0^h}$ converge to zero and the effectivity indices $\kappa_{\omega_0^h}$ and $\kappa'_{\omega_0^h}$ (for both estimators) converge to one as the mesh-size tends to zero. Hence for $\alpha = \dfrac{2}{3}$ there is no pollution for linear elements, asymptotically. In Fig. 3.3 (resp. Fig. 3.4) we show the directional derivatives of the V_1- and V_2-components of the error along the s-axis shown in Fig. 3.1a, for $h = 0.125$ (resp. $h = 0.03125$). In this example (and all other examples involving the L-shaped domain) we let $\Omega = (-1,1)^2 - [0,1] \times [-1,0]$. Here we let $\Omega_0 = (0.25, 0.75)^2$. The points of the graph which lie in the interior of the subdomain Ω_0 are between the dotted vertical lines. Note that the V_2-component of the error is practically zero in the interior of

Table 3.8a. Components of the energy-norm of the error in ω_0^h. L-shaped domain, $\alpha = \frac{2}{3}$, $p = 1$ ($2\alpha > p$). The V_1 and V_2 components of the error were determined from the solution u_h for $h = \frac{1}{64}$ using a least-squares fit over $\Omega_0 = (0.25, 0.75)\times(0.25, 0.75)$.

Components of the energy-norm of the error in ω_0^h					
Exact solution $u(r,\theta) = r^{\frac{2}{3}}\sin(\frac{2\theta}{3})$; linear elements					
Shrinking mesh-cell ω_0^h centered at (0.5, 0.5)					
h	$\|\|\|V_1\|\|\|^2_{\omega_0^h} \cdot 10^{-4}$	$\|\|\|V_2\|\|\|^2_{\omega_0^h} \cdot 10^{-4}$	$2(\int_{\omega_0^h} \nabla V_1 \cdot \nabla V_2) \cdot 10^{-4}$	$\theta = \cos^{-1}\left[\frac{\int_{\omega_0^h} \nabla V_1 \cdot \nabla V_2}{\|\|\|V_1\|\|\|_{\omega_0^h} \|\|\|V_2\|\|\|_{\omega_0^h}}\right]$	$\|\|\|e_h\|\|\|^2_{\omega_0^h} \cdot 10^{-4}$
0.125	2.490920	0.489113	0.310820	81.90	3.290850
0.0625	0.157319	0.016682	0.008554	85.21	0.182559
0.03125	0.009881	0.000562	0.000267	86.82	0.010755
0.015625	0.000624	0.000017	0.000010	87.29	0.000649

Table 3.8b. Pollution factors $\mu_{\omega_0^h}\%$ and $\xi_{\omega_0^h}\%$ and effectivity indices in the shrinking mesh-cell ω_0^h. L-shaped domain shown in Fig. 3.1a, $\alpha = \frac{2}{3}$ $p = 1$ $(2\alpha > p)$. Note that the pollution factors converges to zero and the effectivity indices $\kappa_{\omega_0^h}$ and $\kappa'_{\omega_0^h}$ converge to one, asymptotically.

Pollution factors and effectivity indices in ω_0^h						
Exact solution $u(r,\theta) = r^{\frac{2}{3}}\sin(\frac{2\theta}{3})$; linear elements						
Shrinking mesh-cell ω_0^h centered at (0.5, 0.5)						
h	$\mu_{\omega_0^h}\%$	$\xi_{\omega_0^h}\%$	$\kappa_{\omega_0^h} = \frac{\mathcal{E}_{\omega_0^h}}{\lvert\lvert\lvert e_h \rvert\rvert\rvert_{\omega_0^h}}$ Effectivity Index		$\kappa'_{\omega_0^h} = \frac{\mathcal{E}_{\omega_0^h}}{\lvert\lvert\lvert v_1 \rvert\rvert\rvert_{\omega_0^h}}$ Effectivity Index	
			$\kappa^{ZZ}_{\omega_0^h}$	$\kappa^{ER}_{\omega_0^h}$	$\kappa'^{ZZ}_{\omega_0^h}$	$\kappa'^{ER}_{\omega_0^h}$
0.125	40.51	44.31	0.888	0.889	1.04	1.04
0.0625	30.96	32.56	0.931	0.932	1.01	1.01
0.03125	23.19	23.84	0.959	0.959	1.00	1.00
0.015625	16.28	16.50	0.981	0.981	1.00	1.00

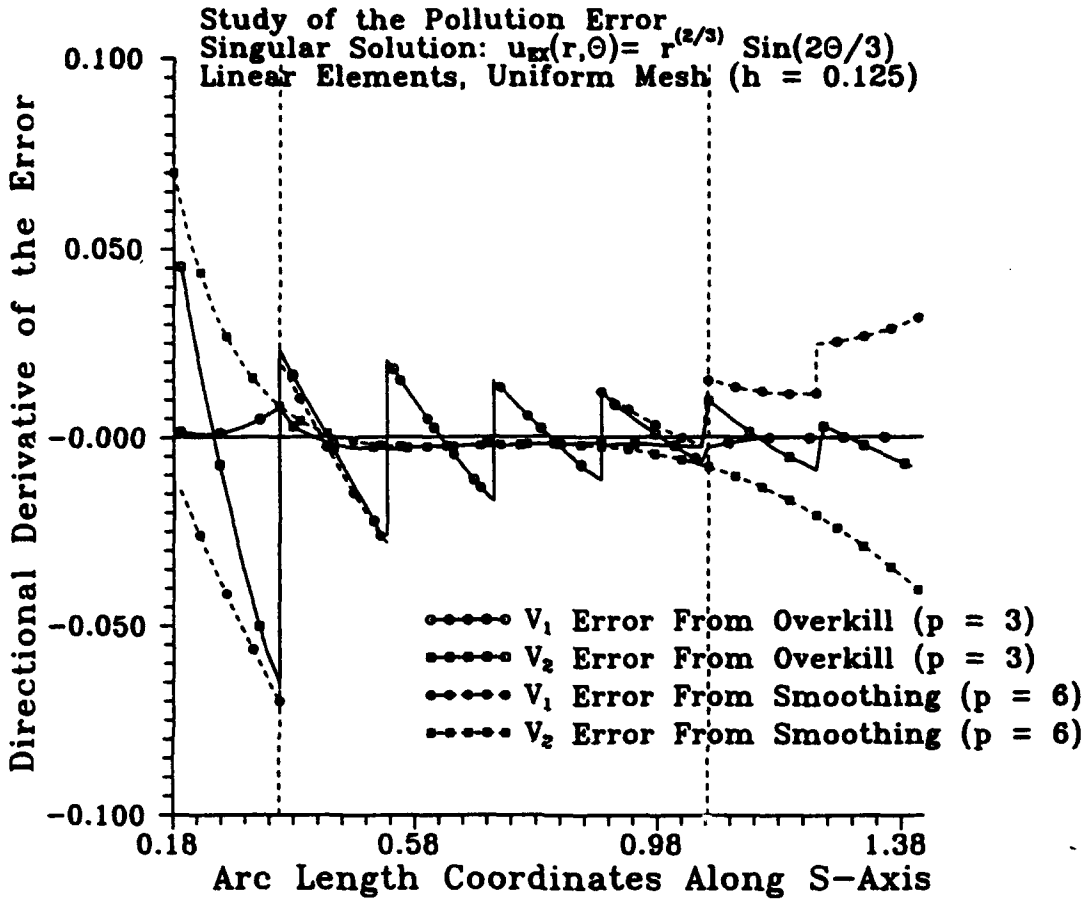

Figure 3.3. Pollution effect for uniform meshes. Linear elements ($p = 1$), $\alpha = \frac{2}{3}$, Uniform mesh size $h = \frac{1}{8}$. Directional derivatives of the V_1 - and V_2 - components of the error along the line A_1A_3 (shown in Fig. 3.1a). Note that $\left|\frac{\partial V_2}{\partial s}\right| \ll \left|\frac{\partial V_1}{\partial s}\right|$ in the interior of the subdomain.

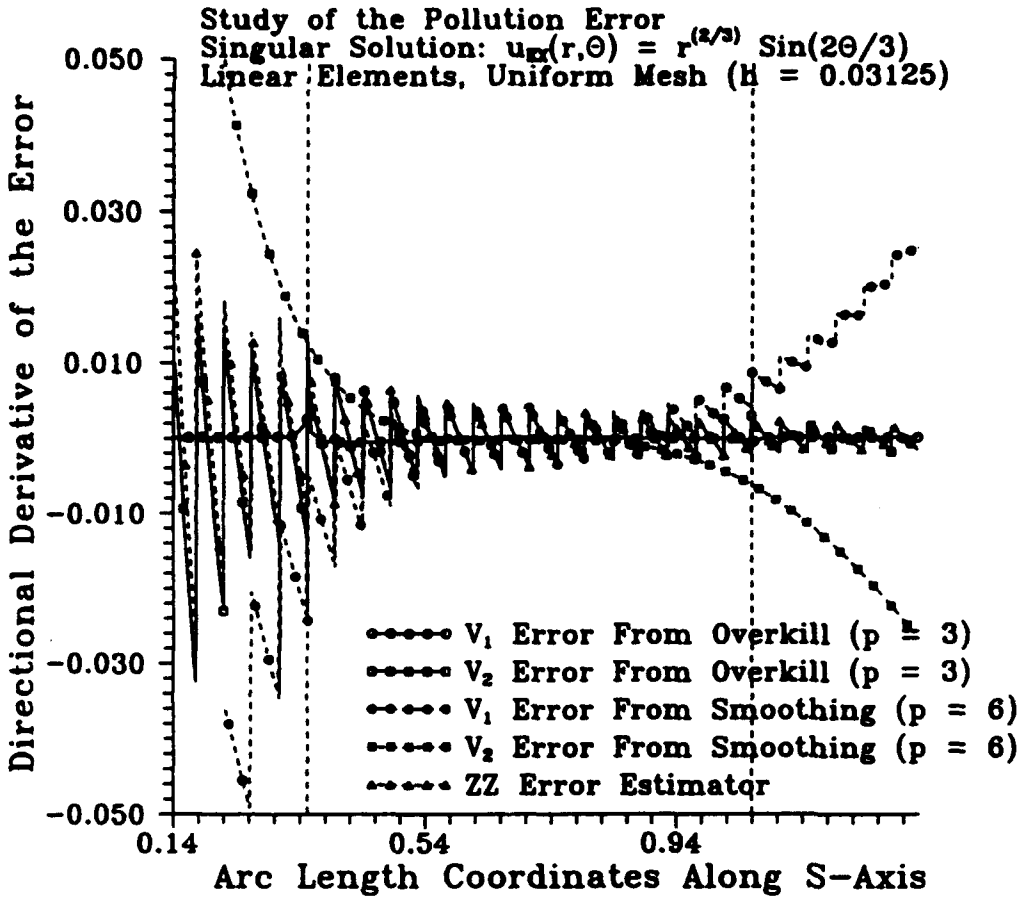

(a)

Figure 3.4. Pollution effect for uniform meshes. Linear elements ($p = 1$), $\alpha = \frac{2}{3}$, Uniform mesh size $h = \frac{1}{32}$. (a) Directional derivatives of the V_1- and V_2-components of the error and the *ZZ* estimators along the s-axis (shown in Fig. 3.1a). (The extent of the subdomain is indicated by the dotted vertical lines.) (b) Detail of the graph in Fig. 3.4a for the points lying in the subdomain. Note that $\left|\frac{\partial V_2}{\partial s}\right| \ll \left|\frac{\partial V_1}{\partial s}\right|$ and $(\sigma^{zz} - \nabla u_h) \cdot s \approx \frac{\partial V_1}{\partial s}$, asymptotically, in the interior of the subdomain.

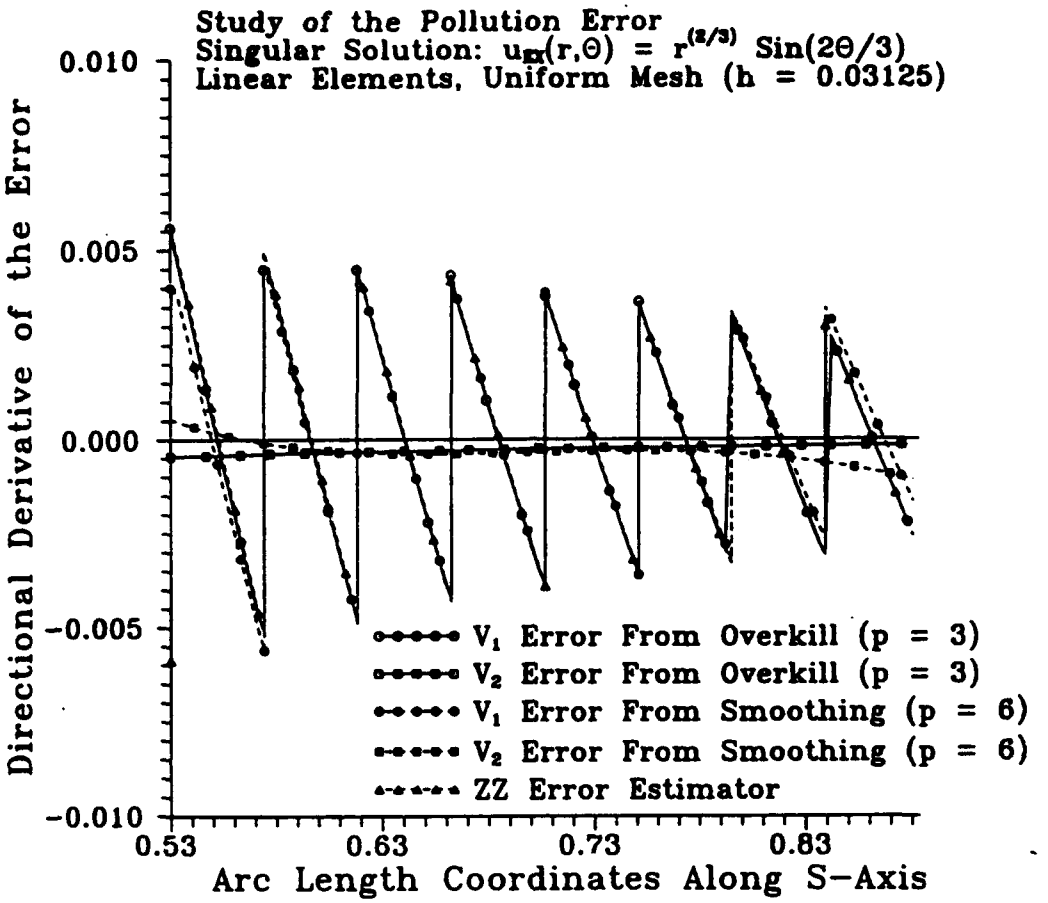

(b)

Figure 3.4. (continued)

the subdomain. In Fig. 3.4b we show the detail of the graph in Fig. 3.4a for the elements in the interior of the subdomain. Note that the error estimator coincides with the V_1-component of the error in the interior (one layer of elements away from the boundary) of the subdomain Ω_0.

In Tables 3.9a, 3.9b, we give the values of $|||V_1|||^2_{\omega_0^h}$, $|||V_2|||^2_{\omega_0^h}$ and $\int_{\omega_0^h} \nabla V_1 \cdot \nabla V_2$, the values of the pollution factors $\mu^{\%}_{\omega_0^h}$ and $\xi^{\%}_{\omega_0^h}$, and the effectivity indices $\kappa_{\omega_0^h}$ and $\kappa'_{\omega_0^h}$ for the two estimators for linear elements ($p = 1$) and $\alpha = \frac{1}{3}$ ($2\alpha < p$). Note that the pollution factor $\mu^{\%}_{\omega_0^h}$ converges to 100%, the pollution factor $\xi^{\%}_{\omega_0^h}$ diverges to infinity and the effectivity index $\kappa_{\omega_0^h}$ converges to zero; however the effectivity index $\kappa'_{\omega_0^h}$ converges to one as the mesh-size tends to zero. In Fig. 3.5 (resp. Fig. 3.6) we show the directional derivatives of the components of the error along that part of A_1A_3 which lies over the subdomain, for $h = 0.125$ (resp. h= 0.03125). Note that the V_2-component of the error converges to zero slower than the V_1-component as the mesh is refined. In Fig. 3.6b we show the detail of the graph in Fig. 3.6a for elements in the interior of the subdomain. Note that the error estimator coincides with the V_1-component of the error in the interior of the subdomain.

3.2.4.2. Uniform meshes of quadratic elements.

Similarly as in the example 3.1.2 we let Ω be the trapezoid shown in Fig. 3.1b with $A_1 = (0, 0)$, $A_2 = (1, 0)$, $A_3 = (1, 1)$, $A_4 = (-1, 1)$. For the definition of V_1 and V_2 and the shrinking mesh-cell ω_0^h we selected the subdomain $\Omega_0 = (0.375, 0.625)^2$. In Tables 3.10a, 3.10b we report the values of the components of the error, the pollution factors and the effectivity indices for quadratic elements ($p = 2$) and $\alpha = \frac{4}{3}$ ($2\alpha > p$). Note that the pollution factors $\mu^{\%}_{\omega_0^h}$ and $\xi^{\%}_{\omega_0^h}$ converge to zero and the effectivity indices $\kappa_{\omega_0^h}$ and $\kappa'_{\omega_0^h}$ for both estimators converge to one as the mesh-size tends to zero. In Tables 3.11a, 3.11b we give the values of $|||V_1|||^2_{\omega_0^h}$, $|||V_2|||^2_{\omega_0^h}$ and $\int_{\omega_0^h} \nabla V_1 \cdot \nabla V_2$, the values of the pollution factors $\mu^{\%}_{\omega_0^h}$ and $\xi^{\%}_{\omega_0^h}$, and the effectivity indices $\kappa_{\omega_0^h}$ and $\kappa'_{\omega_0^h}$ for quadratic elements and $\alpha = \frac{2}{3}$. Note that for $\alpha = \frac{2}{3}$ ($2\alpha < p$), the pollution factor $\mu^{\%}_{\omega_0^h}$ converges to 100%, the pollution factor $\xi^{\%}_{\omega_0^h}$ diverges to infinity, the effectivity index $\kappa_{\omega_0^h}$ converges to zero; however the effectivity index $\kappa'_{\omega_0^h}$ converges to one as the mesh-size tends to zero.

In Fig. 3.7a (resp. Fig. 3.7b) we show the directional derivatives of the V_1- and V_2- components of the error along that part of the s-axis which lies over the subdomain Ω_0 of the uniform mesh of quadratic elements for $\alpha = \frac{2}{3}$ and $h = 0.0625$ (resp. $h = 0.03125$) as shown in Fig. 3.1b. Note that the V_2-component of the error in the interior of the subdomain converges to zero slower than the V_1-component of

Table 3.9a. Components of the energy-norm of the error in ω_0^h. L-shaped domain shown in Fig. 3.1a, $\alpha = \frac{1}{3}$, $p = 1$ $(2\alpha < p)$. The V_1 and V_2 components of the error were determined from the solution u_h for $h = \frac{1}{32}$ using a least-squares fit over $\Omega_0 = (0.25, 0.75)\times(0.25, 0.75)$.

Components of the energy-norm of the error in ω_0^h					
Exact solution $u(r,\theta) = r^{\frac{1}{3}}\sin(\frac{\theta}{3})$; linear elements					
Shrinking mesh-cell ω_0^h centered at (0.5, 0.5)					
h	$\|\|\|V_1\|\|\|^2_{\omega_0^h}\cdot 10^{-4}$	$\|\|\|V_2\|\|\|^2_{\omega_0^h}\cdot 10^{-4}$	$2(\int_{\omega_0^h}\nabla V_1\cdot\nabla V_2)\cdot 10^{-4}$	$\theta = \cos^{-1}\left[\frac{\int_{\omega_0^h}\nabla V_1\cdot\nabla V_2}{\|\|\|V_1\|\|\|_{\omega_0^h}\|\|\|V_2\|\|\|_{\omega_0^h}}\right]$	$\|\|\|e_h\|\|\|^2_{\omega_0^h}\cdot 10^{-4}$
0.125	0.161378	2.685990	0.251750	78.97	3.091190
0.0625	0.012095	0.267938	0.013579	83.15	0.293936
0.03125	0.000857	0.027036	0.000902	84.62	0.028795

Table 3.9b. Pollution factors $\mu^{\%}_{\omega_0^h}$, $\xi^{\%}_{\omega_0^h}$ and effectivity indices $\kappa_{\omega_0^h}$, $\kappa'_{\omega_0^h}$ in the shrinking mesh-cell ω_0^h. L-shaped domain shown in Fig. 3.1a, $\alpha = \frac{1}{3}$, $p = 1$ $(2\alpha < p)$. Note that the pollution factor $\mu^{\%}_{\omega_0^h}$ converges to 100%, the pollution factor $\xi^{\%}_{\omega_0^h}$ diverges to infinity and effectivity index $\kappa_{\omega_0^h}$ converges to zero asymptotically. *However the effectivity index* $\kappa'_{\omega_0^h}$ converges to one.

Pollution factors and effectivity indices						
Exact solution $u(r,\theta) = r^{\frac{1}{3}}\sin(\frac{\theta}{3})$; linear elements						
Shrinking mesh-cell ω_0^h centered at (0.5, 0.5)						
h	$\mu_{\omega_0^h}\%$	$\xi_{\omega_0^h}\%$	$\kappa_{\omega_0^h} = \frac{\mathcal{E}_{\omega_0^h}}{\|\|e_h\|\|_{\omega_0^h}}$ Effectivity Index		$\kappa'_{\omega_0^h} = \frac{\mathcal{E}_{\omega_0^h}}{\|\|v_1\|\|_{\omega_0^h}}$ Effectivity Index	
			$\kappa^{ZZ}_{\omega_0^h}$	$\kappa^{ER}_{\omega_0^h}$	$\kappa'^{ZZ}_{\omega_0^h}$	$\kappa'^{ER}_{\omega_0^h}$
0.125	97.12	408.0	0.235	0.237	1.04	1.03
0.0625	97.81	470.7	0.203	0.204	1.01	1.01
0.03125	98.45	561.7	0.172	0.172	1.00	1.00

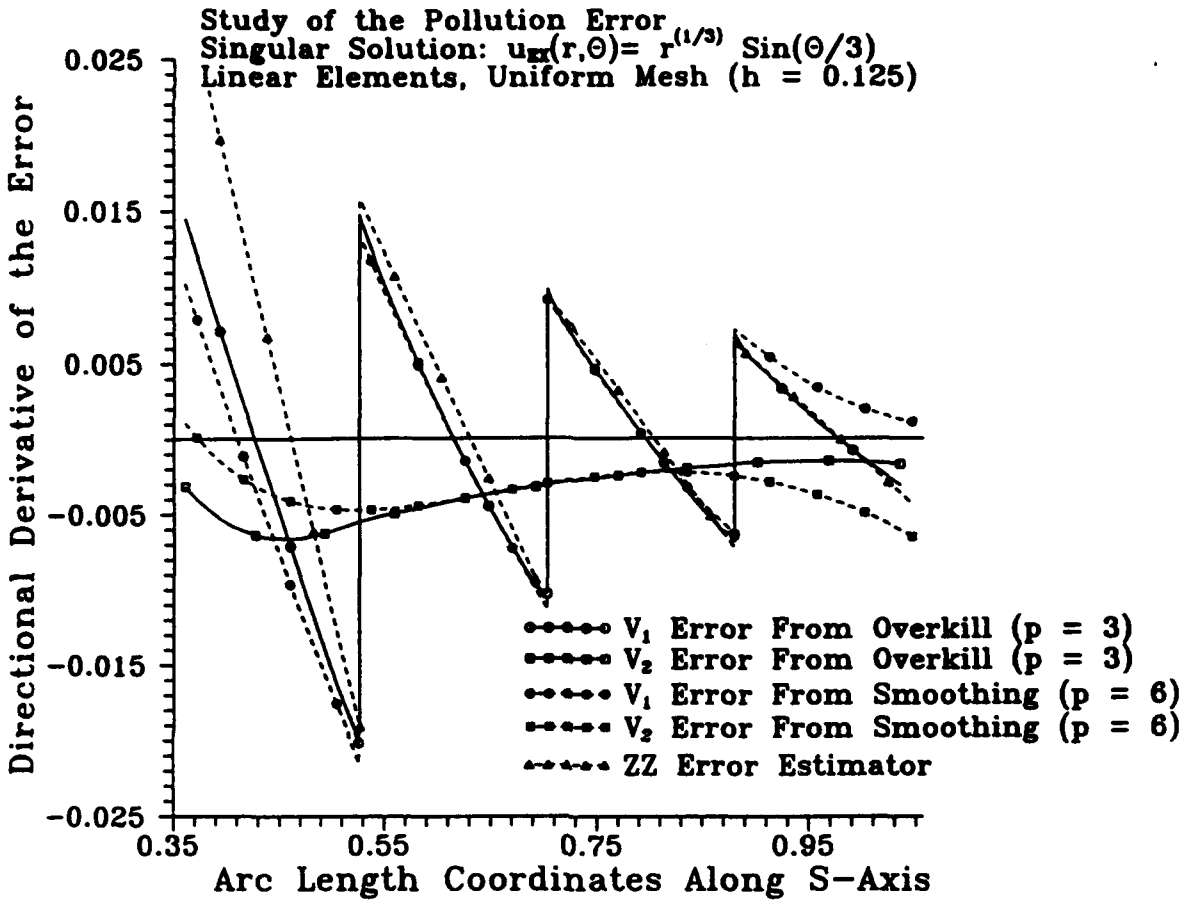

Figure 3.5. Pollution effect for uniform meshes. Linear elements ($p = 1$), $\alpha = \frac{1}{3}$, Uniform mesh size $h = \frac{1}{8}$. Directional derivatives of the V_1- and V_2-components of the error and the ZZ estimator in the subdomain along the s-axis shown in Fig. 3.1a. Note that $\left|\frac{\partial V_2}{\partial s}\right| \approx \left|\frac{\partial V_1}{\partial s}\right|$ and $(\sigma^{ZZ} - \nabla u_h) \cdot s \approx \frac{\partial V_1}{\partial s}$, asymptotically, in the interior of the subdomain.

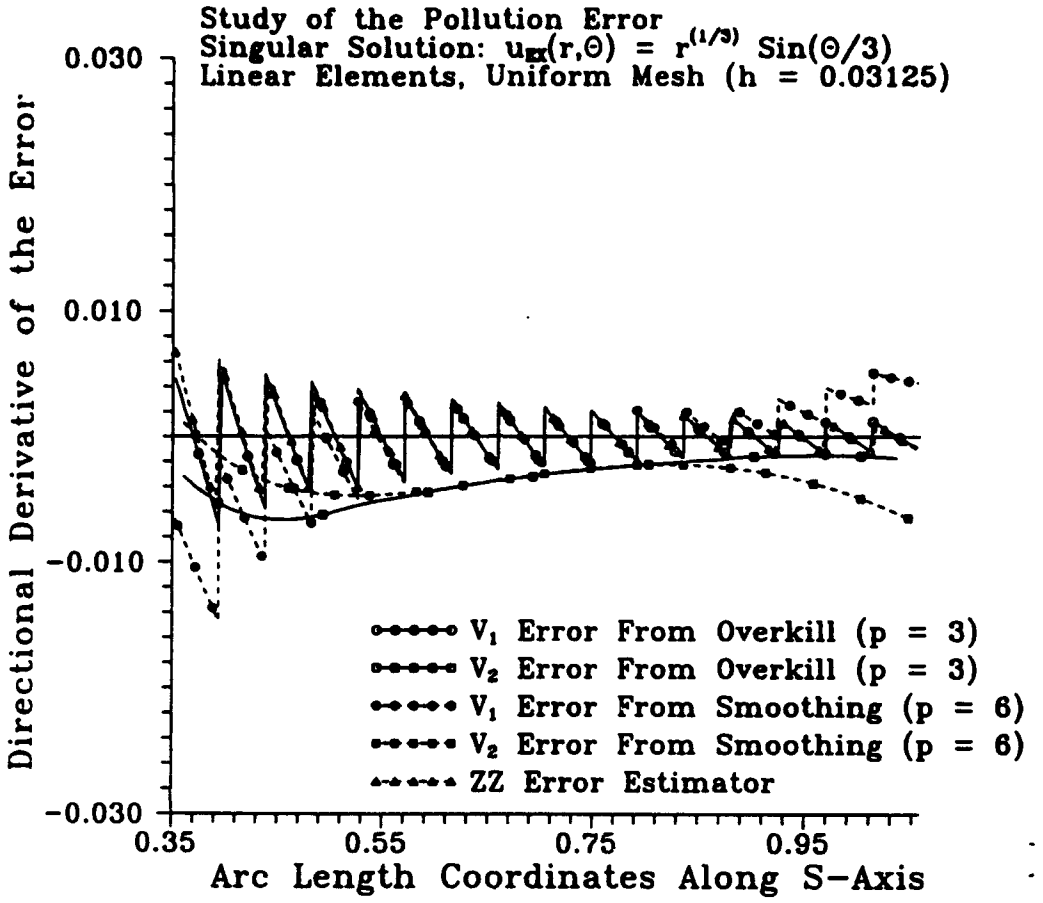

(a)

Figure 3.6. Pollution effect for uniform meshes. Linear elements ($p = 1$), $\alpha = \frac{1}{3}$, Uniform mesh-size $h = \frac{1}{32}$. (a) Directional derivatives of the V_1 - and V_2 - components and the ZZ estimator in the subdomain along the s-axis in Fig. 3.1a. (b) Detail of the graph in Fig. 3.6a for elements in the interior of the subdomain. Note that $\left|\frac{\partial V_2}{\partial s}\right| \gg \left|\frac{\partial V_1}{\partial s}\right|$ and $(\sigma^{ZZ} - \nabla u_h) \cdot s \approx \frac{\partial V_1}{\partial s}$, asymptotically, in the interior of the subdomain.

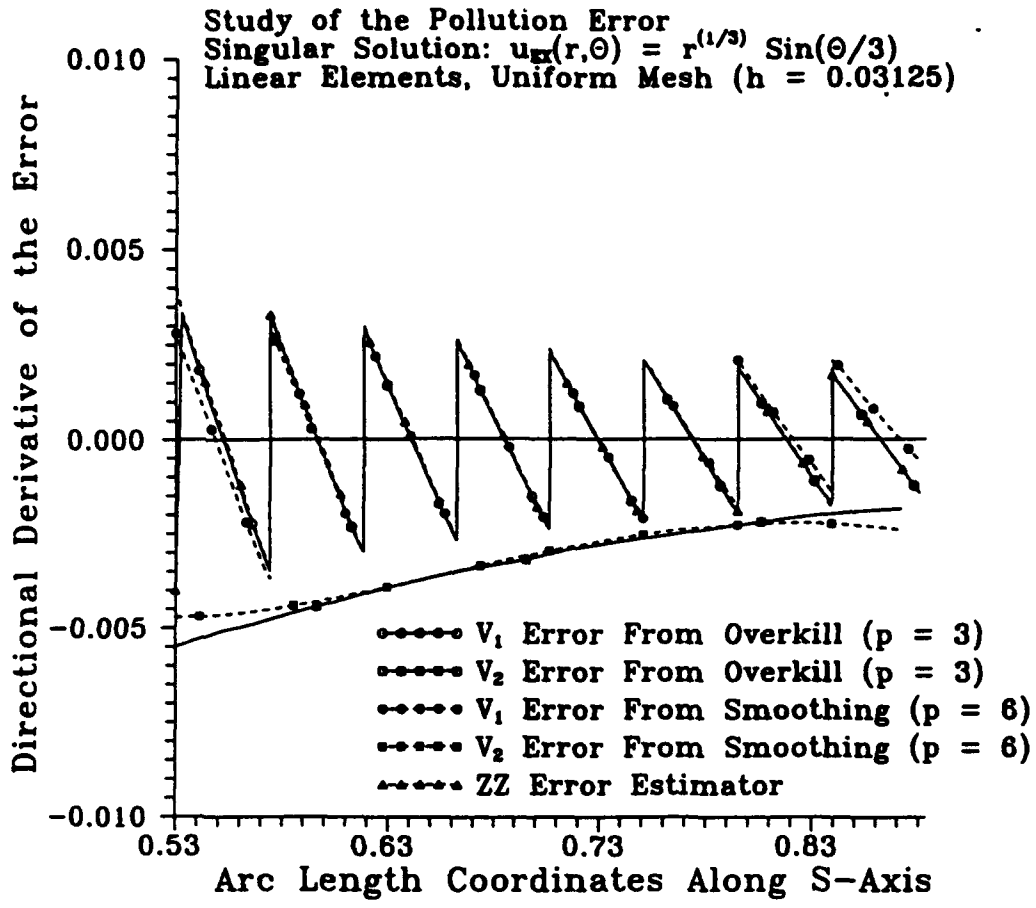

(b)

Figure 3.6. (continued)

Table 3.10a. Components of the energy-norm of the error in ω_0^h. Convex domain shown in Fig. 3.1b, $\alpha = \frac{4}{3}$, $p = 2$ $(2\alpha > p)$. The V_1 and V_2 components of the error were determined from the solution u_h for $h = \frac{1}{3}$ using a least-squares fit over $\Omega_0 = (0.25, 0.75) \times (0.25, 0.75)$.

Components of the energy-norm of the error					
Uniform mesh; shrinking mesh-cell centered at (0.5, 0.5)					
Exact solution $u(r,\theta) = r^{\frac{4}{3}} \sin(\frac{4\theta}{3})$; quadratic elements					
h	$\|\|\|V_1\|\|\|^2_{\omega_0^h} \cdot 10^{-8}$	$\|\|\|V_2\|\|\|^2_{\omega_0^h} \cdot 10^{-8}$	$2(\int_{\omega_0^h} \nabla V_1 \cdot \nabla V_2) \cdot 10^{-8}$	$\theta = \cos^{-1}\left[\frac{\int_{\omega_0^h} \nabla V_1 \cdot \nabla V_2}{\|\|\|V_1\|\|\|_{\omega_0^h} \|\|\|V_2\|\|\|_{\omega_0^h}}\right]$	$\|\|\|e_h\|\|\|^2_{\omega_0^h} \cdot 10^{-8}$
0.125	3.177500	0.009124	0.014658	92.46	3.171960
0.0625	0.047235	0.000266	0.000537	94.34	0.046964
0.03125	0.000741	0.000016	0.000033	98.54	0.000724

Table 3.10b. Pollution factors $\mu^{\%}_{\omega_0^h}$, $\xi^{\%}_{\omega_0^h}$ and effectivity indices $\kappa_{\omega_0^h}$, $\kappa'_{\omega_0^h}$ in the shrinking mesh-cell ω_0^h. Convex domain shown in Fig. 3.1b, $\alpha = \frac{4}{3}$, $p = 2$ $(2\alpha > p)$. Note that the pollution factors decreases and the effectivity indices $\kappa_{\omega_0^h}$ and $\kappa'_{\omega_0^h}$ converge to one asymptotically.

Pollution factors and effectivity indices						
Uniform mesh; Shrinking mesh-cell centered at (0.5, 0.5)						
Exact solution $u(r,\theta) = r^{\frac{1}{3}}\sin(\frac{4\theta}{3})$; quadratic elements						
Shrinking mesh-cell ω_0^h centered at (0.5, 0.5)						
h	$\mu_{\omega_0^h}\%$	$\xi_{\omega_0^h}\%$	$\kappa_{\omega_0^h} = \frac{\mathcal{E}_{\omega_0^h}}{\lvert\lvert\lvert e_h \rvert\rvert\rvert_{\omega_0^h}}$ Effectivity Index		$\kappa'_{\omega_0^h} = \frac{\mathcal{E}_{\omega_0^h}}{\lvert\lvert\lvert v_1 \rvert\rvert\rvert_{\omega_0^h}}$ Effectivity Index	
			$\kappa^{ZZ}_{\omega_0^h}$	$\kappa^{ER}_{\omega_0^h}$	$\kappa'^{ZZ}_{\omega_0^h}$	$\kappa'^{ER}_{\omega_0^h}$
0.125	5.35	5.36	1.014	0.999	1.013	0.998
0.0625	7.49	7.50	1.010	0.999	1.007	0.997
0.03125	14.61	14.69	1.009	1.00	0.988	0.997

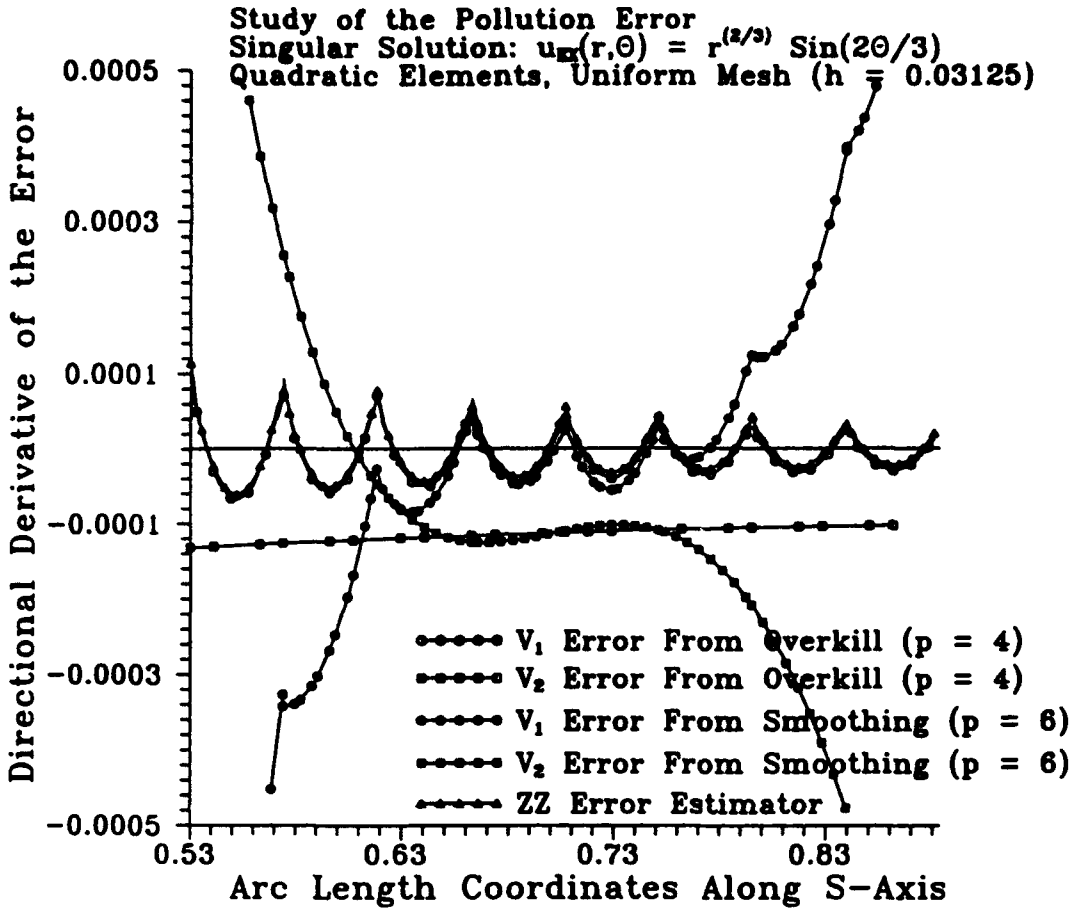

(a)

Figure 3.7. Pollution effect for uniform meshes. Quadratic elements $p = 2$, $\alpha = \frac{2}{3}$. (a) Uniform mesh-size $h = \frac{1}{32}$. (b) Uniform mesh-size $h = \frac{1}{64}$. Directional derivatives of the V_1 - and V_2 -components of the error and the ZZ error estimator in the subdomain along the s-axis shown in Fig. 3.1b. Note that $\left|\frac{\partial V_2}{\partial s}\right| \gg \left|\frac{\partial V_1}{\partial s}\right|$ and $(\sigma^{ZZ} - \nabla u_h) \cdot s \approx \frac{\partial V_1}{\partial s}$, asymptotically, in the interior of the subdomain.

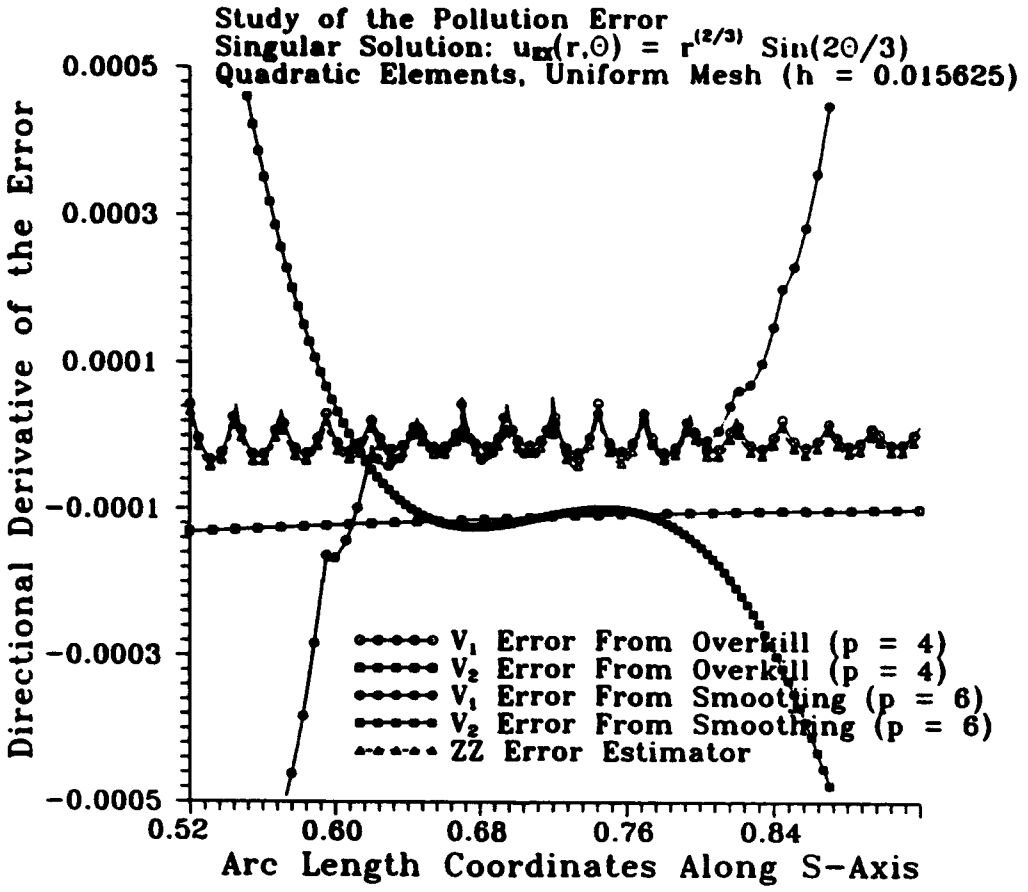

(b)

Figure 3.7. (continued)

Table 3.11a. Components of the energy norm of the error in ω_0^h. Convex domain shown in Fig. 3.1b, $\alpha = \frac{2}{3}$, $p = 2$ $(2\alpha < p)$. The V_1 and V_2 components of the error were determined from the solution u_h for $h = \frac{1}{3}$ using a least-squares fit over $\Omega_0 = (0.25, 0.75)\times(0.25, 0.75)$.

Components of the energy-norm of the error					
Uniform mesh; shrinking mesh-cell centered at (0.5, 0.5)					
Exact solution $u(r,\theta) = r^{\frac{2}{3}}\sin(\frac{2\theta}{3})$; quadratic elements					
h	$\|\|\|V_1\|\|\|^2_{\omega_0^h}\cdot 10^{-7}$	$\|\|\|V_2\|\|\|^2_{\omega_0^h}\cdot 10^{-7}$	$2(\int_{\omega_0^h}\nabla V_1\cdot\nabla V_2)\cdot 10^{-7}$	$\theta = \cos^{-1}\left[\frac{\int_{\omega_0^h}\nabla V_1\cdot\nabla V_2}{\|\|\|V_1\|\|\|_{\omega_0^h}\|\|\|V_2\|\|\|_{\omega_0^h}}\right]$	$\|\|\|e_h\|\|\|^2_{\omega_0^h}\cdot 10^{-7}$
0.125	0.513842	1.218180	0.0310429	88.87	1.763060
0.0625	0.007568	0.047364	0.000313	89.52	0.0552469
0.03125	0.000121	0.001844	0.000016	89.00	0.0019821

Table 3.11b. Pollution factors $\mu^{\%}_{\omega_0^h}$, $\xi^{\%}_{\omega_0^h}$ and effectivity indices $\kappa_{\omega_0^h}$, $\kappa'_{\omega_0^h}$ in the shrinking mesh-cell ω_0^h. Convex domain shown in Fig. 3.1b, $\alpha = \frac{2}{3}$, $p = 2$ $(2\alpha < p)$. Note that the pollution factor $\mu^{\%}_{\omega_0^h}$ converges to 100%, the pollution factor $\xi^{\%}_{\omega_0^h}$ diverges to infinity, and effectivity index $\kappa_{\omega_0^h}$ converges to zero asymptotically. *However the effectivity index* $\kappa'_{\omega_0^h}$ converges to one.

Pollution factors and effectivity indices						
Uniform mesh; Shrinking mesh-cell centered at (0.5, 0.5)						
Exact solution $u(r,\theta) = r^{\frac{2}{3}}\sin(\frac{2\theta}{3})$; quadratic elements						
Shrinking mesh-cell ω_0^h centered at (0.5, 0.5)						
h	$\mu_{\omega_0^h}\%$	$\xi_{\omega_0^h}\%$	$\kappa_{\omega_0^h} \approx \frac{\mathcal{E}_{\omega_0^h}}{\|\|e_h\|\|_{\omega_0^h}}$ Effectivity Index		$\kappa'_{\omega_0^h} = \frac{\mathcal{E}_{\omega_0^h}}{\|\|v_1\|\|_{\omega_0^h}}$ Effectivity Index	
			$\kappa^{ZZ}_{\omega_0^h}$	$\kappa^{ER}_{\omega_0^h}$	$\kappa'^{ZZ}_{\omega_0^h}$	$\kappa'^{ER}_{\omega_0^h}$
0.125	83.86	153.97	0.560	0.538	1.03	0.998
0.0625	92.85	250.16	0.376	0.367	1.01	0.993
0.03125	96.86	390.38	0.245	0.240	0.995	0.993

the error as the mesh is refined. Also, note that the error estimator closely follows the V_1 -component of the error in the interior of the subdomain Ω_0.

3.2.4.3. Uniform meshes of cubic elements.

Similarly as the example 3.1.3 we let Ω be the triangular domain of Fig. 3.1c with $A_1 = (0, 0)$, $A_2 = (0, 1)$, $A_3 = (\cos 75°, \sin 75°)$ and selected a subdomain Ω_0 as a parallelogram with vertices at (0.33, 0.24), (0.45, 0.24), (0.48, 0.36), (0.36, 0.36). In Fig. 3.8a (resp. Fig. 3.8b) we show the directional derivatives of the V_1 - and V_2 - components of the error along the s-axis, as shown in Fig. 3.1c. We considered a uniform mesh of cubic elements for $\alpha = \frac{6}{5}$ ($2\alpha < p$) and $h = 0.03125$ (resp. $h = 0.0078125$). Note that the V_2 -component of the error converges to zero slower than the V_1 -component as the mesh size tends to zero. Also note that the error estimator closely follows the V_1 -component of the error.

Remark 3.4. For uniform meshes both norm $|||V_1|||_{\omega_0^h}$ and $|||V_2|||_{\omega_0^h}$ converge to zero as the mesh-size tends to zero. When $2\alpha > p$ (resp. $2\alpha < p$) $|||V_2|||_{\omega_0^h}$ converges to zero at a faster (resp. slower) rate that $|||V_1|||_{\omega_0^h}$. When $\frac{|||V_2|||_{\omega_0^h}}{|||V_1|||_{\omega_0^h}} \longrightarrow$ 0 (resp. ∞) we have no pollution (resp. we have pollution), asymptotically.

Remark 3.5. The values of the V_1 - and V_2 -components of the error obtained using the overkill are more accurate than the values obtained by employing the least-squares fit over the subdomain. Nevertheless, for mesh-cells near the center of the subdomain the values of the V_1 - and V_2 -functions computed by both methodologies are practically the same.

3.3 Summary of the results for the pollution-effect in uniform meshes

In summary we observe that the results agree with the predictions of the asymptotic analysis, namely:

(i). For $2\alpha > p$, the pollution factors in the shrinking mesh-cell converge to zero and the effectivity indices $\kappa_{\omega_0^h}$, $\kappa'_{\omega_0^h}$ for both estimators converge to one as the mesh-size tends to zero.

(ii). For $2\alpha < p$, the percentage of pollution $\mu^{\%}_{\omega_0^h}$ in the shrinking mesh-cell converges to 100%, the pollution-factor $\xi^{\%}_{\omega_0^h}$ diverges to infinity and the effectivity index $\kappa_{\omega_0^h}$ for both estimators converges to zero. On the other hand the effectivity index $\kappa'_{\omega_0^h}$ converges to one.

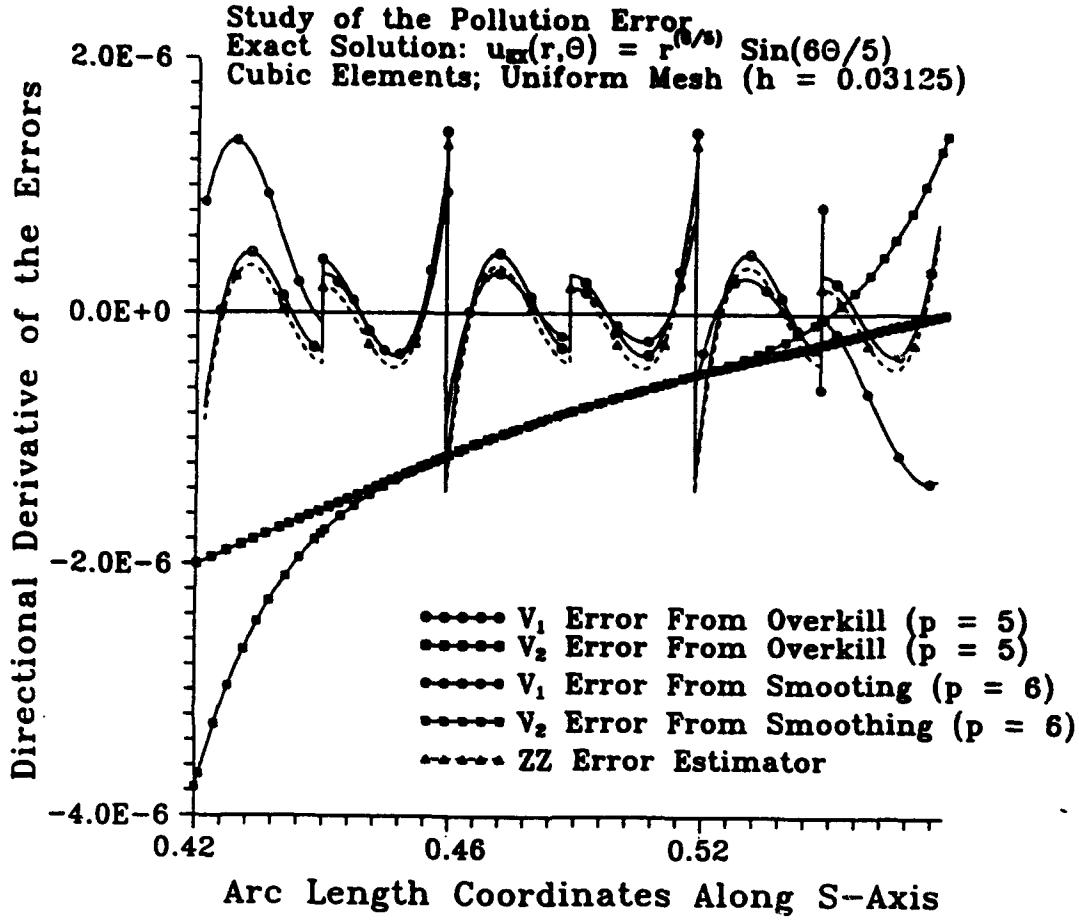

(a)

Figure 3.8. Pollution effect for uniform meshes: Cubic element ($p = 3$), $\alpha = \frac{6}{5}$. Directional derivatives of the V_1- and V_2-components of the error along the s-axis shown in Fig. 3.1c. (a) Uniform mesh size $h = \frac{1}{32}$ (b) Uniform mesh size $h = \frac{1}{64}$. Note that $\left|\frac{\partial V_2}{\partial s}\right| \gg \left|\frac{\partial V_1}{\partial s}\right|$ and $(\sigma^{ZZ} - \nabla u_h) \cdot s \approx \frac{\partial V_1}{\partial s}$, asymptotically, in the interior of the subdomain.

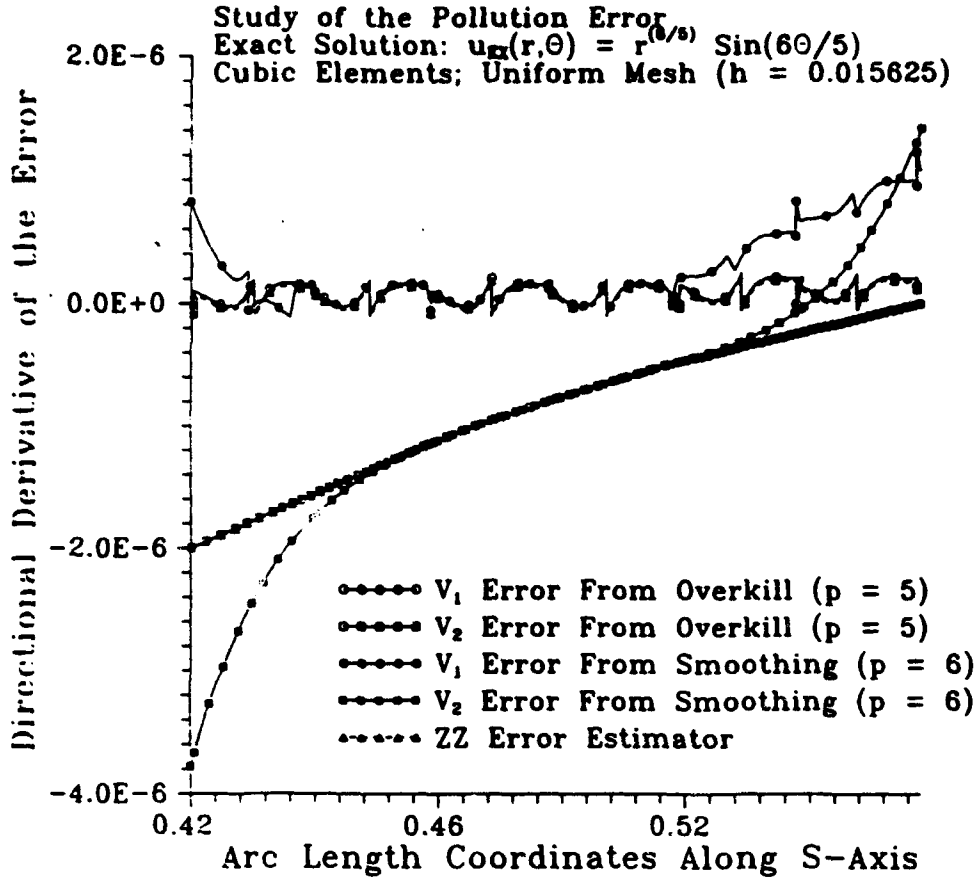

(b)

Figure 3.8. (continued)

(iii). The pollution-effect in uniform meshes becomes more severe as the degree of the elements is increased. This can be clearly seen by comparing the graphs in Figs. 3.8b, 3.9b, 3.10b, where the difference between the derivatives of the V_1 - and V_2 -components of the error in the interior of the subdomain Ω_0 increases with the polynomial degree of the elements.

4 Control of the pollution-effect using adaptive grids

In this Section we will give numerical examples which demonstrate that when the mesh is globally adaptive (i.e. nearly equilibrated in the energy-norm), the pollution is controlled.

4.1 The h-adaptive scheme

Here we summarize the h-adaptive scheme (see also [67], [68]) which was employed to construct the adaptive meshes in the numerical examples below.

Given a tolerance δ for the relative error in the global energy-norm,

1. Choose an initial discretization of the domain T_h^0 ; let $T_h = T_h^0$.

2. For the mesh T_h, compute the corresponding finite element solution u_h and obtain an estimate η_τ of the energy-norm of the error in element τ,

3. Check for convergence. If

$$\sqrt{\sum_{e=1}^{N} \eta_\tau^2} \leq \delta |||u_h|||_\Omega \tag{4.1}$$

stop; otherwise proceed to the next step. Here N denotes the number of elements in the mesh T_h.

4. Compute the target error e_{target} for the optimal mesh (using the *principle of equidistribution of error*) namely

$$e_{target} = \frac{\delta |||u_h|||_\Omega}{\sqrt{N}} \tag{4.2}$$

5. For each element τ, predict the optimal local mesh-size from the formula

$$h_\tau^{\text{opt}} = \frac{h}{\left(\frac{\eta_\tau}{e_{target}}\right)^{\frac{1}{r}}} \tag{4.3}$$

Here h_τ^{opt} is the predicted optimal mesh-size for the subdomain within the element τ, r is an exponent which depends on the order p of the approximation and the regularity of the solution.

6. Construct a smooth representation of the predicted optimal mesh-size over the mesh T_h which now becomes the *background grid* (see [67]) and use it to define the mesh-size function $h : \Omega \longrightarrow \mathrm{R}^+$.

7. Use either h-refinement or h-remeshing to construct a new grid T_h^{new} with minimal number of elements N, such that $h_\tau \leq h(x)$, $x \in \tau$, $\forall\, \tau \in T_h^{\text{new}}$.

4.2 Assessment of the pollution-effect for adaptive grids

We considered the mixed boundary value problem for the Laplace equation and applied boundary conditions consistent with the exact solution $u(r,\theta) = r^{\frac{1}{4}} \sin(\frac{1}{4}\theta)$ over the *square-slit domain* $\Omega = (-1,1)^2 - [0,1] \times \{0\}$ shown with thick black perigram in Fig. 4.1a. (Note that in this case $\alpha = \frac{1}{4}$ and the singularity is very strong.) We constructed nearly equilibrated meshes of linear, quadratic and cubic elements using adaptive refinement and remeshing and we studied the effect of the pollution for interior mesh-cells.

4.2.1 Nearly equilibrated grids of linear elements

In Fig. 4.1a and Fig. 4.1c we show the adaptive grids of linear elements ($p = 1$) generated using refinement and remeshing, respectively (a tolerance of 0.5% for the global relative error in the energy-norm was employed). In Fig. 4.2 (resp. Fig. 4.3) we show the graph of the values of the energy-norms of the error in the elements for the mesh shown in Fig. 4.1a (resp. 4.1c) (The elements have been numbered according to their distance from the singular point and two rings of elements around the singularity have been excluded from the graph). The values of the effectivity index for the mesh-cells (which are shown shaded gray in the Figures) are reported in Table 4.1 for the mesh shown in Fig. 4.1a and Table 4.2 shown in Fig. 4.1c. These values are compared with the *pollution-free* values of the effectivity index, $\bar{\kappa}$, for the mesh-cells. The pollution-free value of the effectivity index in each mesh-cell was obtained from a *pollution-free finite element solution* of the boundary value problem in the domain Ω, using the same mesh, with data obtained from the $(p+1)$ degree Taylor series expansion of the exact solution about the center X of each mesh-cell. Note that the computed values of the effectivity index are very close to the corresponding pollution-free values in all the interior mesh-cells.

For the mesh shown in Fig. 4.1c we also computed the effectivity index for the *mesh-layers*, which are shown in Figs. 4.4a, 4.4b. We excluded the last mesh-layer of elements adjacent to the singular point and numbered the layers inward from the boundary as shown in Fig. 4.4b. In Table 4.3 we give the computed effectivity indices and pollution-free value of the effectivity index for each mesh-layer. The

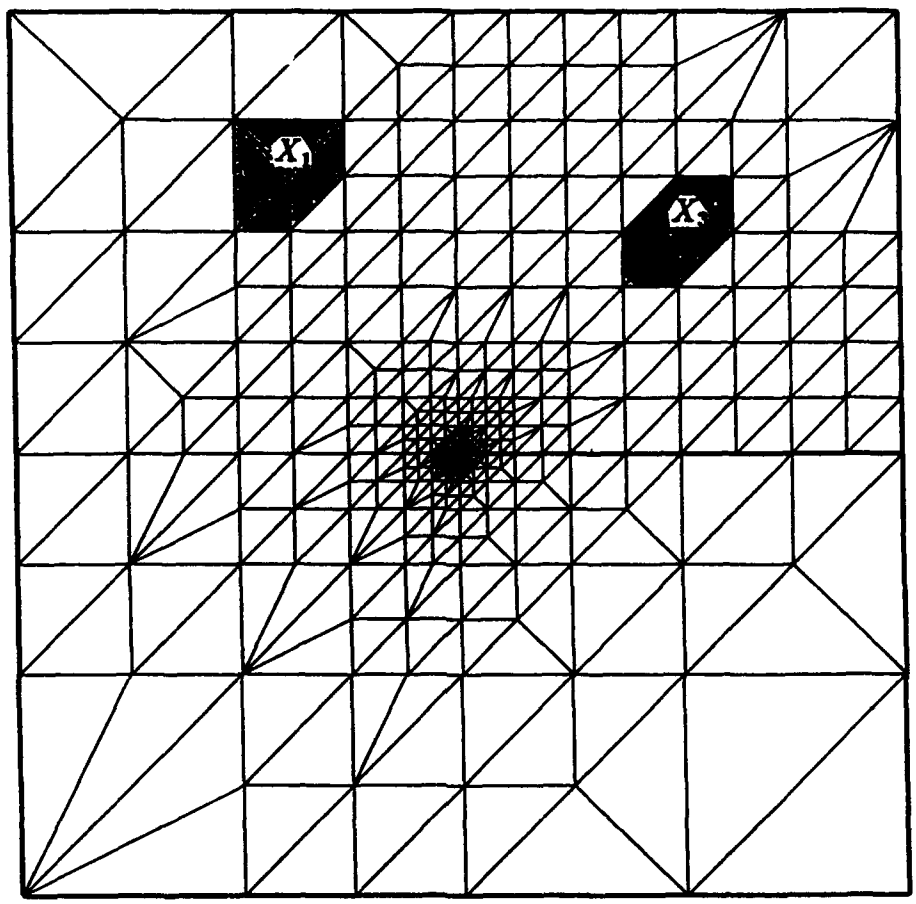

(a)

Figure 4.1. (a) A finite-element grid of linear elements constructed over the slit-domain using adaptive refinement and a tolerance of 0.5% for the global relative error in the energy-norm; (b) Detail of the finite-element mesh shown in Fig. 4.1a near the singular point with the mesh-cell $\omega^h_{X_2}$ shown shaded gray; (c) A finite-element grid of linear elements constructed over the slit-domain using adaptive remeshing and a tolerance of 0.5% for the global relative error in the energy-norm.

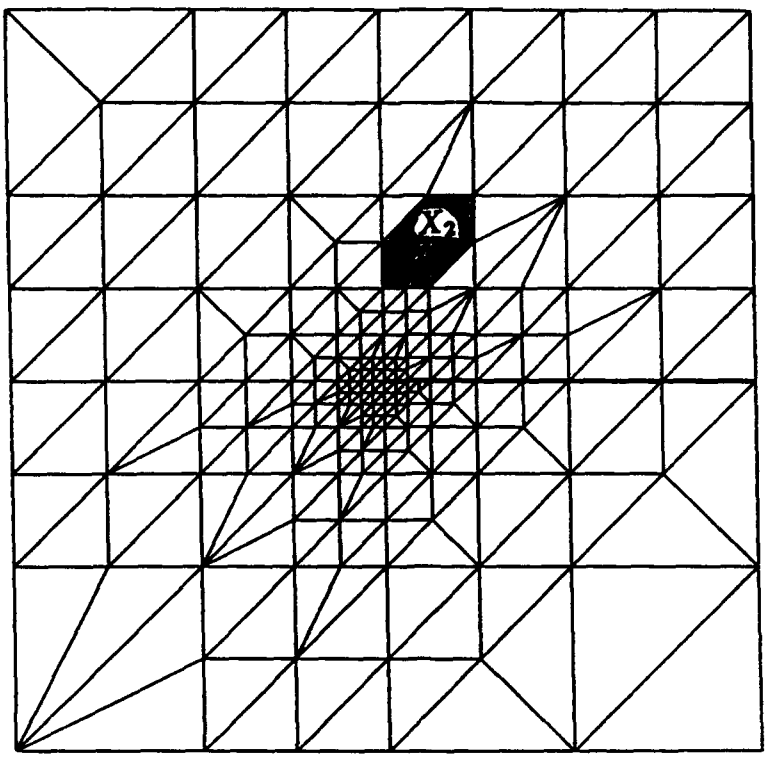

(b)

Figure 4.1. (continued)

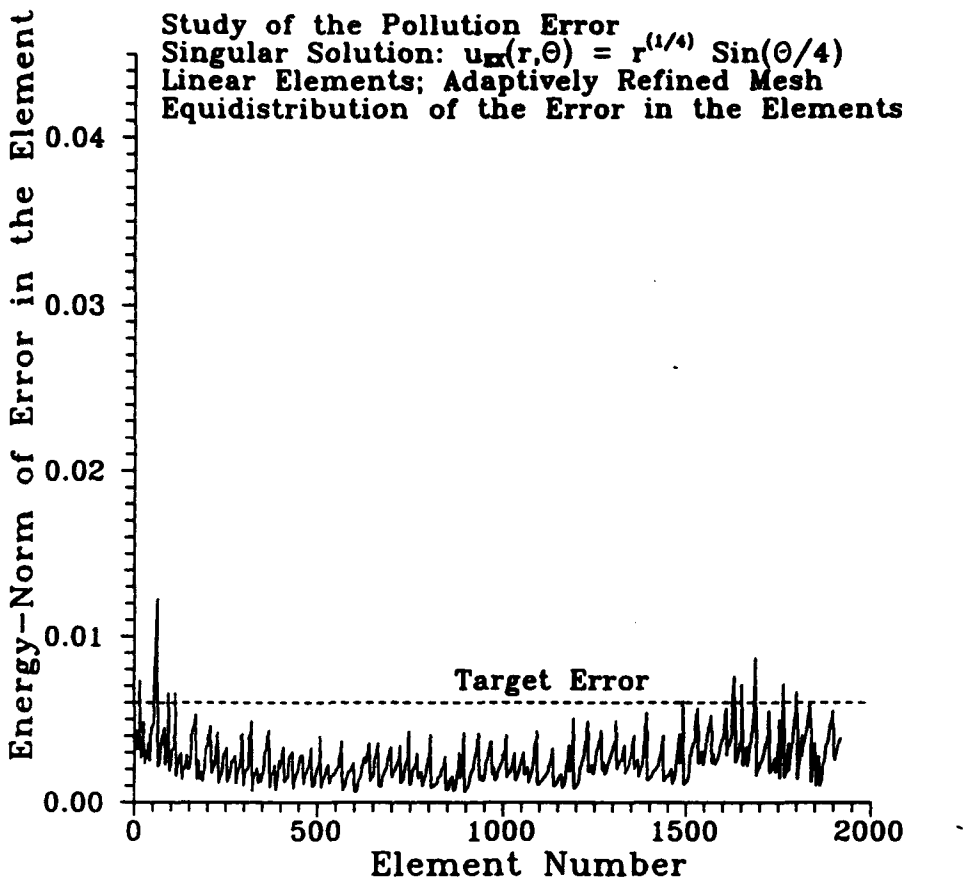

Figure 4.2. Control of the pollution-effect using adaptive grids. Distribution of the energy-norm of the error in the elements of the mesh shown in Fig. 4.1a.

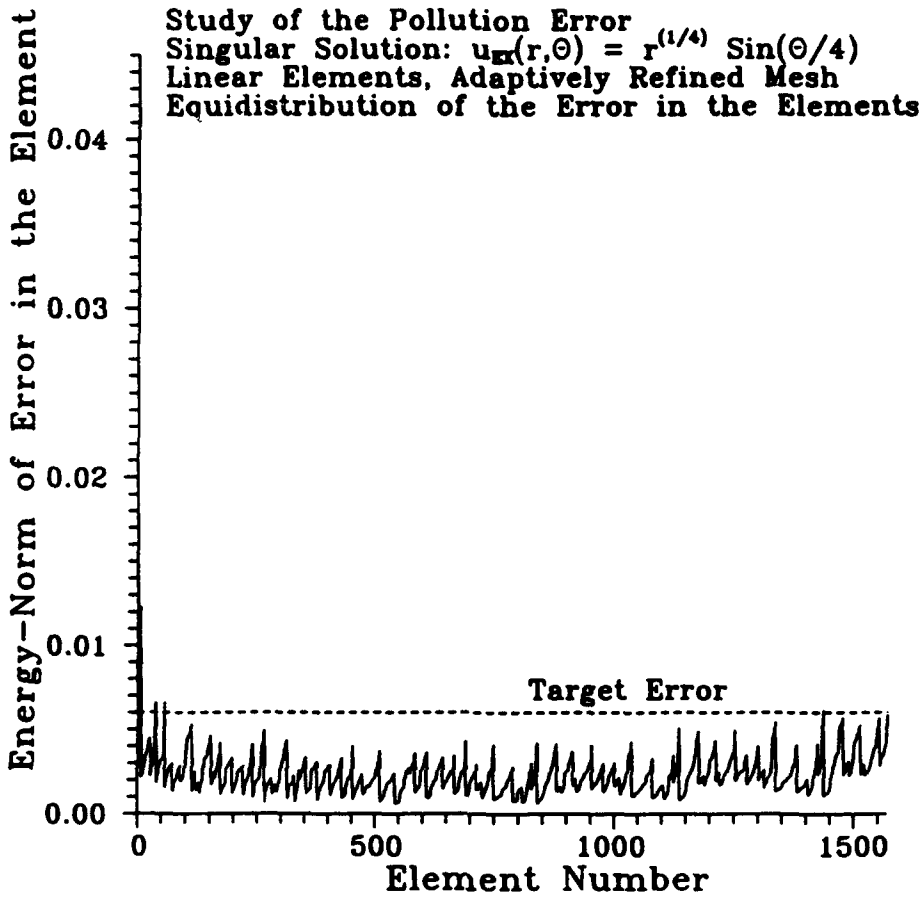

Figure 4.3. Control of the pollution-effect using adaptive grids. Distribution of the energy-norm of the error in the elements of the mesh shown in Fig. 4.1c.

Table 4.1. Control of the pollution-effect using adaptive grids. Adaptive grid of linear elements generated over the slit-domain using refinement (tolerance = 0.5%, H^1-error control). Comparison of the effectivity index, $\kappa_{\omega_X^h}$, in the H^1-norm, computed with respect to the exact solution with the corresponding values of the pollution-free effectivity index $\bar{\kappa}_{\omega_X^h}$, for the ZZ estimator and the element-residual (ER) estimator in the mesh-cells $\omega_{X_1}^h$, $\omega_{X_2}^h$ and $\omega_{X_3}^h$ (which consist of the elements connected to the nodes X_1, X_2 and X_3 shown in Fig. 4.1a).

Adaptive grid using refinement, H^1-error control, linear elements											
Effectivity index in the H^1-norm											
Mesh-cell $\omega_{X_1}^h$				Mesh-cell $\omega_{X_2}^h$				Mesh-cell $\omega_{X_3}^h$			
$\kappa^{ZZ}_{\omega^h_{X_1}}$	$\bar{\kappa}^{ZZ}_{\omega^h_{X_1}}$	$\kappa^{ER}_{\omega^h_{X_1}}$	$\bar{\kappa}^{ER}_{\omega^h_{X_1}}$	$\kappa^{ZZ}_{\omega^h_{X_2}}$	$\bar{\kappa}^{ZZ}_{\omega^h_{X_2}}$	$\kappa^{ER}_{\omega^h_{X_2}}$	$\bar{\kappa}^{ER}_{\omega^h_{X_2}}$	$\kappa^{ZZ}_{\omega^h_{X_3}}$	$\bar{\kappa}^{ZZ}_{\omega^h_{X_3}}$	$\kappa^{ER}_{\omega^h_{X_3}}$	$\bar{\kappa}^{ER}_{\omega^h_{X_3}}$
0.98	0.99	0.98	0.98	0.98	0.99	0.96	0.98	1.00	1.00	0.99	0.99

Table 4.2. Control of the pollution-effect using adaptive grids. Adaptive grid of linear elements generated over the slit-domain using remeshing (tolerance = 0.5%, H^1-error norm equidistribution). Comparison of the effectivity index $\kappa_{\omega_X^h}$ in the H^1-norm, computed with respect to the exact solution with the corresponding value of the pollution-free effectivity index $\bar{\kappa}_{\omega_X^h}$, for the ZZ estimator and the element-residual (ER) estimator in the mesh-cells $\omega_{X_1}^h$, $\omega_{X_2}^h$ and $\omega_{X_3}^h$ (which consist of the elements connected to the nodes X_1, X_2 and X_3 shown in Fig. 4.1c).

Adaptive grid using remeshing, H^1-error control, linear elements											
Effectivity index in the H^1-norm											
Mesh-cell $\omega_{X_1}^h$				Mesh-cell $\omega_{X_2}^h$				Mesh-cell $\omega_{X_3}^h$			
$\kappa_{\omega_{X_1}^h}^{ZZ}$	$\bar{\kappa}_{\omega_{X_1}^h}^{ZZ}$	$\kappa_{\omega_{X_1}^h}^{ER}$	$\bar{\kappa}_{\omega_{X_1}^h}^{ER}$	$\kappa_{\omega_{X_2}^h}^{ZZ}$	$\bar{\kappa}_{\omega_{X_2}^h}^{ZZ}$	$\kappa_{\omega_{X_2}^h}^{ER}$	$\bar{\kappa}_{\omega_{X_2}^h}^{ER}$	$\kappa_{\omega_{X_3}^h}^{ZZ}$	$\bar{\kappa}_{\omega_{X_3}^h}^{ZZ}$	$\kappa_{\omega_{X_3}^h}^{ER}$	$\bar{\kappa}_{\omega_{X_3}^h}^{ER}$
0.95	0.95	0.93	0.94	0.92	0.94	0.91	0.93	0.94	0.96	0.93	0.95

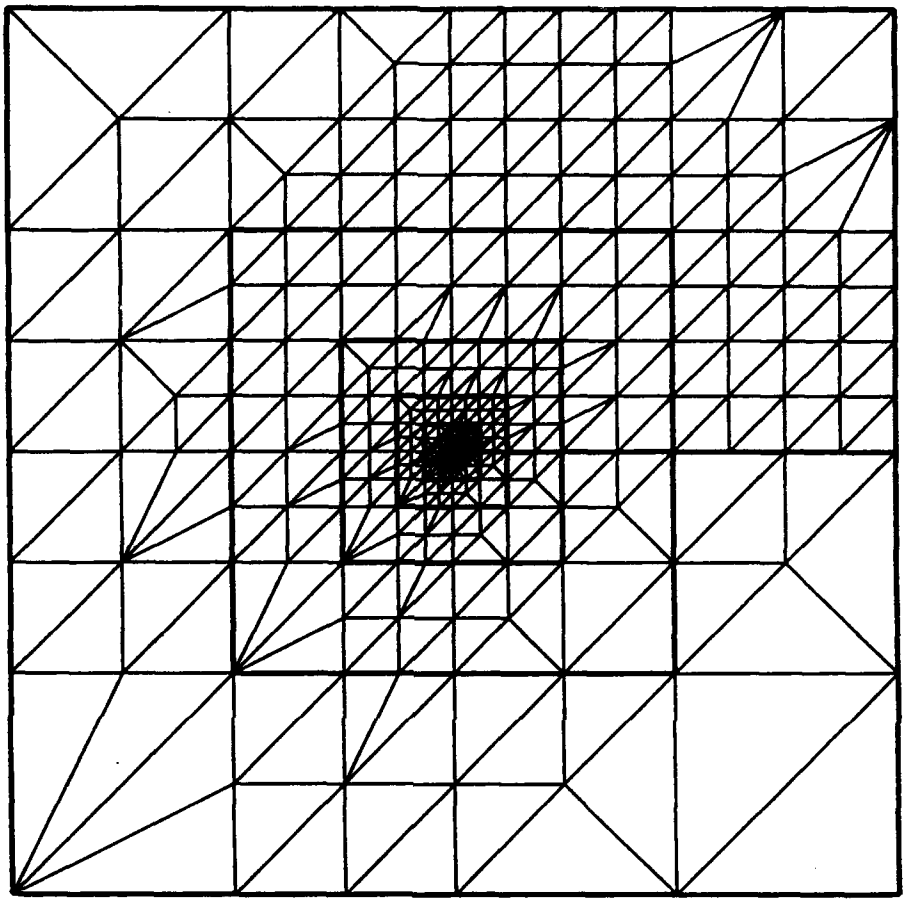

(a)

Figure 4.4. (a) The adaptive finite element mesh in Fig. 4.1a in which we indicate the mesh-layers for which we computed the effectivity index; (b) Detail of the finite-element mesh showing the mesh layer near the singular point; (c) Detail of the mesh near the singular point. This is the same mesh, shown in Fig. 4.4a and 4.4b, with two rings of elements around the singular point removed. This mesh was used in the computation of a pollution-free finite element solution.

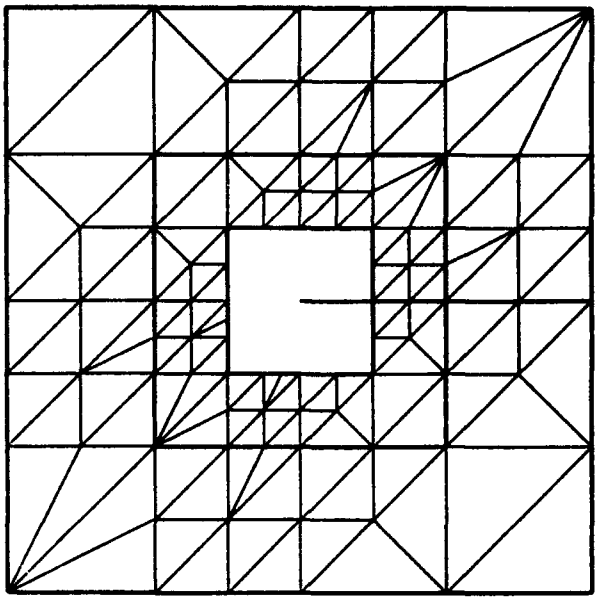

(b)

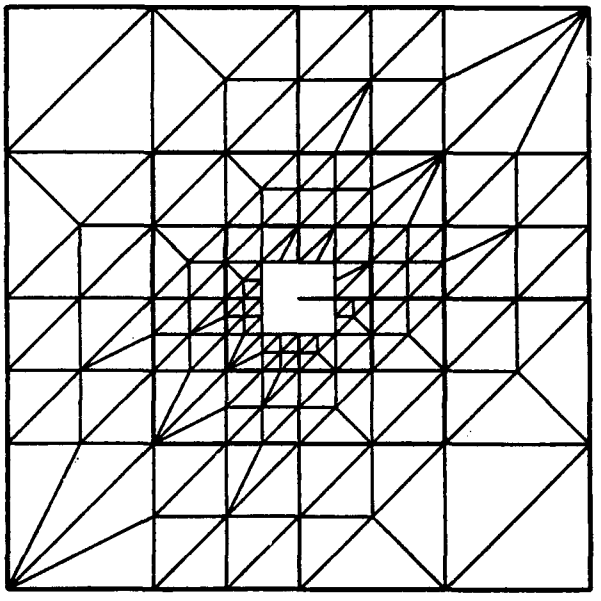

(c)

Figure 4.4 (continued)

Table 4.3. Control of the pollution-effect using adaptive grids. Adaptive grid of linear elements shown in Fig. 4.4. Effectivity index for element-residual and *ZZ* estimators for each mesh-layer ω_n in the interior of the mesh. Note that the effectivity index κ_{ω_n} computed with respect to the exact solution is very close to the pollution-free values $\bar{\kappa}_{\omega_n}$ for all the layers in the interior of the mesh.

Adaptive grid using refinement, H^1-error control, linear elements				
Effectivity index in each mesh layer				
Layer number	**Effectivity Index**			
	$\kappa_{\omega_n}^{ZZ}$	$\bar{\kappa}_{\omega_n}^{ZZ}$	$\kappa_{\omega_n}^{ER}$	$\bar{\kappa}_{\omega_n}^{ER}$
1	0.954	0.994	0.974	0.996
2	0.996	0.998	0.992	0.997
3	0.992	0.992	0.979	0.992
4	0.974	0.975	0.971	0.974
5	0.971	0.971	0.968	0.971
6	0.861	0.970	0.858	0.970

pollution-free values for the mesh-layers were obtained by solving the boundary value problem over the domain Ω_ϵ which excludes two rings of elements around the singular point as shown in Fig. 4.4c. Note that the values of the effectivity index for the mesh-layers ω_n are very close to the corresponding pollution-free values of the effectivity index.

4.2.2 Nearly equilibrated grids of quadratic elements

In Fig. 4.5 we show a grid of quadratic elements ($p = 2$) which was generated using adaptive refinement and equidistribution of the energy-norm of the error for a tolerance of 0.1%. In Fig. 4.6 we show the energy-norm of the error in the elements for the mesh shown in Fig. 4.5. (The elements have been numbered according to their distance from the singular point and two rings of elements around the singularity have been excluded from the graph.) In Table 4.4 (resp. Table 4.5) we compare the effectivity index of the estimators in the shaded mesh-cells (resp. mesh-layers) with the pollution-free values of the effectivity index in the mesh-cells (resp. mesh-layers). Note that the values of the effectivity index for the mesh-cells and the mesh-layers are very close to the corresponding pollution-free values of the effectivity index.

4.2.3 Nearly equilibrated grids of cubic elements

In Fig. 4.7a we give a grid of cubic elements ($p = 3$) which was constructed using adaptive refinement and equidistribution of the energy-norm of the error for a tolerance of 0.05%. In Fig. 4.8 we show the energy-norm of the error in the elements for the mesh shown in Fig. 4.7. (The elements have been numbered according to their distance from the singularity and the first two rings of elements around the singular point have been excluded from the graph.) In Table 4.6 (resp. Table 4.7) we compare the effectivity index of the estimators in the shaded mesh-cells (resp. mesh-layers) with the pollution-free values. Note that the values of the effectivity index for the mesh-cells and the mesh-layers are very close to the corresponding pollution-free values of the effectivity index.

4.3 Summary of the results for the pollution-effect in adaptive grids

In summary, we observe that when the mesh is nearly equilibrated in the energy-norm, the pollution in the energy-norm is negligible and the values of the effectivity index are, for all practical purposes, the same as the pollution-free values for any estimator.

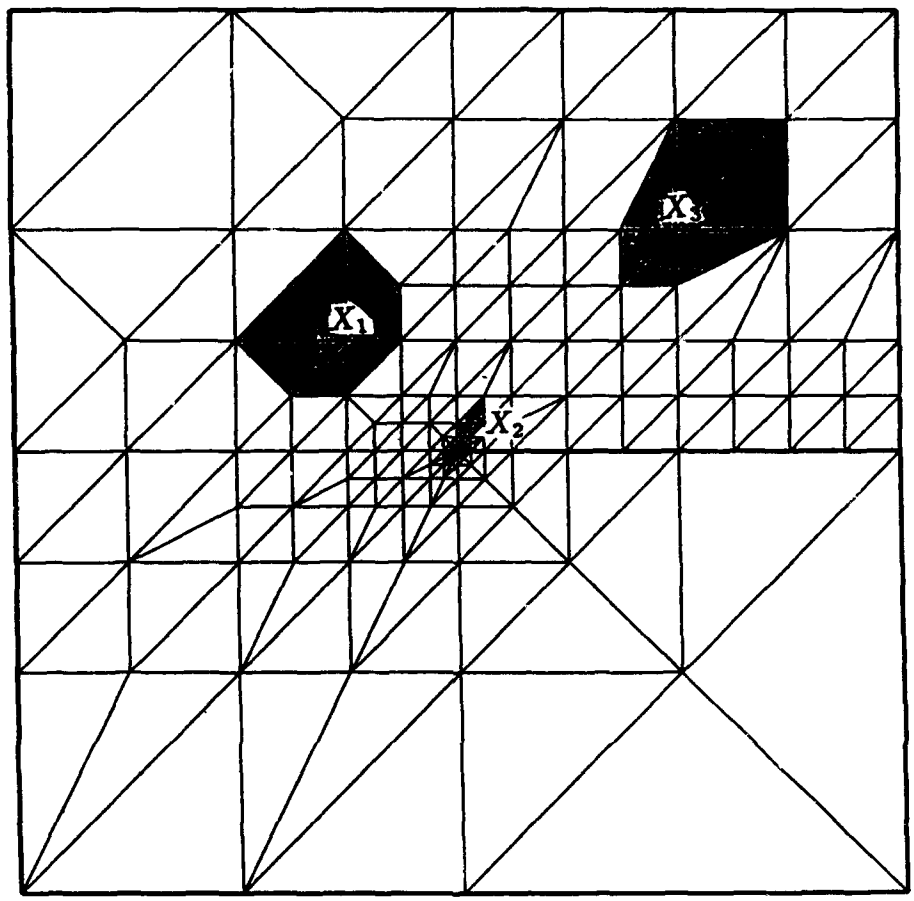

Figure 4.5. A finite-element grid of quadratic elements constructed over the slit-domain using adaptive refinement and a tolerance of 0.1% for the global relative error in the energy-norm.

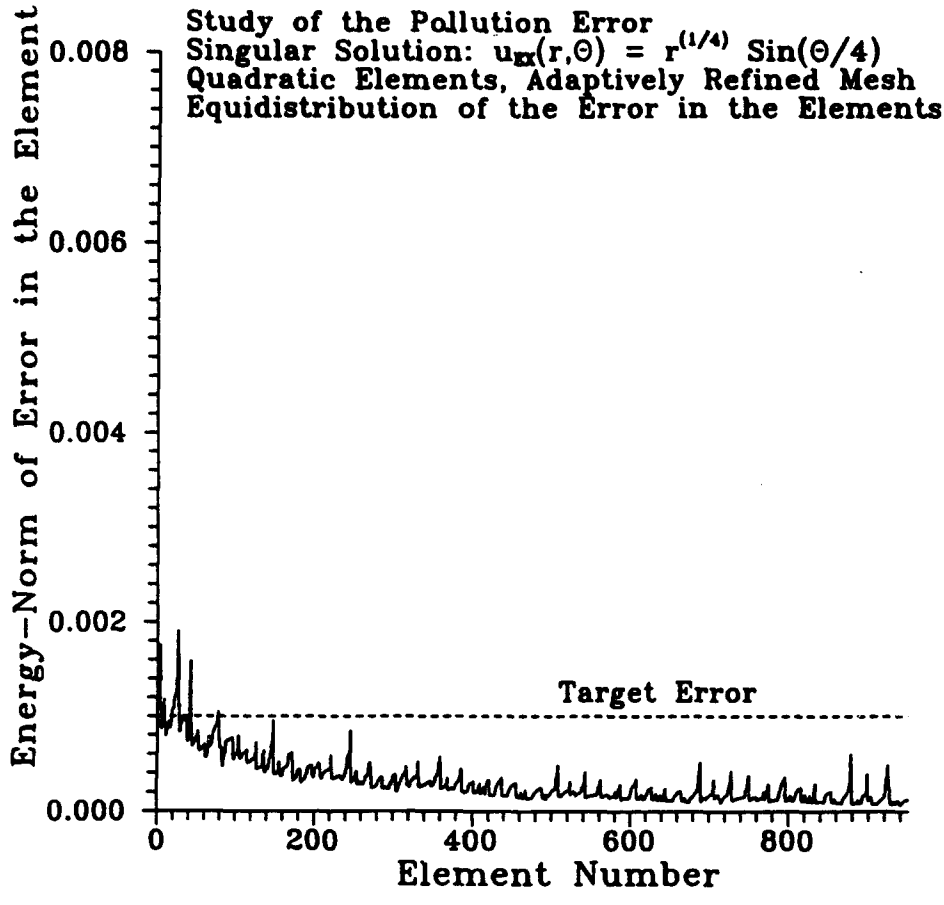

Figure 4.6. Control of the pollution-effect using adaptive grids. Distribution of the energy-norm of the error in the elements of the mesh shown in Fig. 4.5.

Table 4.4. Control of the pollution-effect using adaptive grids. Adaptive grid of quadratic elements generated over the slit-domain using refinement (tolerance = 0.1%, H^1-error norm equidistribution). Comparison of the effectivity index κ_{ω^h}, computed with respect to the exact solution with the the corresponding values of the pollution-free effectivity index $\bar{\kappa}_{\omega^h}$, for the ZZ estimator and the element-residual (ER) estimator, in the mesh-cells $\omega^h_{X_1}$, $\omega^h_{X_2}$ and $\omega^h_{X_3}$ (which consist of the elements connected to the nodes X_1, X_2 and X_3 shown in Fig. 4.5).

Adaptive grid using refinement, H^1-error control, quadratic elements											
Effectivity index κ_{ω^h} in the H^1-norm											
Mesh-cell $\omega^h_{X_1}$				Mesh-cell $\omega^h_{X_2}$				Mesh-cell $\omega^h_{X_3}$			
$\kappa^{ZZ}_{\omega^h_{X_1}}$	$\bar{\kappa}^{ZZ}_{\omega^h_{X_1}}$	$\kappa^{ER}_{\omega^h_{X_1}}$	$\bar{\kappa}^{ER}_{\omega^h_{X_1}}$	$\kappa^{ZZ}_{\omega^h_{X_2}}$	$\bar{\kappa}^{ZZ}_{\omega^h_{X_2}}$	$\kappa^{ER}_{\omega^h_{X_2}}$	$\bar{\kappa}^{ER}_{\omega^h_{X_2}}$	$\kappa^{ZZ}_{\omega^h_{X_3}}$	$\bar{\kappa}^{ZZ}_{\omega^h_{X_3}}$	$\kappa^{ER}_{\omega^h_{X_3}}$	$\bar{\kappa}^{ER}_{\omega^h_{X_3}}$
1.01	1.00	0.97	0.99	0.91	0.97	0.90	0.97	1.00	1.00	0.99	1.00

Table 4.5. Control of the pollution-effect using adaptive grids. Adaptive grid of quadratic elements shown in Fig. 4.5. Effectivity index for element-residual and ZZ estimators for each mesh-layer in the interior of the mesh. Note that the effectivity index κ_{ω_n} computed with respect to the exact solution is very close to the pollution-free values $\bar{\kappa}_{\omega_n}$ for all the layers in the interior of the mesh.

Adaptive grid using refinement, H^1-error control, quadratic elements				
Effectivity index in each mesh layer				
Layer number	Effectivity Index			
	$\kappa_{\omega_n}^{ZZ}$	$\bar{\kappa}_{\omega_n}^{ZZ}$	$\kappa_{\omega_n}^{ER}$	$\bar{\kappa}_{\omega_n}^{ER}$
1	0.954	0.994	0.974	0.996
2	0.996	0.998	0.992	0.997
3	0.992	0.992	0.979	0.992
4	0.974	0.975	0.971	0.974
5	0.971	0.971	0.968	0.971
6	0.861	0.970	0.858	0.970

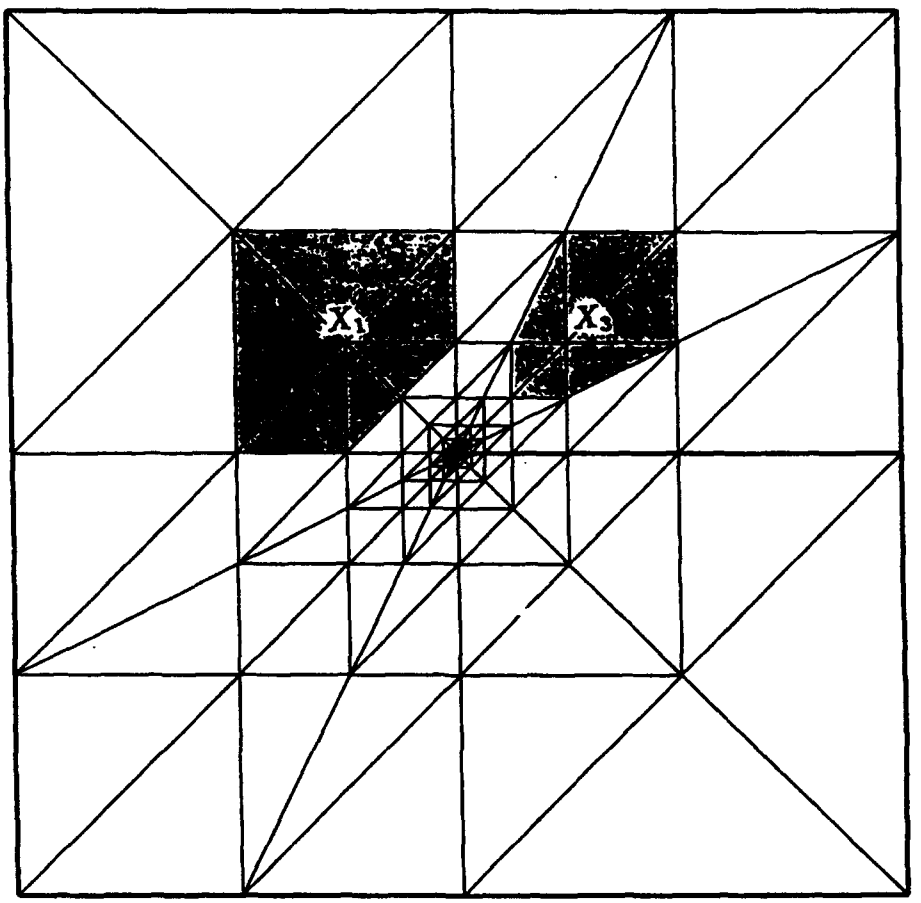

(a)

Figure 4.7. (a) A finite-element grid of cubic elements constructed over the slit-domain using adaptive refinement and a tolerance of 0.04% for the global relative error in the energy-norm; (b) Detail of the finite-element mesh shown in Fig. 4.7a near the singular point with the mesh-cell $\omega^h_{X_2}$.

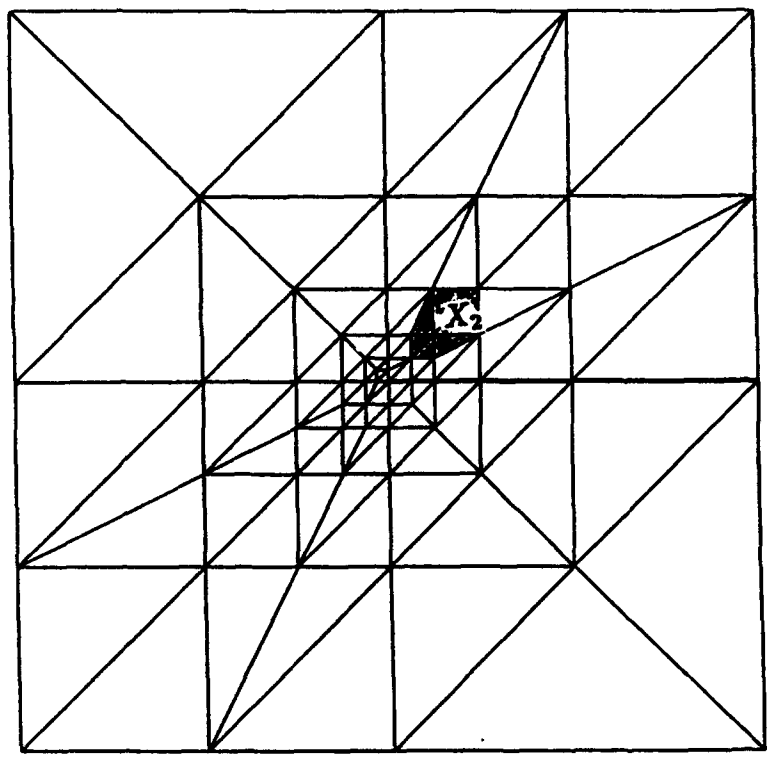

(b)

Figure 4.7. (continued)

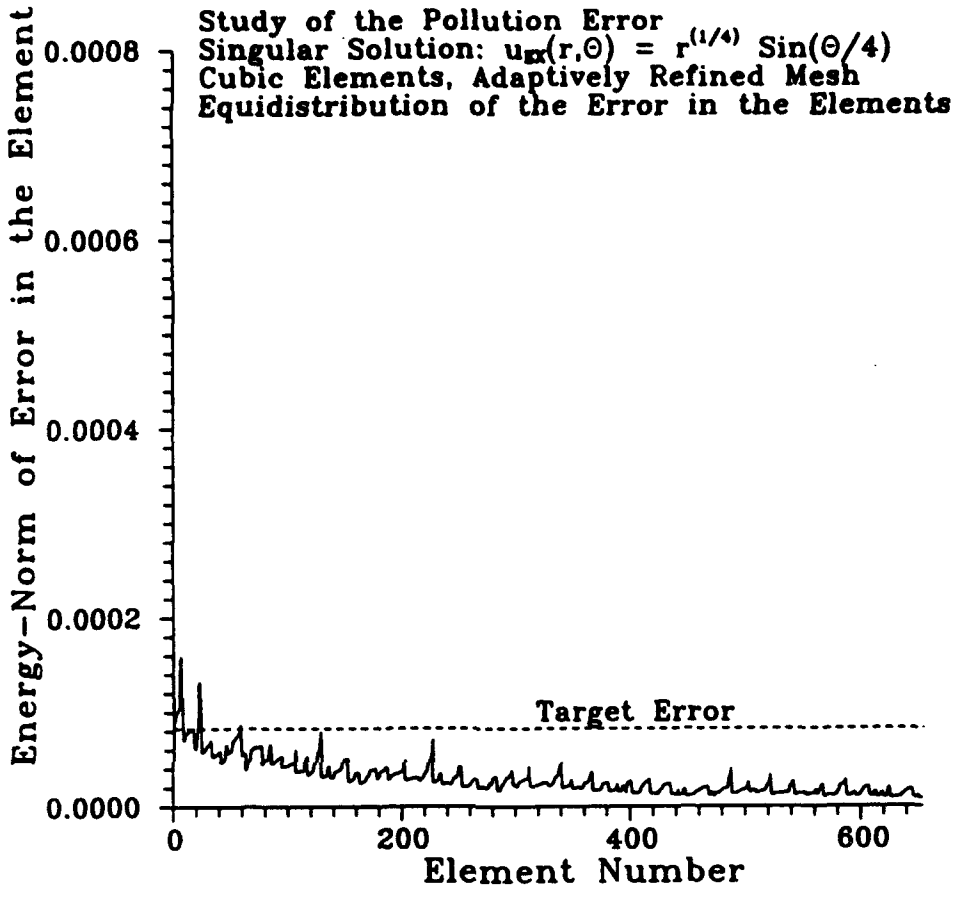

Figure 4.8. Control of the pollution-effect using adaptive grids. Distribution of the energy-norm of the error in the elements of the mesh shown in Fig. 4.7.

Table 4.6. Control of the pollution-effect using adaptive grids. Adaptive grid of cubic elements generated over the slit-domain using refinement (tolerance = 0.05%, H^1-error norm equidistribution). Comparison of the effectivity index κ_{ω^h}, computed with respect to the exact solution, with the corresponding values of the pollution-free effectivity index $\bar{\kappa}_{\omega^h}$, for the ZZ estimator the element-residual (ER) estimator, in the mesh-cells $\omega^h_{X_1}$, $\omega^h_{X_2}$ and $\omega^h_{X_3}$ (which consist of the elements connected to the nodes X_1, X_2 and X_3 shown in Fig. 4.7a).

Adaptive grid using refinement, H^1-error control, cubic elements											
Effectivity index κ_{ω^h} in the H^1-norm											
Mesh-cell $\omega^h_{X_1}$				Mesh-cell $\omega^h_{X_2}$				Mesh-cell $\omega^h_{X_3}$			
$\kappa^{ZZ}_{\omega^h_{X_1}}$	$\bar{\kappa}^{ZZ}_{\omega^h_{X_1}}$	$\kappa^{ER}_{\omega^h_{X_1}}$	$\bar{\kappa}^{ER}_{\omega^h_{X_1}}$	$\kappa^{ZZ}_{\omega^h_{X_2}}$	$\bar{\kappa}^{ZZ}_{\omega^h_{X_2}}$	$\kappa^{ER}_{\omega^h_{X_2}}$	$\bar{\kappa}^{ER}_{\omega^h_{X_2}}$	$\kappa^{ZZ}_{\omega^h_{X_3}}$	$\bar{\kappa}^{ZZ}_{\omega^h_{X_3}}$	$\kappa^{ER}_{\omega^h_{X_3}}$	$\bar{\kappa}^{ER}_{\omega^h_{X_3}}$
0.98	0.99	0.96	0.98	0.86	0.94	0.84	0.93	0.99	0.99	0.97	0.99

Table 4.7. Control of the pollution-effect using adaptive grids. Adaptive grid of cubic elements shown in Fig. 4.7a. Effectivity index for element-residual and ZZ estimators for each mesh-layer in the interior of the mesh. Note that the effectivity index κ_{ω_n} computed with respect to the exact solution is very close to the pollution-free values $\bar{\kappa}_{\omega_n}$ for all the layers in the interior of the mesh.

Adaptive grid using refinement, H^1-error control, cubic elements				
Effectivity index in each mesh layer				
Layer number	Effectivity Index			
	$\kappa_{\omega_n}^{ZZ}$	$\bar{\kappa}_{\omega_n}^{ZZ}$	$\kappa_{\omega_n}^{ER}$	$\bar{\kappa}_{\omega_n}^{ER}$
1	0.952	0.990	0.950	0.986
2	0.991	0.993	0.992	0.997
3	0.976	0.982	0.975	0.980
4	0.922	0.925	0.921	0.924
5	0.898	0.901	0.896	0.901
6	0.862	0.900	0.858	0.900

5 Pollution-effect for meshes refined locally in the interior

As discussed in the Introduction it is a common practice in engineering computations to refine the mesh locally, only in local regions of interest. In this Section we give numerical evidence which shows that: ***Local refinements in a subdomain of interest in the interior of the mesh (where the solution is smooth) do not lead to higher local accuracy unless the mesh is also properly refined in the rest of the domain.*** In particular we demonstrate that if the singular points are not refined and the mesh is refined locally in an interior subdomain Ω_0:

a. The finite element solution in the interior of the subdomain converges to a function which satisfies the differential equation (i.e. it is harmonic) but may be very different from the exact solution of the boundary value problem (i.e. the finite element solution converges to a wrong solution in the interior of the subdomain).

b. The V_1-component of the error converges to zero in the interior of the subdomain while the V_2-component remains practically constant. The error estimators estimate only the V_1-component of the error in the interior of the subdomain and if $|||V_2|||_{\Omega_0} \gg |||V_1|||_{\Omega_0}$ severe underestimation of the error may occur in the interior of the subdomain.

5.1 Convergence of the approximate solution in the interior of the subdomain

We first present a simple numerical example to demonstrate that when the mesh is refined locally in an interior subdomain only, as shown for example in Fig. 5.1, the finite element solution converges to a wrong solution in the interior of the subdomain.

We considered the mixed boundary-value problem for the Laplacian in the L-shaped domain with exact solution $u(r,\theta) = r^{\frac{1}{3}} \sin\left(\frac{\theta}{3}\right)$. The boundary-value problem was solved using the mesh shown in Fig. 5.1 where the domain was meshed by a coarse uniform grid $\left(\text{with mesh-size } h_0 = \frac{1}{4}\right)$ and the subdomain is subdivided uniformly five times $\left(\text{the mesh-size in the subdomain } h = \frac{1}{32} h_0\right)$, and elements of degree p (p = 1, 2 and 3). From the finite element solution we approximated the function $w := u - V_2$ in the subdomain and the exact solution u by their local Taylor-series expansions about the center of the subdomain $x = (x_1^0, x_2^0)$, namely

$$w(x_1,x_2) \approx \alpha_0 + \sum_{q=1}^{q_{max}} \sum_{\ell=1}^{2} \alpha_\ell^{(q)} Q_\ell^{(q)}(x_1 - x_1^0, x_2 - x_2^0)$$

$$u(x_1,x_2) \approx \beta_0 + \sum_{q=1}^{q_{max}} \sum_{\ell=1}^{2} \beta_\ell^{(q)} Q_\ell^{(q)}(x_1 - x_1^0, x_2 - x_2^0)$$

where $Q_\ell^{(q)}$, $\ell = 1,2$ denotes the harmonic monomials of degree q; q_{max} is the maximum degree employed in the harmonic Taylor-series expansions (below we let $q_{max} = 4$); $x^0 = (0.375, 0.375)$ is the center of the subdomain.

In Table 5.1 we report the β-coefficients of the local Taylor-series expansion of the exact solution u and the corresponding α-coefficients of the local Taylor-series expansion of the limit function w for $p = 1$, 2 and 3. Note that the coefficients of the limit-function w are very different from the coefficients of the exact solution u. Hence if the mesh is refined only in an interior subdomain and the mesh outside the subdomain is kept fixed the finite element solution converges to a wrong solution in the interior of the subdomain.

5.2 Asymptotics of the error in the interior of a locally refined subdomain

Here we study the asymptotics of the components $V_1(\Omega_0)$ and $V_2(\Omega_0)$ of the error in the interior of a subdomain Ω_0 as the mesh in the subdomain is successively refined while the mesh outside the subdomain remains fixed.

5.2.1 Locally refined meshes of linear elements

5.2.1.1. Smooth solutions

We solved the boundary-value problem for the Laplace equation in the domain $\Omega = (0,1)^2$ and employed boundary-conditions consistent with the smooth harmonic solution $u(x_1,x_2) = A \sin \pi x_1 \sinh \pi x_2$. In Figure 5.2 we show the domain Ω meshed with a coarse uniform grid with mesh-size $h_0 = \frac{1}{8}$ and the subdomain $\Omega_0 := (0.375, 0.625)^2$ meshed with a finer grid with mesh-size $h = \frac{1}{64}$. We considered linear elements ($p = 1$) and different mesh-sizes in the subdomain shown in Fig. 5.2. In Tables 5.2a, 5.2b we give the values of the components $|||V_1|||^2_{\omega_0^h}$, $|||V_2|||^2_{\omega_0^h}$ and $\int_{\omega_0^h} \nabla V_1 \cdot \nabla V_2$ of the energy-norm of the error, the values of the pollution factors $\mu^{\%}_{\omega_0^h}$ and $\xi^{\%}_{\omega_0^h}$ and the effectivity indices $\kappa_{\omega_0^h}$ and $\kappa'_{\omega_0^h}$ for the shrinking eight-element mesh-cell ω_0^h at the center of the subdomain. Note that, as the mesh-size in the subdomain tends to zero, the pollution factor $\mu^{\%}_{\omega_0^h}$ converges to 100%,

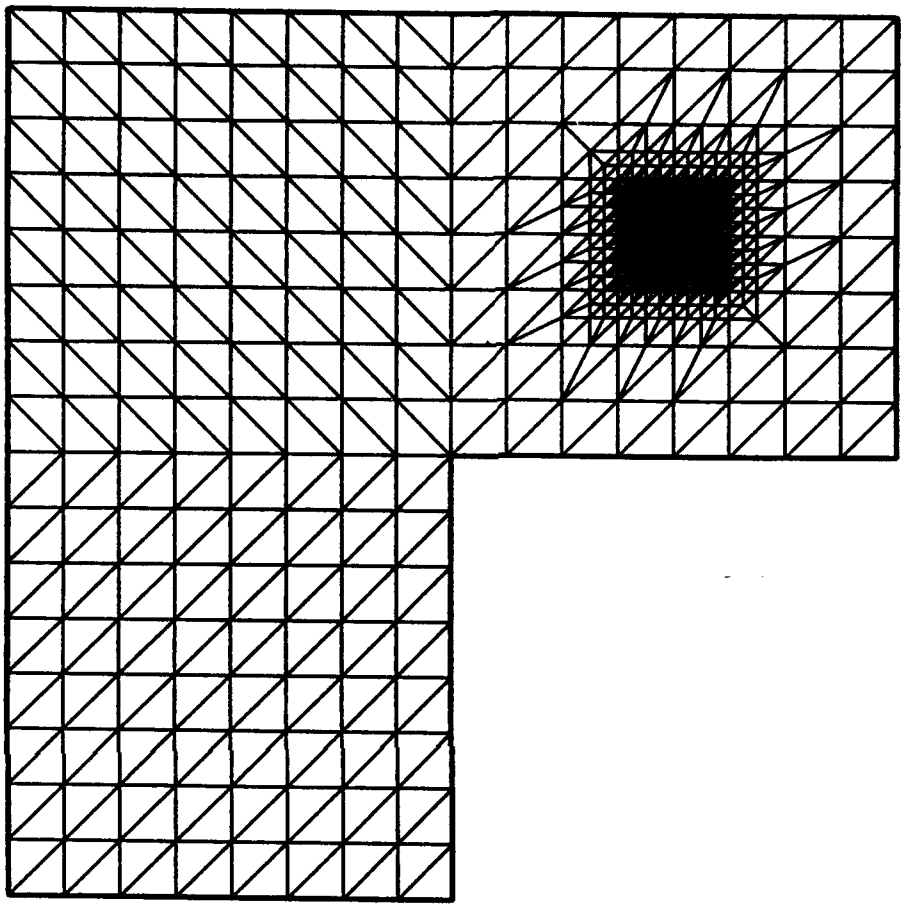

Figure 5.1. Pollution-effect for meshes refined locally in an interior subdomain. The L-shaped domain meshed with a coarse uniform grid with mesh-size $h_0 = \frac{1}{8}\, h$. The mesh has been divided uniformly four times in an interior subdomain Ω_0 $\left(\text{the mesh size in subdomain is } h = \frac{1}{128}\right)$.

Table 5.1. Pollution-effect for meshes refined locally in an interior subdomain. Coefficients of the local Taylor series expansions of the exact solution u and the limit function w about the center of the subdomain $\Omega_0 := (0.5, 0.75)^2$. L-shaped domain shown in Fig. 5.1, exact solution $u(r,\theta) = r^{\frac{1}{3}} \sin \frac{\theta}{3}$, mesh-size in the subdomain $h = \frac{1}{256}$. Note that the β-coefficients of the local Taylor series expansion of u are very different from the α-coefficients of the local Taylor series expansion of the limit function w.

Coefficients of the Taylor series expansion					
Exact solution $u(r,\theta) = r^{\frac{1}{3}} \sin \frac{1}{3}\theta$					
Uniform refinements in the subdomain only					
Exact Solution u		**Limit Function w**			
Coeff. β		Coeff. α	$p=1$	$p=2$	$p=3$
β_0	0.2306	α_0	0.1304	0.1655	0.2016
$\beta_1^{(1)}$	-0.2099	$\alpha_1^{(1)}$	-0.1224	-0.1798	-0.1953
$\beta_2^{(1)}$	0.3637	$\alpha_2^{(1)}$	0.3103	0.3115	0.3311
$\beta_1^{(2)}$	0.1912	$\alpha_1^{(2)}$	0.1160	0.1095	0.1458
$\beta_2^{(2)}$	-0.1025	$\alpha_2^{(2)}$	-0.1729	-0.1834	-0.1196
$\beta_1^{(3)}$	-0.1347	$\alpha_1^{(3)}$	-0.1324	-0.2097	-0.1162
$\beta_2^{(3)}$	0.0777	$\alpha_2^{(3)}$	0.0056	0.0070	0.0128
$\beta_1^{(4)}$	0.0379	$\alpha_1^{(4)}$	0.1422	0.1337	0.0429
$\beta_2^{(4)}$	0.5666	$\alpha_2^{(4)}$	0.2249	0.8150	0.3909

the pollution factor $\xi^{\%}_{\omega_0^h}$ diverges to infinity, the effectivity index $\kappa_{\omega_0^h}$ converges to zero and the effectivity-index $\kappa'_{\omega_0^h}$ converges to one.

In Fig. 5.3a (resp. Fig. 5.3b) we give the graph of the directional derivative of the V_1 - and V_2 -components of the error in the subdomain shown in Fig. 5.2 when the mesh-size in the subdomain is $h = \frac{1}{128}$ (resp. $h = \frac{1}{256}$). Note that the directional derivative of the V_2 -component of the error is very large relative to the directional derivative of the V_1 -component of the error. As the mesh-size in the subdomain is reduced the V_1 -component of the error converges to zero while the V_2 -component remains practically constant.

5.2.1.2. Singular solutions

Next we solved the mixed boundary problem for the Laplace equation and considered the singular solution $u(r,\theta) = r^{\frac{2}{3}} \sin(\frac{2}{3}\theta)$ for linear elements ($p = 1$) and different mesh-sizes in the subdomain shown in Fig. 5.1. In Tables 5.3a, 5.3b we give the values of $|||V_1|||^2_{\omega_0^h}$, $|||V_2|||^2_{\omega_0^h}$ and $\int_{\omega_0^h} \nabla V_1 \cdot \nabla V_2$, the values of the pollution factors $\mu^{\%}_{\omega_0^h}$ and $\xi^{\%}_{\omega_0^h}$, and the effectivity indices $\kappa_{\omega_0^h}$ and $\kappa'_{\omega_0^h}$ for the shrinking eight-element mesh-cell at the center of the subdomain, as the mesh-size in the subdomain tends to zero. Note that, as the mesh-size in the subdomain tends to zero, the pollution factor $\mu^{\%}_{\omega_0^h}$ converges to 100%, the pollution factor $\xi^{\%}_{\omega_0^h}$ diverges to infinity for a larger mesh-size in the subdomain than in the case of the smooth solution, the effectivity index $\kappa_{\omega_0^h}$ for both estimators converges to zero and the effectivity index $\kappa'_{\omega_0^h}$ converges to one.

We also considered the exact solution $u(r,\theta) = r^{\frac{1}{3}} \sin(\frac{1}{3}\theta)$. In Fig. 5.4 we give the graphs of the directional derivative of the V_1 - and V_2 -components of the error in the subdomain shown in Fig. 5.1, along the s-axis shown in Fig. 3.1a, obtained by employing an overkill with $p = 3$, when the mesh-size in the subdomain is $h = \frac{1}{32} h_0$. In Fig. 5.5 we show the detail in the interior of the subdomain for the graphs in Fig. 5.4. Note that the directional derivative of the V_2 -component of the error is very large relative to the directional derivative of the V_1 -component of the error in the subdomain. Also note that the error estimator coincides with the V_1 -component of the error in the interior of the subdomain. In Fig. 5.6 we plot the directional derivative of the V_1 - and V_2 -components of the error along the s-axis shown in Fig. 3.1a when the mesh-size in the subdomain is reduced to $h = \frac{1}{64} h_0$. As the mesh-size in the subdomain is reduced the V_1 -component of the error converges to zero in the subdomain while the V_2 -component of the error remains practically constant.

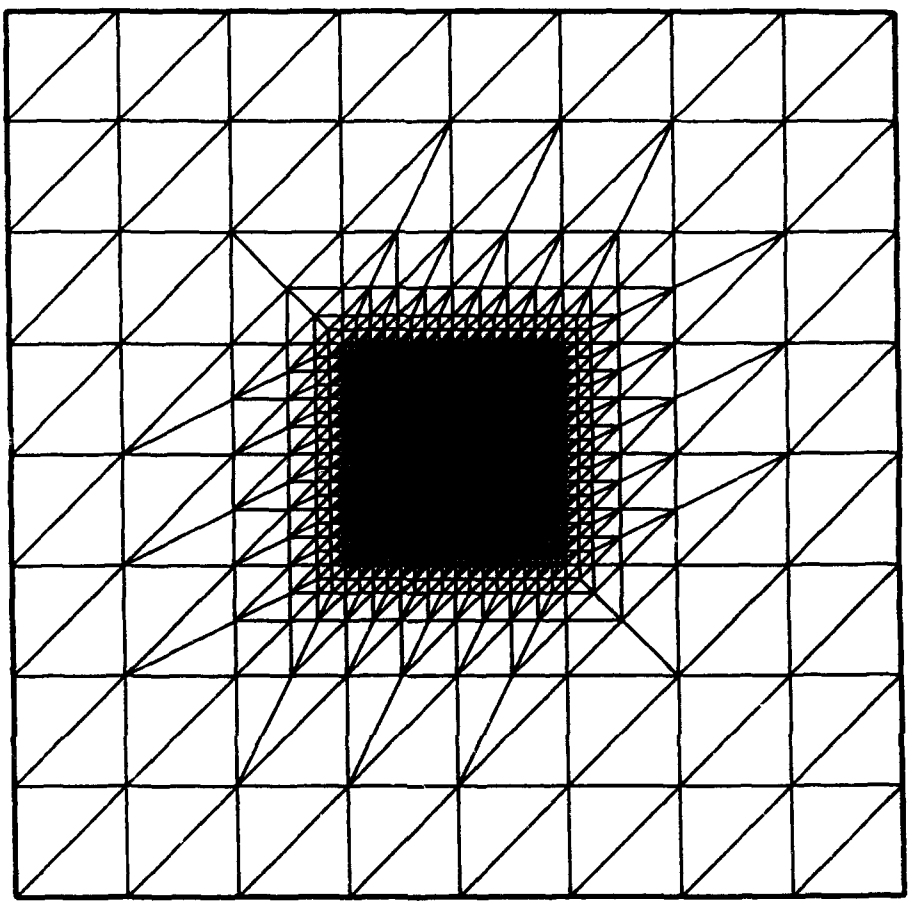

Figure 5.2. Pollution-effect for meshes refined locally in an interior subdomain. The unit-square domain meshed with a coarse uniform grid with mesh size $h_0 = \frac{1}{8}$. The mesh has been divided uniformly five times in an interior subdomain Ω_0 $\left(\text{the mesh-size in the subdomain is } h = \frac{1}{256}\right)$.

Table 5.2a. Components of the energy-norm of the error in ω_0^h. Square domain shown in Fig. 5.2, smooth solution $u(x_1, x_2) = A \sin \pi x_1 \sinh \pi x_2$, $A = 10^3$, $p = 1$. The V_1 - and V_2 -components were determine from the solution u_h for $h = \frac{1}{256}$ using a least square fit over $\Omega_0 = (0.375, 0.625) \times (0.375, 0.625)$.

Components of the energy-norm of the error in ω_0^h					
Exact solution $u(x_1, x_2) = A \sin \pi x_1 \sinh \pi x_2$; linear elements					
Shrinking mesh-cell ω_0^h centered at (0.5, 0.5)					
Uniform mesh refinements in subdomain only					
Mesh-size in the rest of the domain = 0.125					
h	$\|\|\|V_1\|\|\|^2_{\omega_0^h} \cdot 10^{-5}$	$\|\|\|V_2\|\|\|^2_{\omega_0^h} \cdot 10^{-5}$	$-2(\int_{\omega_0^h} \nabla V_1 \cdot \nabla V_2) \cdot 10^{-5}$	$\theta = \cos^{-1}\left[\frac{\int_{\omega_0^h} \nabla V_1 \cdot \nabla V_2}{\|\|\|V_1\|\|\|_{\omega_0^h} \|\|\|V_2\|\|\|_{\omega_0^h}}\right]$	$\|\|\|e_h\|\|\|^2_{\omega_0^h} \cdot 10^{-5}$
0.015625	2.06771	2.39818	0.03693	90.47	4.42896
0.0078125	0.12986	0.60715	0.00325	90.33	0.73376
0.00390625	0.00812	0.15210	0.00021	90.16	0.16001

Table 5.2b. Pollution-effect for meshes refined locally in an interior subdomain. Pollution factors $\mu^{\%}_{\omega_0^h}$ and $\xi^{\%}_{\omega_0^h}$ and effectivity indices in the shrinking mesh-cell ω_0^h. Square domain shown in Fig. 5.2, smooth solution $u(x_1, x_2) = A \sin \pi x_1 \sinh \pi x_2$, $A = 10^3$, $p = 1$. Note that the pollution factor $\mu^{\%}_{\omega_0^h}$ ocnverges to 100%, the pollution factor $\xi^{\%}_{\omega_0^h}$ diverges to infinity and the effectivity index $\kappa_{\omega_0^h}$ converges to zero asymptotically; however the effectivity index $\kappa'_{\omega_0^h}$ converges to one as the mesh-size tends to zero.

Pollution factors and effectivity indices in ω_0^h						
Exact solution $u(x_1, x_2) = A \sin \pi x_1 \sinh \pi x_2$; linear elements						
Shrinking mesh-cell ω_0^h centered at (0.5, 0.5)						
Uniform mesh refinements in subdomain only						
Mesh-size in the rest of the domain = 0.125						
h	$\mu_{\omega_0^h}\%$	$\xi_{\omega_0^h}\%$	$\kappa_{\omega_0^h} = \frac{\mathcal{E}_{\omega_0^h}}{\lvert\lvert\lvert e_h \rvert\rvert\rvert_{\omega_0^h}}$ Effectivity Index		$\kappa'_{\omega_0^h} = \frac{\mathcal{E}_{\omega_0^h}}{\lvert\lvert\lvert v_1 \rvert\rvert\rvert_{\omega_0^h}}$ Effectivity Index	
			$\kappa^{ZZ}_{\omega_0^h}$	$\kappa^{ER}_{\omega_0^h}$	$\kappa'^{ZZ}_{\omega_0^h}$	$\kappa'^{ER}_{\omega_0^h}$
0.015625	73.28	107.69	0.412	0.412	1.001	1.001
0.0078125	90.76	216.22	0.343	0.343	1.001	1.001
0.00390625	97.43	432.83	0.250	0.250	1.000	1.000

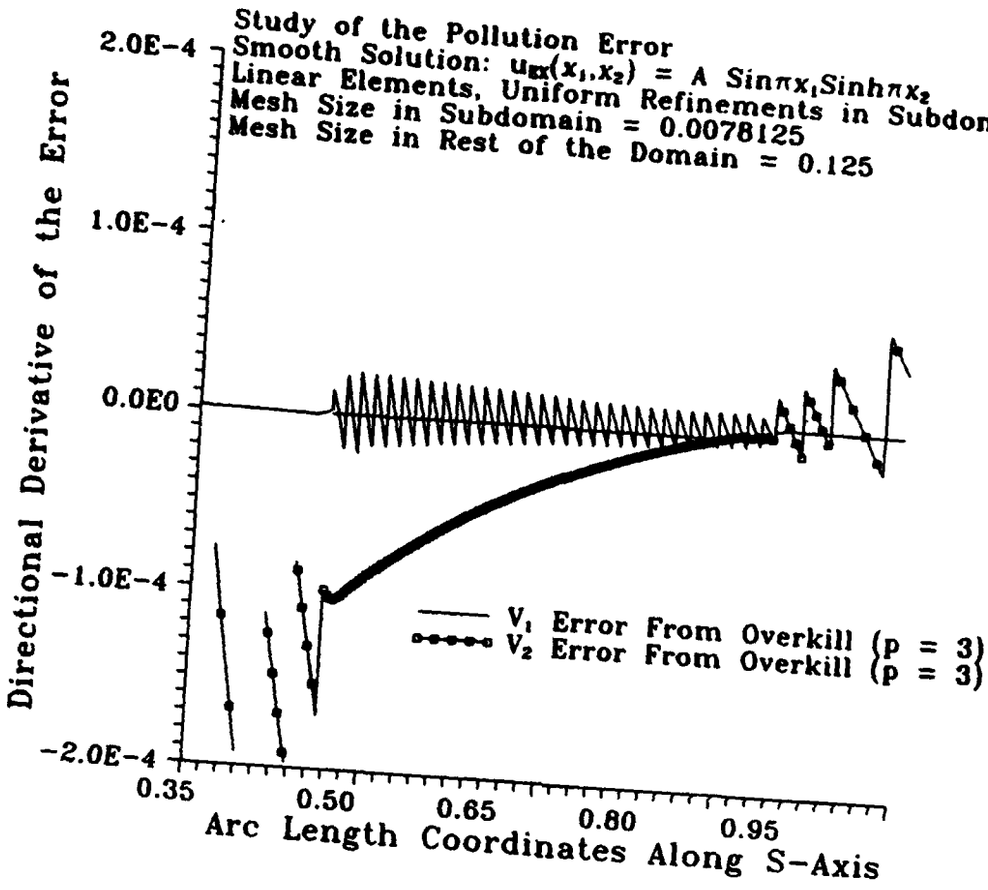

(a)

Figure 5.3. Pollution-effect for meshes refined locally in an interior subdomain. Linear elements, smooth solution $u(x_1, x_2) = A \sin \pi x_1 \sinh \pi x_2$, $A = 10^3$. Unit square domain shown in Fig. 5.2. (a) Uniform mesh-size in the subdomain $h = \frac{1}{128}$. (b) Uniform mesh size in the subdomain $h = \frac{1}{256}$. Directional derivatives of the V_1- and V_2-components of the error obtained from the overkill. Note that $\left|\frac{\partial V_2}{\partial s}\right| \gg \left|\frac{\partial V_1}{\partial s}\right|$ and $(\sigma^{zz} - \nabla u_h) \cdot s \approx \frac{\partial V_1}{\partial s}$, asymptotically, in the interior of the subdomain.

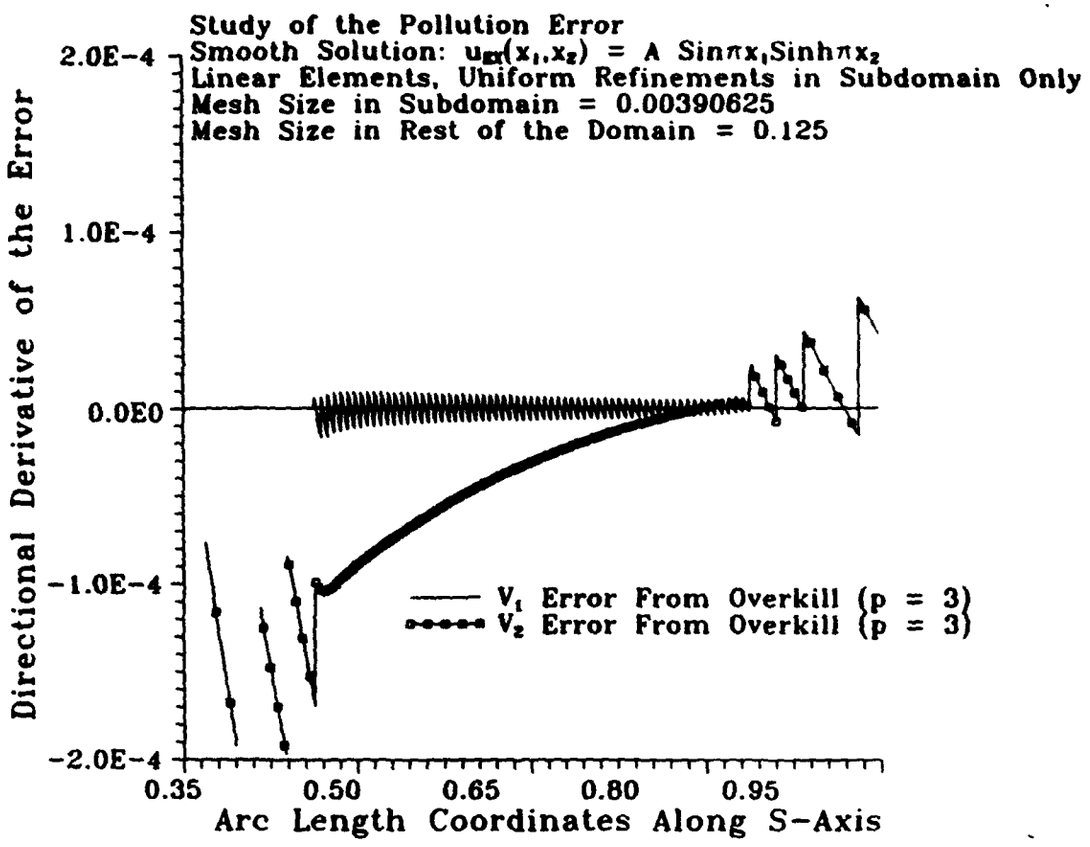

(b)

Figure 5.3. (continued)

Table 5.3a. Pollution-effect for mesh refined locally in an interior subdomain. L-shaped domain shown in Fig. 5.1, $\alpha = \frac{2}{3}$, $p = 1$. The V_1 and V_2 components of the error were obtained from the solution u_h for $h = \frac{1}{256}$ using a least-squares fit over $\Omega_0 = (0.25, 0.75)\times(0.25, 0.75)$.

Components of the energy-norm of the error					
Shrinking mesh-cell centered at (0.5, 0.5)					
Exact solution $u(r,\theta) = r^{\frac{2}{3}}\sin(\frac{2\theta}{3})$; linear elements					
Uniform mesh-refinement in the subdomain only					
Mesh-size in the rest of the domain $h = 0.125$					
Mesh size in subdomain	$\|\|\|V_1\|\|\|^2_{\omega_0^h} \cdot 10^{-6}$	$\|\|\|V_2\|\|\|^2_{\omega_0^h} \cdot 10^{-6}$	$2(\int_{\omega_0^h} \nabla V_1 \cdot \nabla V_2) \cdot 10^{-6}$	$\theta = \cos^{-1}\left[\frac{\int_{\omega_0^h} \nabla V_1 \cdot \nabla V_2}{\|\|\|V_1\|\|\|_{\omega_0^h} \|\|\|V_2\|\|\|_{\omega_0^h}}\right]$	$\|\|\|e_h\|\|\|^2_{\omega_0^h} \cdot 10^{-6}$
0.0625	1.664040	1.144390	0.251316	85.35	3.059750
0.03125	0.097998	0.297721	0.020063	86.63	0.415783
0.015625	0.005994	0.076453	0.000865	88.77	0.083312
0.0078125	0.000374	0.019119	0.000062	89.34	0.019556
0.00390625	0.000023	0.004781	0.000006	89.48	0.004809

Table 5.3b. Pollution-effect for meshes refined locally in an interior subdomain. Pollution-factors $\mu_{\omega_0^h}\%$ and $\xi_{\omega_0^h}\%$ and effectivity indices in shrinking mesh-cell ω_0^h. L-shaped domain shown in Fig. 5.1a, $\alpha = \frac{2}{3}$, $p = 1$. Note that the pollution factor $\mu^{\%}_{\omega_0^h}$ converges to 100%, the pollution factor $\xi^{\%}_{\omega_0^h}$ diverges to infinity, and the effectivity index $\kappa_{\omega_0^h}$ converges to zero. However, the effectivity index $\kappa'_{\omega_0^h}$ converges to one.

Pollution factors and effectivity indices						
Shrinking mesh-cell centered at (0.5, 0.5) **Exact solution $u(r,\theta) = r^{\frac{2}{3}}\sin(\frac{2\theta}{3})$; linear elements**						
Uniform mesh-refinement in the subdomain only						
Mesh-size in the rest of the domain $h = 0.125$						
h	$\mu_{\omega_0^h}\%$	$\xi_{\omega_0^h}\%$	$\kappa_{\omega_0^h} = \frac{\mathcal{E}_{\omega_0^h}}{\lvert\lvert\lvert e_h \rvert\rvert\rvert_{\omega_0^h}}$ Effectivity Index		$\kappa'_{\omega_0^h} = \frac{\mathcal{E}_{\omega_0^h}}{\lvert\lvert\lvert v_1 \rvert\rvert\rvert_{\omega_0^h}}$ Effectivity Index	
			$\kappa^{ZZ}_{\omega_0^h}$	$\kappa^{ER}_{\omega_0^h}$	$\kappa'^{ZZ}_{\omega_0^h}$	$\kappa'^{ER}_{\omega_0^h}$
0.0625	61.15	82.93	0.722	0.722	0.979	0.979
0.03125	84.62	174.29	0.482	0.482	0.992	0.992
0.015625	95.79	357.14	0.268	0.268	1.000	1.000
0.0078125	98.88	714.98	0.138	0.138	1.000	1.000
0.00390625	99.70	1441.76	0.069	0.069	1.000	1.000

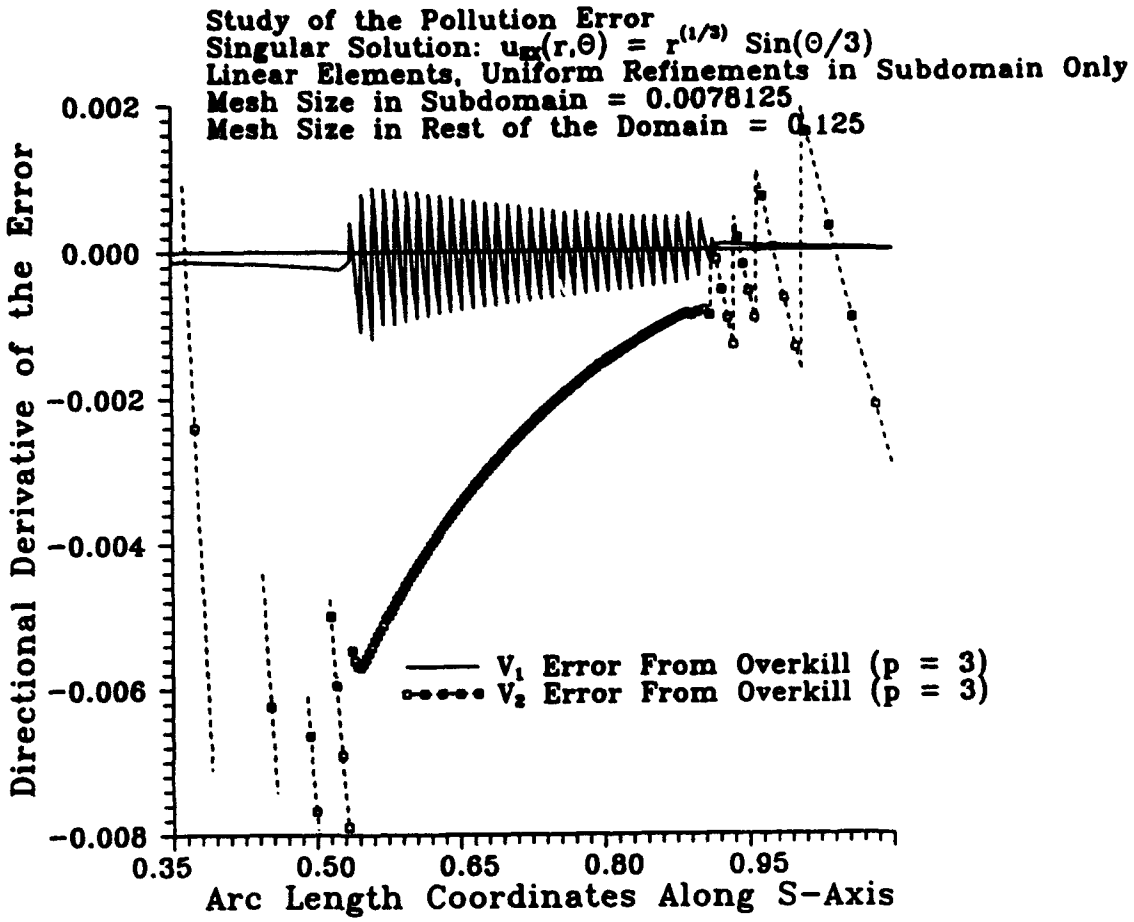

Figure 5.4. Pollution-effect for meshes refined locally in an interior subdomain. Linear elements ($p = 1$), $\alpha = \frac{1}{3}$, L-shaped domain shown in Fig. 5.1. Uniform mesh size in the subdomain $h = \frac{1}{128}$. Directional derivatives of the V_1- and V_2-components of the error obtained from the *overkill*. Note that $\left|\frac{\partial V_2}{\partial s}\right| \gg \left|\frac{\partial V_1}{\partial s}\right|$ and $(\sigma^{zz} - \nabla u_h)\cdot s \approx \frac{\partial V_1}{\partial s}$, asymptotically, in the interior of the subdomain.

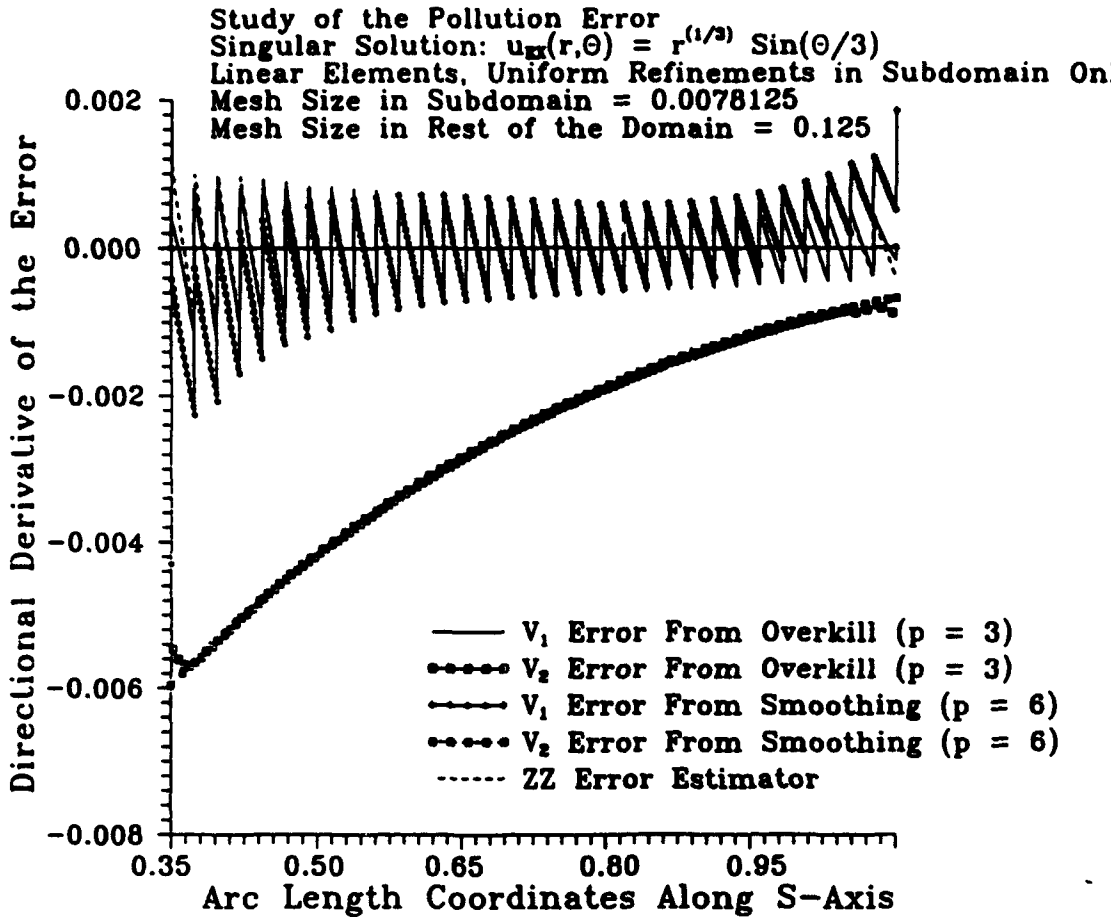

Figure 5.5. Pollution-effect for meshes refined locally in an interior subdomain. Linear elements ($p = 1$), $\alpha = \frac{1}{3}$, L-shaped domain shown in Fig. 5.1. Uniform mesh size in the subdomain $h = \frac{1}{128}$. Directional derivatives of the V_1 - and V_2 -components of the error and the ZZ error estimator in the subdomain Ω_0. Comparison between the values obtained from *smoothing* and *overkill*. Note that the directional derivatives of V_1 and V_2 obtained from smoothing and overkill coincide exactly and $(\sigma^{ZZ} - \nabla u_h) \cdot s \approx \frac{\partial V_1}{\partial s}$ in the interior of the subdomain.

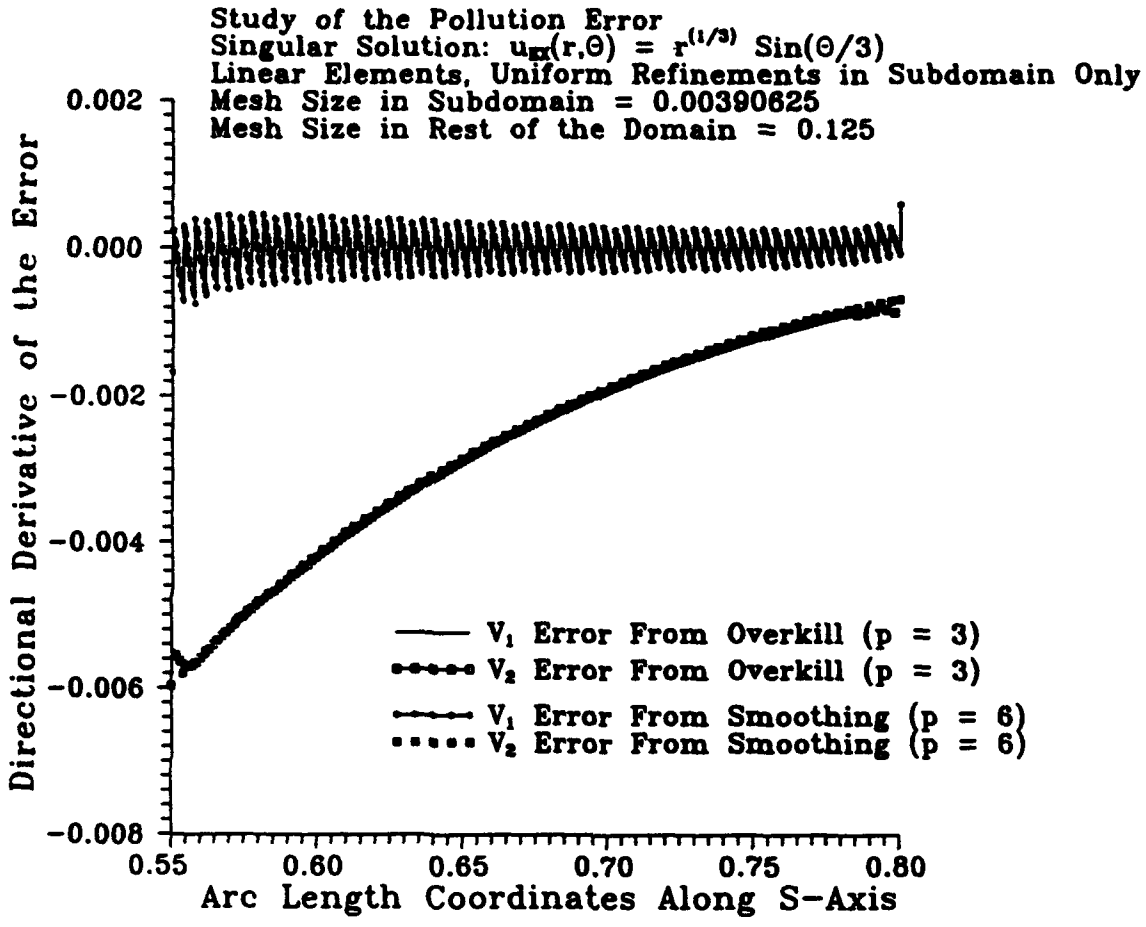

Figure 5.6. Pollution effect for grids refined locally in an interior subdomain. Linear elements ($p = 1$), $\alpha = \frac{1}{3}$, L-shaped domain shown in Fig. 5.1, Uniform mesh size in the subdomain $h = \frac{1}{256}$. Directional derivatives of the V_1- and V_2-components of the error. Note that $\left|\frac{\partial V_2}{\partial s}\right| \gg \frac{\partial V_1}{\partial s}$ asymptotically, in the interior of the subdomain.

5.2.2 Locally refined meshes of quadratic elements

5.2.2.1. Smooth solution

We considered the same boundary-value problem as in Section 5.2.1.1 with the smooth harmonic solution $u(x_1, x_2) = A \sin \pi x_1 \sinh \pi x_2$ and employed meshes of quadratic elements ($p = 2$) with various mesh-sizes in the subdomain shown in Fig. 5.2. In Table 5.4a, 5.4b we report the values of the pollution factors and the effectivity indices for different mesh-sizes in the subdomain. Once again we note that the pollution-factor $\mu^{\%}_{\omega_0^h}$ converges to 100%, the pollution factor $\xi^{\%}_{\omega_0^h}$ diverges to infinity and the effectivity index $\kappa_{\omega_0^h}$ converges to zero as the mesh-size in the subdomain tends to zero.

5.2.2.2. Singular solutions

We solved the mixed boundary value problem for the Laplacian with boundary-conditions consistent with the exact solution $u(r, \theta) = r^{\frac{4}{3}} \sin(\frac{4}{3}\theta)$ fand employed meshes of quadratic elements ($p = 2$) with various mesh-sizes in the subdomain shown in Fig. 5.7. In Tables 5.5a, 5.5b we give the values of $|||V_1|||^2_{\omega_0^h}$, $|||V_2|||^2_{\omega_0^h}$ and $\int_{\omega_0^h} \nabla V_1 \cdot \nabla V_2$, the values of the pollution factors $\mu^{\%}_{\omega_0^h}$ and $\xi^{\%}_{\omega_0^h}$, and effectivity indices $\kappa_{\omega_0^h}$ and $\kappa'_{\omega_0^h}$ in the shrinking eight-element mesh-cell at the center of the subdomain, as the mesh-size in the subdomain tends to zero. Again, we note that the percentage of pollution in the shrinking mesh-cell at the center of the subdomain converges to 100%, the pollution factor $\xi^{\%}_{\omega_0^h}$ diverges to infinity, the effectivity index $\kappa_{\omega_0^h}$ for both estimators converges to zero and the effectivity index $\kappa'_{\omega_0^h}$ converges to one. Also note that compared with the results in Table 5.2, we see that the pollution-effect is stronger for larger values of the mesh-size in the subdomain.

We also considered the exact solution $u(r, \theta) = r^{\frac{2}{3}} \sin(\frac{2}{3}\theta)$. In Fig. 5.8a (resp. Fig. 5.8b) we show the graph of the directional derivative of the V_1- and V_2-components of the error in the subdomain shown in Fig. 5.7, along the s-axis shown in Fig. 3.1b, where the mesh-size in the subdomain is $h = \frac{1}{32}$ (resp. $h = \frac{1}{128}$). Note that the directional derivative V_2-component is significantly greater than the directional derivative V_1-component of the error in the interior of the subdomain. Further note that as the mesh-size in the subdomain is reduced, the V_1-component of the error converges to zero while the V_2-component remains constant. Also note that the error estimator coincides with the V_1-component of the error.

Table 5.4a. Components of the energy-norm of the error in ω_0^h. Square domain shown in Fig. 5.2, smooth solution $u(x_1, x_2) = A \sin \pi x_1 \sinh \pi x_2$, $A = 10^3$, $p = 2$. The V_1- and V_2-components were determine from the solution u_h for $h = \frac{1}{256}$ using a least square fit over $\Omega_0 = (0.375, 0.625) \times (0.375, 0.625)$.

Components of the energy-norm of the error in ω_0^h					
Exact solution $u(x_1, x_2) = A \sin \pi x_1 \sinh \pi x_2$; quadratic elements					
Shrinking mesh-cell ω_0^h centered at (0.5, 0.5)					
Uniform mesh refinements in subdomain only					
Mesh-size in the rest of the domain = 0.125					
h	$\|\|\|V_1\|\|\|^2_{\omega_0^h} \cdot 10^{-8}$	$\|\|\|V_2\|\|\|^2_{\omega_0^h} \cdot 10^{-8}$	$-2(\int_{\omega_0^h} \nabla V_1 \cdot \nabla V_2) \cdot 10^{-8}$	$\theta = \cos^{-1}\left[\frac{\int_{\omega_0^h} \nabla V_1 \cdot \nabla V_2}{\|\|\|V_1\|\|\|_{\omega_0^h} \|\|\|V_2\|\|\|_{\omega_0^h}}\right]$	$\|\|\|e_h\|\|\|^2_{\omega_0^h} \cdot 10^{-8}$
0.015625	0.246768	3.301960	0.0053241	89.83	3.554050
0.0078125	0.003850	0.824801	0.0000704	89.96	0.828722
0.00390625	0.000061	0.205921	0.0000008	90.00	0.205981

Table 5.4b. Pollution-effect for meshes refined locally in an interior subdomain. Pollution factors $\mu^{\%}_{\omega_0^h}$ and $\xi^{\%}_{\omega_0^h}$ and effectivity indices in the shrinking mesh-cell ω_0^h. Square domain shown in Fig. 5.2, smooth solution $u(x_1, x_2) = A \sin \pi x_1 \sinh \pi x_2$, $A = 10^3$, $p = 2$. Note that the pollution factor $\mu^{\%}_{\omega_0^h}$ ocnverges to 100%, the pollution factor $\xi^{\%}_{\omega_0^h}$ diverges to infinity and the effectivity index $\kappa_{\omega_0^h}$ converges to zero asymptotically; however the effectivity index $\kappa'_{\omega_0^h}$ converges to one as the mesh-size tends to zero.

Pollution factors and effectivity indices in ω_0^h						
Exact solution $u(x_1, x_2) = A \sin \pi x_1 \sinh \pi x_2$; quadratic elements						
Shrinking mesh-cell ω_0^h centered at (0.5, 0.5)						
Uniform mesh refinements in subdomain only						
Mesh-size in the rest of the domain = 0.125						
h	$\mu_{\omega_0^h}\%$	$\xi_{\omega_0^h}\%$	$\kappa_{\omega_0^h} = \frac{\mathcal{E}_{\omega_0^h}}{\lvert\lvert\lvert e_h \rvert\rvert\rvert_{\omega_0^h}}$ Effectivity Index		$\kappa'_{\omega_0^h} = \frac{\mathcal{E}_{\omega_0^h}}{\lvert\lvert\lvert V_1 \rvert\rvert\rvert_{\omega_0^h}}$ Effectivity Index	
			$\kappa^{ZZ}_{\omega_0^h}$	$\kappa^{ER}_{\omega_0^h}$	$\kappa'^{ZZ}_{\omega_0^h}$	$\kappa'^{ER}_{\omega_0^h}$
0.015625	96.46	365.79	0.245	0.241	1.013	0.998
0.0078125	99.76	1463.63	0.062	0.061	1.010	1.000
0.00390625	99.98	5851.72	0.016	0.015	1.010	0.999

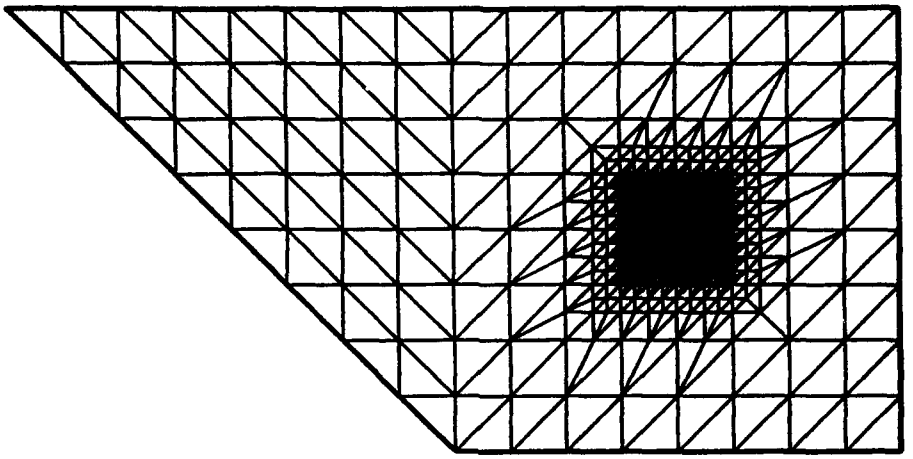

Figure 5.7. Pollution-effect for meshes refined locally in an interior subdomain. The convex domain meshed with a coarse uniform grid with mesh-size $h_0 = \frac{1}{8}$. The mesh has been divided uniformly four times in an interior subdomain Ω_0 $\left(\text{the mesh-size in the subdomain is } h = \frac{1}{128}\right)$.

Table 5.5a. Pollution-effect for meshes refined locally in an interior subdomain. Convex domain shown in Fig. 5.7, $\alpha = \frac{4}{3}$, $p = 2$ $(2\alpha > p)$. The V_1 and V_2 components of the error were determined from the solution u_h for $h = \frac{1}{3}$ using a least-squares fit over $\Omega_0 = (0.25, 0.75)\times(0.25, 0.75)$.

Components of the energy-norm of the error					
Shrinking mesh-cell centered at (0.5, 0.5)					
Exact solution $u(r,\theta) = r^{\frac{1}{3}}\sin(\frac{4\theta}{3})$; quadratic elements					
Uniform mesh-refinement in the subdomain only					
Mesh-size in the rest of the domain $h = 0.125$					
Mesh size in subdomain	$\|\|\|V_1\|\|\|^2_{\omega_0^h} \cdot 10^{-10}$	$\|\|\|V_2\|\|\|^2_{\omega_0^h} \cdot 10^{-10}$	$2(\int_{\omega_0^h} \nabla V_1 \cdot \nabla V_2) \cdot 10^{-10}$	$\theta = \cos^{-1}\left[\frac{\int_{\omega_0^h} \nabla V_1 \cdot \nabla V_2}{\|\|\|V_1\|\|\|_{\omega_0^h} \|\|\|V_2\|\|\|_{\omega_0^h}}\right]$	$\|\|\|e_h\|\|\|^2_{\omega_0^h} \cdot 10^{-10}$
0.0625	4.692720	0.161097	0.0080028	90.26	4.845800
0.03125	0.072353	0.020709	0.0000135	90.01	0.093049
0.015625	0.001127	0.004960	0.0000010	90.01	0.006087
0.0078125	0.000018	0.001236	0.0000006	90.11	0.001254

Table 5.5b. Pollution-effect for meshes refined locally in an interior subdomain. Pollution factors $\mu^{\%}_{\omega_0^h}$ and $\xi^{\%}_{\omega_0^h}$ and effectivity indices in the shrinking mesh-cell ω_0^h. Convex domain shown in Fig. 5.7, $\alpha = \frac{4}{3}$, $p = 2$ $(2\alpha > p)$. Note that the pollution factor $\mu^{\%}_{\omega_0^h}$ converges to 100%, the pollution factor $\xi^{\%}_{\omega_0^h}$ diverges to infinity, and the effectivity index $\kappa_{\omega_0^h}$ converges to zero. However, the effectivity index $\kappa'_{\omega_0^h}$ converges to one.

Pollution factors and effectivity indices						
Shrinking mesh-cell centered at (0.5, 0.5) **Exact solution $u(r,\theta) = r^{\frac{1}{3}}\sin(\frac{4\theta}{3})$; quadratic elements**						
Uniform mesh-refinement in the subdomain only						
Mesh-size in the rest of the domain $h = 0.125$						
h	$\mu_{\omega_0^h}\%$	$\xi_{\omega_0^h}\%$	$\kappa_{\omega_0^h} = \frac{\varepsilon_{\omega_0^h}}{\lvert\lvert\lvert e_h \rvert\rvert\rvert_{\omega_0^h}}$ Effectivity Index		$\kappa'_{\omega_0^h} = \frac{\varepsilon_{\omega_0^h}}{\lvert\lvert\lvert v_1 \rvert\rvert\rvert_{\omega_0^h}}$ Effectivity Index	
			$\kappa^{ZZ}_{\omega_0^h}$	$\kappa^{ER}_{\omega_0^h}$	$\kappa'^{ZZ}_{\omega_0^h}$	$\kappa'^{ER}_{\omega_0^h}$
0.0625	18.22	18.52	0.991	0.983	1.00	1.00
0.03125	47.17	53.50	0.889	0.882	1.00	1.00
0.015625	90.26	209.78	0.434	0.430	1.00	1.00
0.0078125	99.29	828.65	0.118	0.118	1.00	1.00

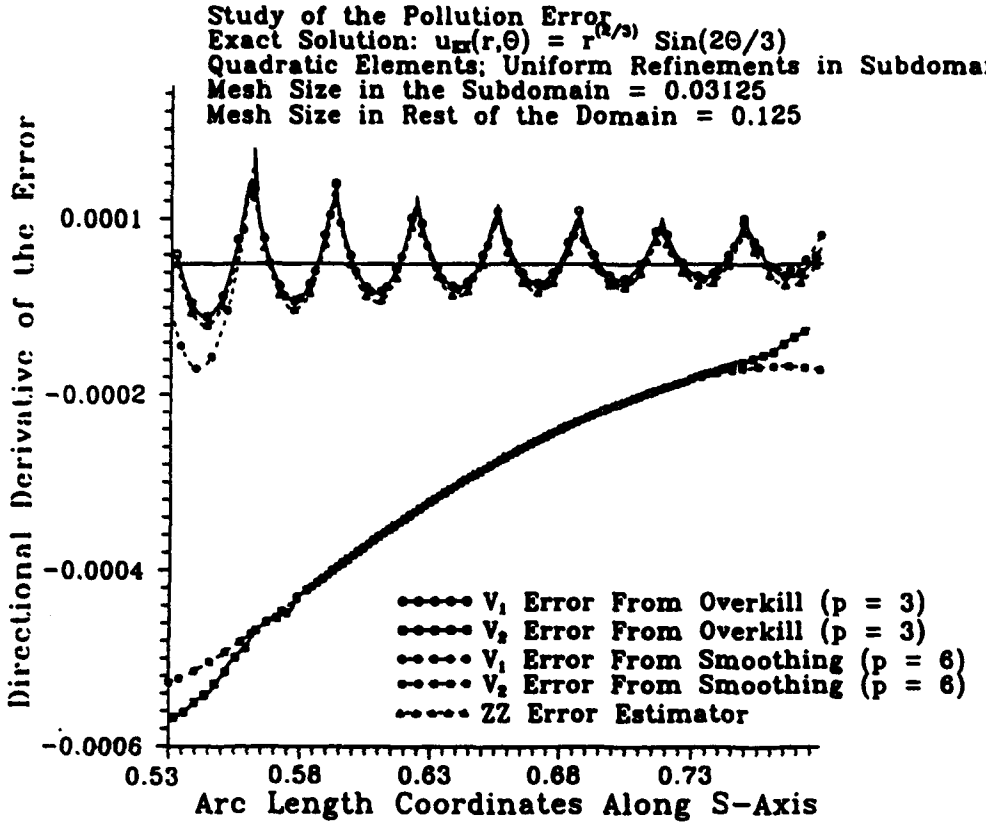

(a)

Figure 5.8. Pollution-effect for meshes refined locally in an interior subdomain. Quadratic elements ($p = 2$), $\alpha = \frac{2}{3}$. Directional derivatives of the V_1- and V_2-components of the error and the ZZ error estimator along the s axis as shown in Fig. 3.1b. (a) Uniform mesh-size in the subdomain $h = \frac{1}{32}$; (b) Uniform mesh-size in the subdomain $h = \frac{1}{128}$. Note that $\left|\frac{\partial V_2}{\partial s}\right| \gg \left|\frac{\partial V_1}{\partial s}\right|$ and $(\sigma^{ZZ} - \nabla u_h)\cdot s \approx \frac{\partial V_1}{\partial s}$, asymptotically, in the interior of the subdomain.

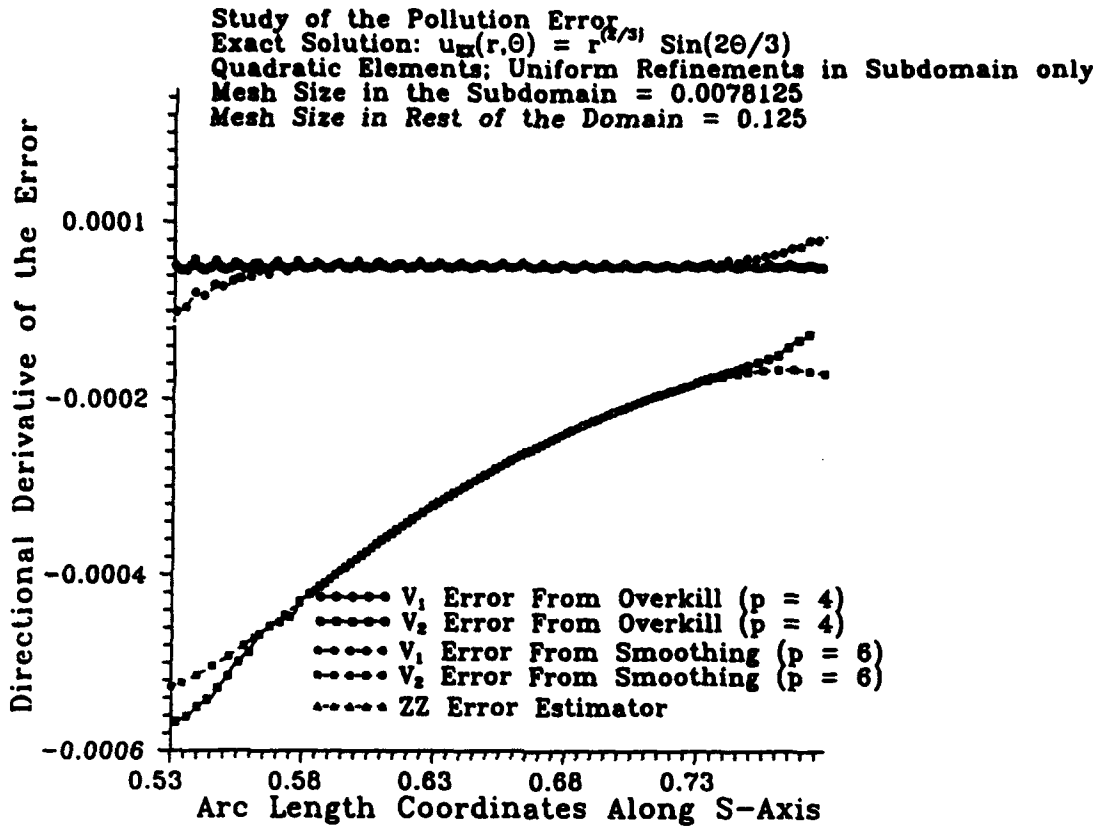

(b)

Figure 5.8. (continued)

5.2.3 Locally refined meshes of cubic elements

5.2.3.1. Smooth solution

We considered the same boundary-value problem as in Section 5.2.1.1 with the smooth solution $u(x_1, x_2) = A \sin \pi x_1 \sinh \pi x_2$ and employed meshes of cubic elements ($p = 3$) with various mesh-sizes in the subdomain. In Tables 5.6a, 5.6b we give the values of $|||V_1|||^2_{\omega_0^h}$, $|||V_2|||^2_{\omega_0^h}$ and $\int_{\omega_0^h} \nabla V_1 \cdot V_2$, the values of the pollution factors $\mu^{\%}_{\omega_0^h}$ and $\xi^{\%}_{\omega_0^h}$ and the values of the effectivity index $\kappa_{\omega_0^h}$ and $\kappa'_{\omega_0^h}$. We note that, as the mesh-size in the subdomain tends to zero, the pollution factor $\mu^{\%}_{\omega_0^h}$ converges to 100%, $\xi^{\%}_{\omega_0^h}$ diverges to infinity and the effectivity index $\kappa_{\omega_0^h}$ converges to zero.

5.2.3.2. Singular solution

We also solved the mixed boundary value problem for the Laplacian with boundary conditions consistent with the exact solution $u(r, \theta) = r^{\frac{6}{5}} \sin(\frac{6}{5}\theta)$ and employed meshes of cubic elements ($p = 3$) with various mesh-sizes in the subdomain shown in Fig. 5.9. In Fig. 5.10a (resp. Fig. 5.10b) we show the graph of the directional derivative of the V_1 - and V_2 -components of the error in the subdomain, along the s-axis shown in Fig. 3.1c, where the mesh-size in the subdomain is $h = \frac{1}{32}$ (resp. $h = \frac{1}{128}$). Once again we note that as the mesh-size in the subdomain tends to zero the V_2 -component of the error remains constant while the V_1 -component converges to zero. Also note that the error estimator follows the V_1 -component of the error and that the V_2 -component is the dominant part of the error in the interior of the subdomain.

5.3 Summary of the results for the pollution-effect for locally refined meshes

In summary we observe that if the mesh is refined locally in an interior subdomain only

(i). As the mesh size in the subdomain tends to zero the V_1 -component of the error converges to zero in the interior of the subdomain while the V_2 -component remains practically constant.

(ii). The value of relative magnitude of $\frac{|||V_1|||_{\omega_0^h}}{|||V_2|||_{\omega_0^h}}$, which measures the pollution-effect in the interior of the subdomain for a given grid, depends on the mesh-size in the subdomain (compared to the mesh-size of the outside mesh), the smoothness of the solution and the degree p of the elements.

Table 5.6a. Components of the energy-norm of the error in ω_0^h. Square domain shown in Fig. 5.2, smooth solution $u(x_1, x_2) = A \sin \pi x_1 \sinh \pi x_2$, $A = 10^3$, $p = 3$. The V_1 - and V_2 -components were determine from the solution u_h for $h = \frac{1}{256}$ using a least square fit over $\Omega_0 = (0.375, 0.625) \times (0.375, 0.625)$.

Components of the energy-norm of the error in ω_0^h					
Exact solution $u(x_1, x_2) = A \sin \pi x_1 \sinh \pi x_2$; cubic elements					
Shrinking mesh-cell ω_0^h centered at (0.5, 0.5)					
Uniform mesh refinements in subdomain only					
Mesh-size in the rest of the domain = 0.125					
h	$\|\|\|V_1\|\|\|^2_{\omega_0^h} \cdot 10^{-12}$	$\|\|\|V_2\|\|\|^2_{\omega_0^h} \cdot 10^{-12}$	$-2(\int_{\omega_0^h} \nabla V_1 \cdot \nabla V_2) \cdot 10^{-12}$	$\theta = \cos^{-1}\left[\frac{\int_{\omega_0^h} \nabla V_1 \cdot \nabla V_2}{\|\|\|V_1\|\|\|_{\omega_0^h} \|\|\|V_2\|\|\|_{\omega_0^h}}\right]$	$\|\|\|e_h\|\|\|^2_{\omega_0^h} \cdot 10^{-12}$
0.015625	0.047745	6.454031	0.011364	90.58	6.490410
0.0078125	0.000213	1.598780	0.000764	91.18	1.598221
0.00390625	0.000003	0.039879	0.000066	91.85	0.039816

Table 5.6b. Pollution-effect for meshes refined locally in an interior subdomain. Pollution factors $\mu^{\%}_{\omega_0^h}$ and $\xi^{\%}_{\omega_0^h}$ and effectivity indices in the shrinking mesh-cell ω_0^h. Square domain shown in Fig. 5.2, smooth solution $u(x_1, x_2) = A \sin \pi x_1 \sinh \pi x_2$, $A = 10^3$, $p = 3$. Note that the pollution factor $\mu^{\%}_{\omega_0^h}$ converges to 100%, the pollution factor $\xi^{\%}_{\omega_0^h}$ diverges to infinity and the effectivity index $\kappa_{\omega_0^h}$ converges to zero asymptotically; however the effectivity index $\kappa'_{\omega_0^h}$ converges to one as the mesh-size tends to zero.

Pollution factors and effectivity indices in ω_0^h						
Exact solution $u(x_1, x_2) = A \sin \pi x_1 \sinh \pi x_2$; cubic elements						
Shrinking mesh-cell ω_0^h centered at (0.5, 0.5)						
Uniform mesh refinements in subdomain only						
Mesh-size in the rest of the domain = 0.125						
h	$\mu_{\omega_0^h}\%$	$\xi_{\omega_0^h}\%$	$\kappa_{\omega_0^h} = \frac{\mathcal{E}_{\omega_0^h}}{\lvert\lvert\lvert e_h \rvert\rvert\rvert_{\omega_0^h}}$ Effectivity Index		$\kappa'_{\omega_0^h} = \frac{\mathcal{E}_{\omega_0^h}}{\lvert\lvert\lvert V_1 \rvert\rvert\rvert_{\omega_0^h}}$ Effectivity Index	
			$\kappa^{ZZ}_{\omega_0^h}$	$\kappa^{ER}_{\omega_0^h}$	$\kappa'^{ZZ}_{\omega_0^h}$	$\kappa'^{ER}_{\omega_0^h}$
0.015625	99.63	1162.65	0.081	0.080	0.993	0.991
0.0078125	99.99	8644.49	0.037	0.037	0.992	0.992
0.00390625	99.99	39370.32	0.008	0.008	0.994	0.994

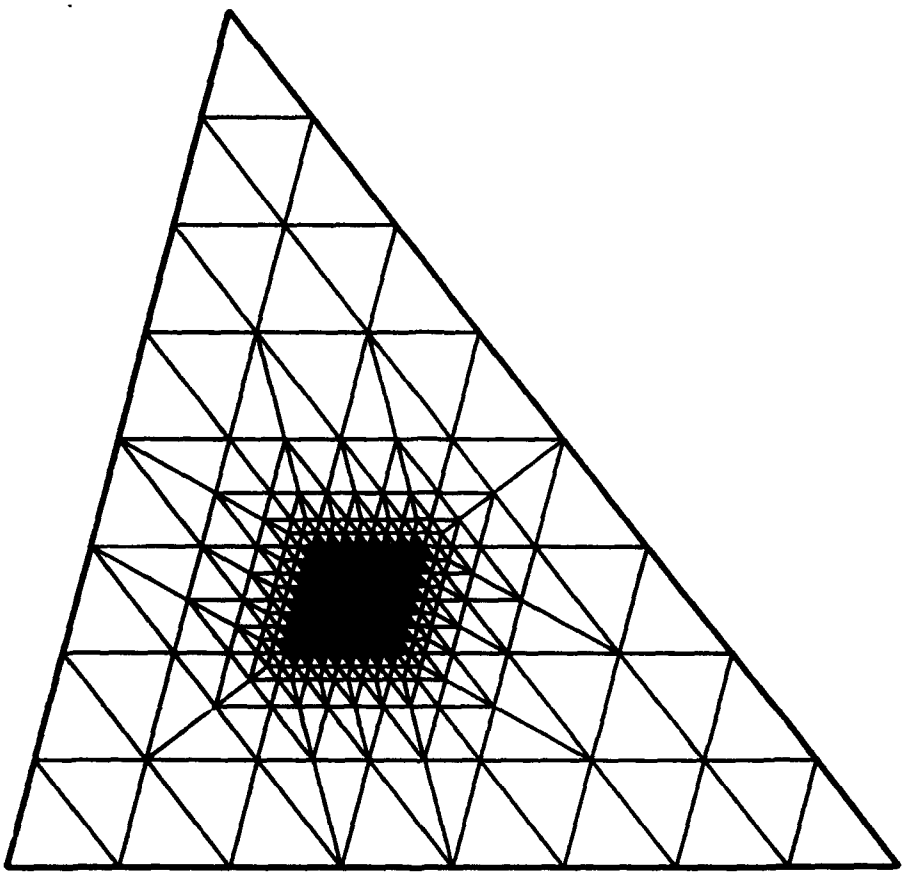

Figure 5.9. Pollution-effect for meshes refined locally in an interior subdomain. The triangular domain meshed with a coarse uniform grid with mesh-size $h_0 = \frac{1}{8}$. The mesh has been divided uniformly four times in an interior subdomain Ω_0 $\left(\text{the mesh-size in the subdomain is } h = \frac{1}{128}\right)$.

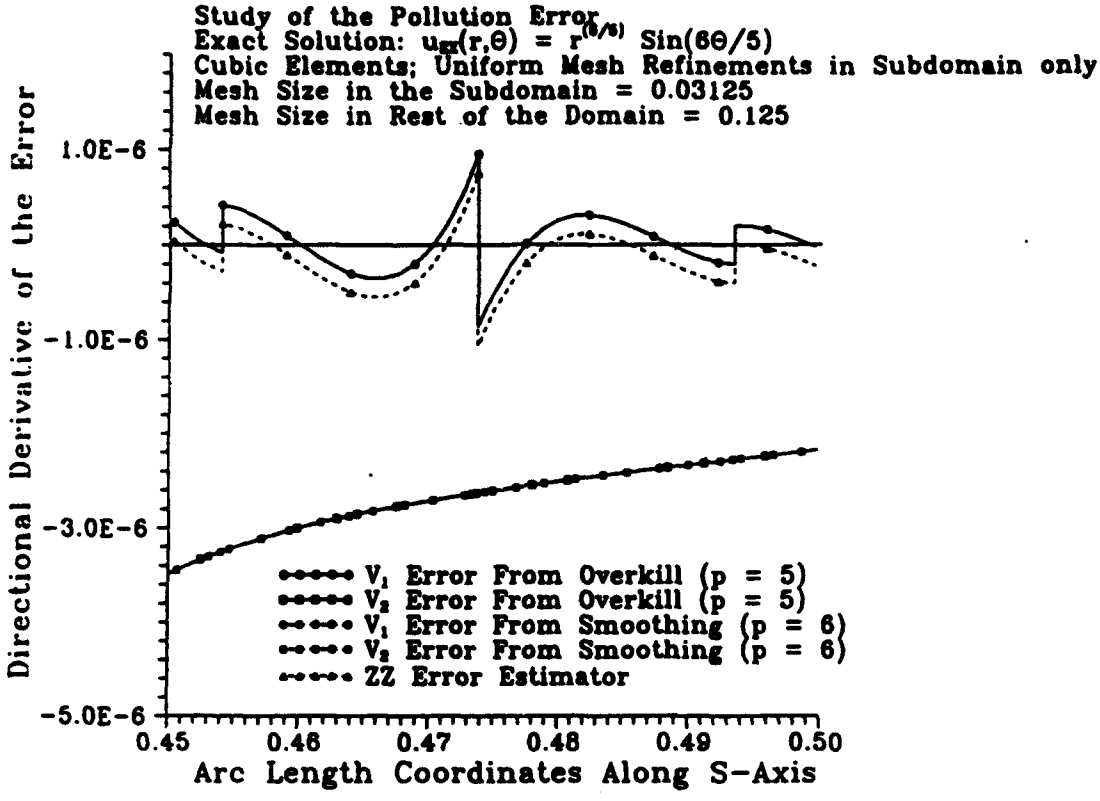

(a)

Figure 5.10. Pollution-effect for grids refined locally in an interior subdomain. Cubic elements ($p = 3$), $\alpha = \frac{6}{5}$. Directional derivatives of the V_1- and V_2-components of the error and the *ZZ* error estimator along the s-axis shown in Fig. 3.1c. (a) Uniform mesh-size in the subdomain $h = \frac{1}{32}$; (b) Uniform mesh-size in the subdomain $h = \frac{1}{128}$. Note that $\left|\frac{\partial V_2}{\partial s}\right| \gg \left|\frac{\partial V_1}{\partial s}\right|$ and $(\sigma^{ZZ} - \nabla u_h) \cdot s \approx \frac{\partial V_1}{\partial s}$, asymptotically, in the interior of the subdomain.

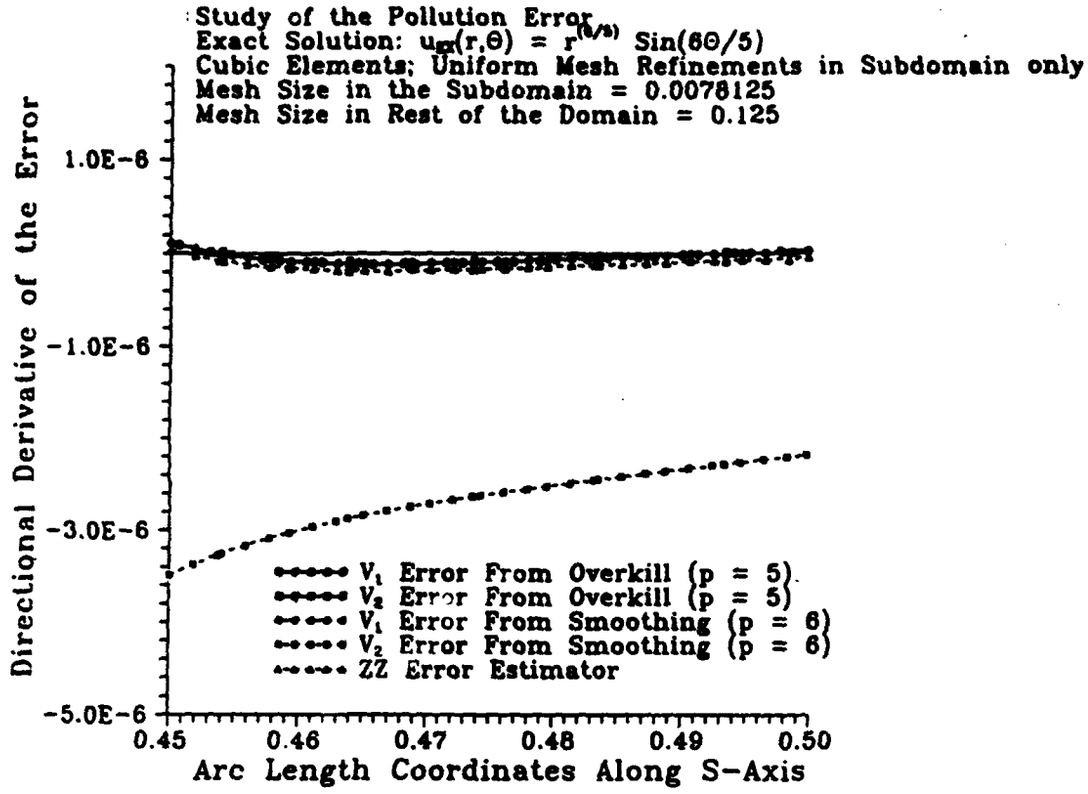

(b)

Figure 5.10. (continued)

6 Control of the pollution-effect in a subdomain

Solutions with multiple singularities occur commonly in typical 2-D geometrical idealizations of problems in solid-mechanics and heat transfer. Globally adaptive methods employ nearly-equilibrated grids in order to achieve prescribed uniform accuracies over the entire domain. In complex engineering problems one is interested to control the error and to compute with high-accuracy only in certain subdomains of interest (e.g. discussion about global/local analysis in the introduction). Here we give model computations which demonstrate that it is possible to guarantee the reliability of error estimation (and to control the error) in any interior subdomain Ω_0, by using meshes which are less refined outside the subdomain than the globally adaptive grids.

6.1 Effect of the refinement outside a subdomain on the effectivity index in the interior of the subdomain

We considered the mixed boundary-value problem for the Laplacian over the L-shaped domain and we applied boundary-conditions consistent with the exact solution $u(r,\theta) = r^{\frac{1}{3}}\sin(\frac{1}{3}\theta)$ and we considered a subdomain Ω_0 in the interior of the mesh, far from the singular point. We refined the mesh inside the subdomain uniformly, to a desired mesh-size h, and computed the relative error $\zeta_{\Omega_0} = \frac{|||e_h|||_{\Omega_0}}{|||u_h|||_{\Omega_0}}$ using a pollution-free finite element solution over the subdomain. (The pollution-free solution was computed by solving a Neumann problem over Ω_0 using data consistent with the exact solution.) The grid outside the subdomain Ω_0 was then generated using the adaptive refinement algorithm given in Section 4.5 with a tolerance $\delta = K\zeta_{\Omega_0}$, where $K \geq 1$ denotes the *weight-factor*. In the following we refer to meshes of this type as *weighted equilibrated meshes*.

6.1.1 Meshes of linear elements

In Fig. 6.1 we show the L-shaped domain meshed by a grid of linear elements ($p = 1$). The grid is uniform in the subdomain $\Omega_0 := (0.5, 0.75)^2$ with mesh-size $h = \frac{1}{32}$. The grid outside the subdomain was generated using adaptive refinement for $\zeta_{\Omega_0} = 0.44$ and $K = 1$. In Fig. 6.2 we show the graph of the effectivity index, $\kappa_{\omega_0^h}$, in the eight-element mesh-cell ω_0^h at the center of the subdomain Ω_0, plotted against the weight-factor K for different mesh-sizes in the subdomain. Note that the curve is practically invariant with respect to the mesh-size in the subdomain. Also note that the effectivity index $\kappa_{\omega_0^h}$ remains close to one up to a value of $K = 2.5$. In Fig. 6.3 we show the weighted equilibrated mesh of linear elements where the grid outside the subdomain is generated using $\zeta_{\Omega_0} = 0.44$ and $K = 2.5$.

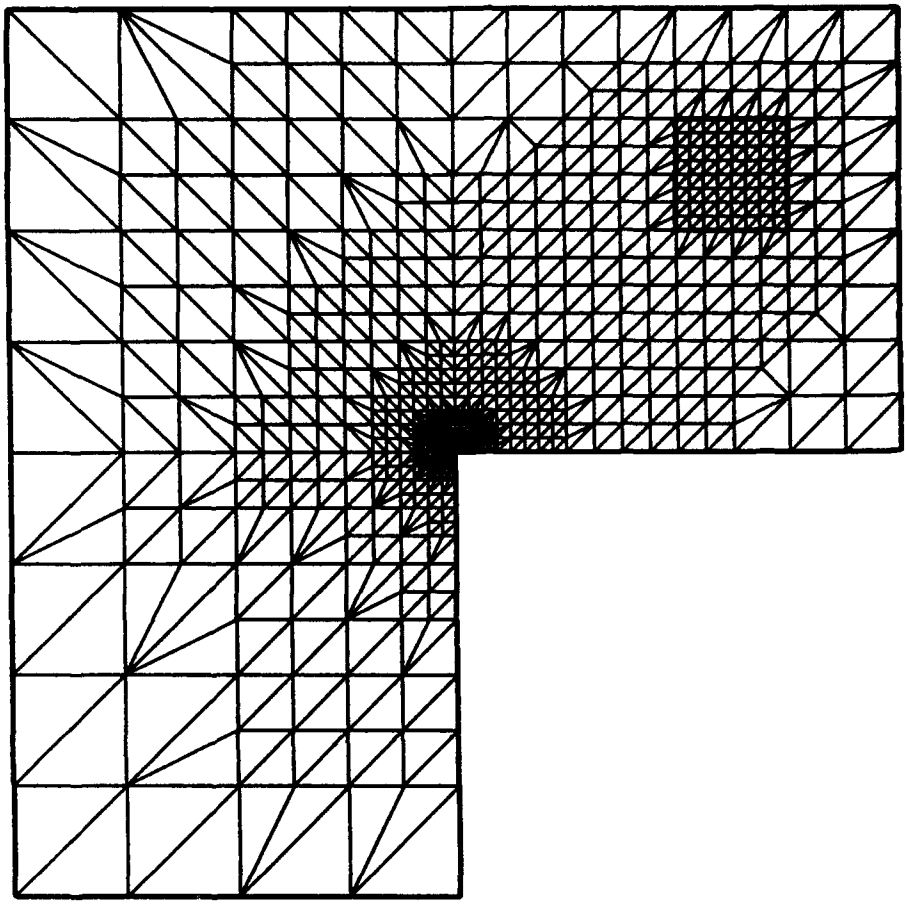

Figure 6.1. Control of the pollution-effect in a subdomain by employing weighted-equilibrated meshes. Linear elements, exact solution $u(r,\theta) = r^{\frac{1}{3}} \sin(\frac{\theta}{3})$; the mesh-size in the subdomain Ω_0 is $h = \frac{1}{32}$. The mesh outside Ω_0 is generated using adaptive refinement for $\zeta_{\Omega_0} = 0.44$ and $K = 1$. The effectivity index $\kappa_{\omega_0^h}$ in the eight-element mesh-cell ω_0^h at the center of the subdomain Ω_0 is 0.92.

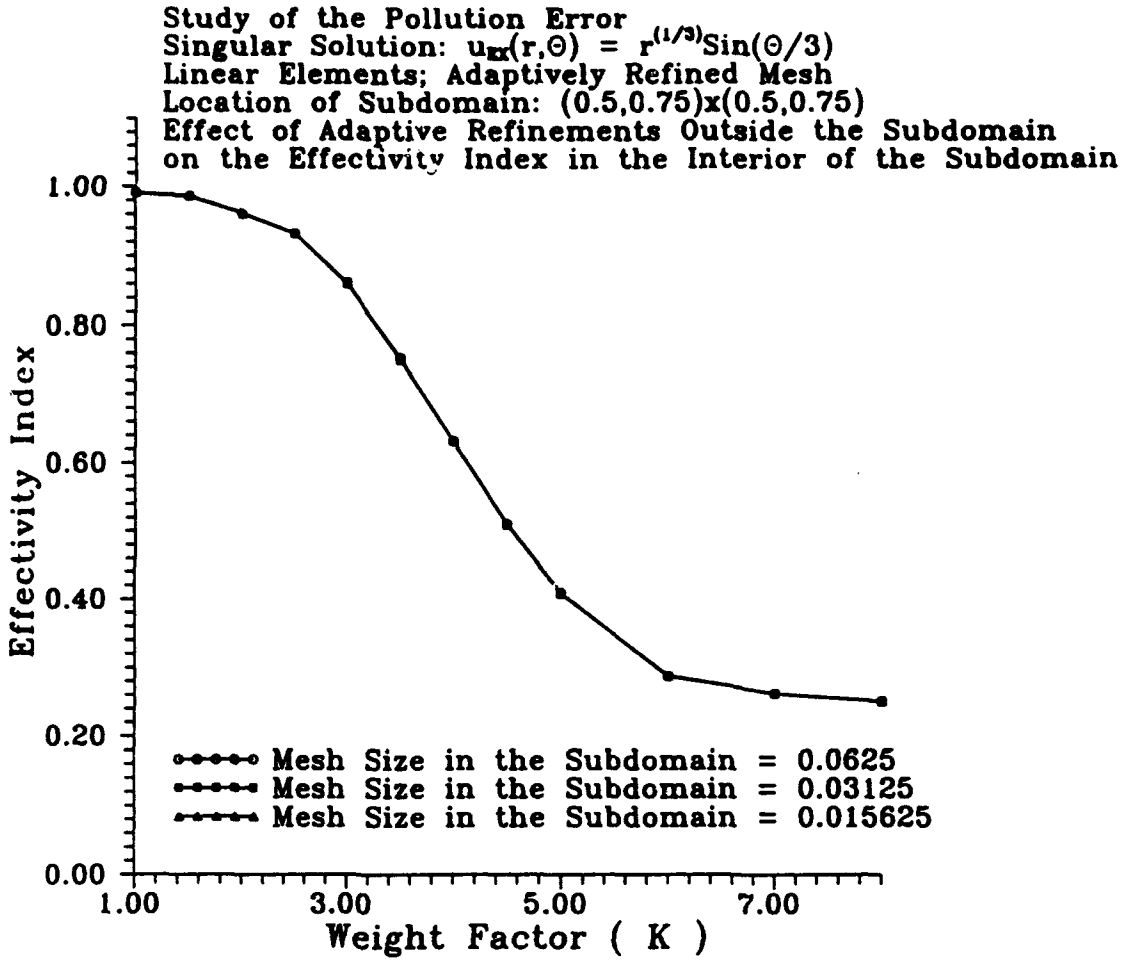

Figure 6.2. Control of the pollution-effect in a subdomain by employing weighted-equilibrated meshes. Graph of the effectivity index in the eight-element mesh-cell ω_0^h at the center of the subdomain Ω_0 plotted versus the weight factor K for different mesh-sizes in the subdomain of the mesh shown in Fig. 6.1a. Note that the curve is invariant with respect to the mesh-size in Ω_0.

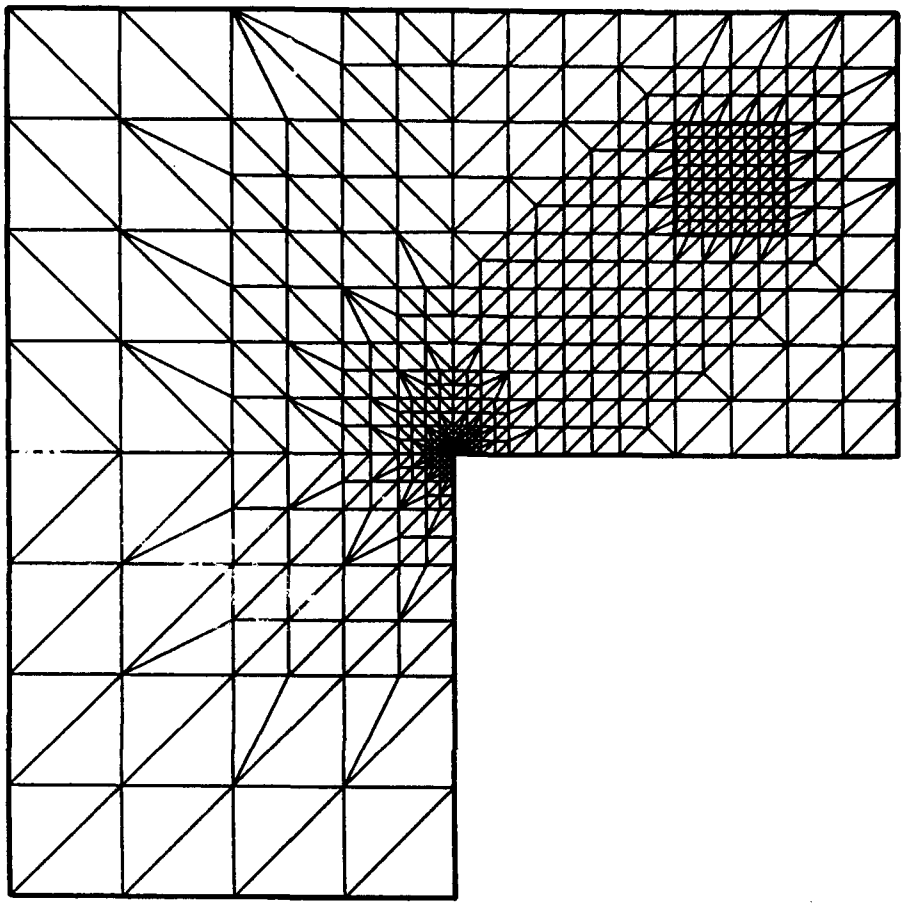

Figure 6.3. Control of the pollution-effect in a subdomain by employing weighted-equilibrated meshes. Linear elements, exact solution $u(r,\theta) = r^{\frac{1}{3}}\sin(\frac{\theta}{3})$; the mesh-size in the subdomain Ω_0 is $h = \frac{1}{32}$. The mesh outside the subdomain is generated using adaptive refinement for $\zeta_{\Omega_0} = 0.44$ and $K = 2.5$.

In Figs. 6.4a, 6.4b and 6.4c we show the directional derivatives of the V_1 - and V_2 -components of the error along the s-axis shown in Fig. 6.1a for $K = 1$, $K = 2.5$ and $K = 5$, respectively. Note that for $K = 1$, the directional derivative of the V_2 -component of the error is close to zero in the interior of the subdomain. Further, note that as the value of K is increased i.e. as the amount of refinement outside the subdomain is reduced, the directional derivative of the V_2 -component of the error becomes larger in the interior of the subdomain and for $K = 5$ the directional derivative of the V_2 -component is larger than the directional derivative of the V_1 -component in the interior of the subdomain. Also note that the error estimator practically coincides with the V_1 -component of the error in the interior of the subdomain.

6.1.2 Meshes of quadratic and cubic elements

In Fig. 6.5 we show the L-shaped domain meshed by a grid for quadratic elements ($p = 2$). The grid is uniform in the subdomain $\Omega_0 = (0.5, 0.75)^2$ with mesh-size $h = \frac{1}{32}$. The grid outside the subdomain was generated using adaptive refinement for $\zeta_{\Omega_0} = 0.07$ and $K = 1$. In Fig. 6.6 we show the mesh where the grid outside the subdomain Ω_0 was generated using $\zeta_{\Omega_0} = 0.01$ and $K = 1$.

In Fig. 6.7 we give the graph of the effectivity index, $\kappa_{\omega_0^h}$, in the mesh-cell ω_0^h at the center of the subdomain $\Omega_0 := (0.5, 0.75)^2$ for $p = 1$, 2 and 3. Note that for quadratic elements the effectivity index is close to one up to a value of $K = 3$ and for cubic elements the value of the effectivity index is close to one up to a value of $K = 3.5$. In Fig. 6.8 we show the weighted-equilibrated mesh of quadratic elements which is generated using $\zeta_{\Omega_0} = 0.07$ and $K = 3$ outside the subdomain and in Fig. 6.9 we show the weighted-equilibrated mesh of cubic elements generated using adaptive refinement for $\zeta_{\Omega_0} = 0.02$ and $K = 3.5$ outside the subdomain. Hence we observe that as the polynomial degree p of the elements is increased, the pollution-effect in the interior of the subdomain is controlled for a bigger range of values of the weight-factor K.

6.2 Factors affecting the permissible range of the weight-factor K

Here we examine the factors which affect the range of the weight-factor K for which the pollution-effect in the interior of the subdomain is controlled. We will say that the pollution-effect in an interior subdomain is controlled if $\kappa_{\omega_0^h} > 0.85$ (where ω_0^h denote interior mesh-cells in the subdomain). We will call the range of K, $\mathcal{K} = [1, K_{\max}]$, for which $\kappa_{\omega_0^h} > 0.85$, the *permissible range of* of K. For example, in the numerical examples given in Section 6.1, $K_{\max} = 2.5$, 3 and 3.5 for linear, quadratic and cubic elements, respectively.

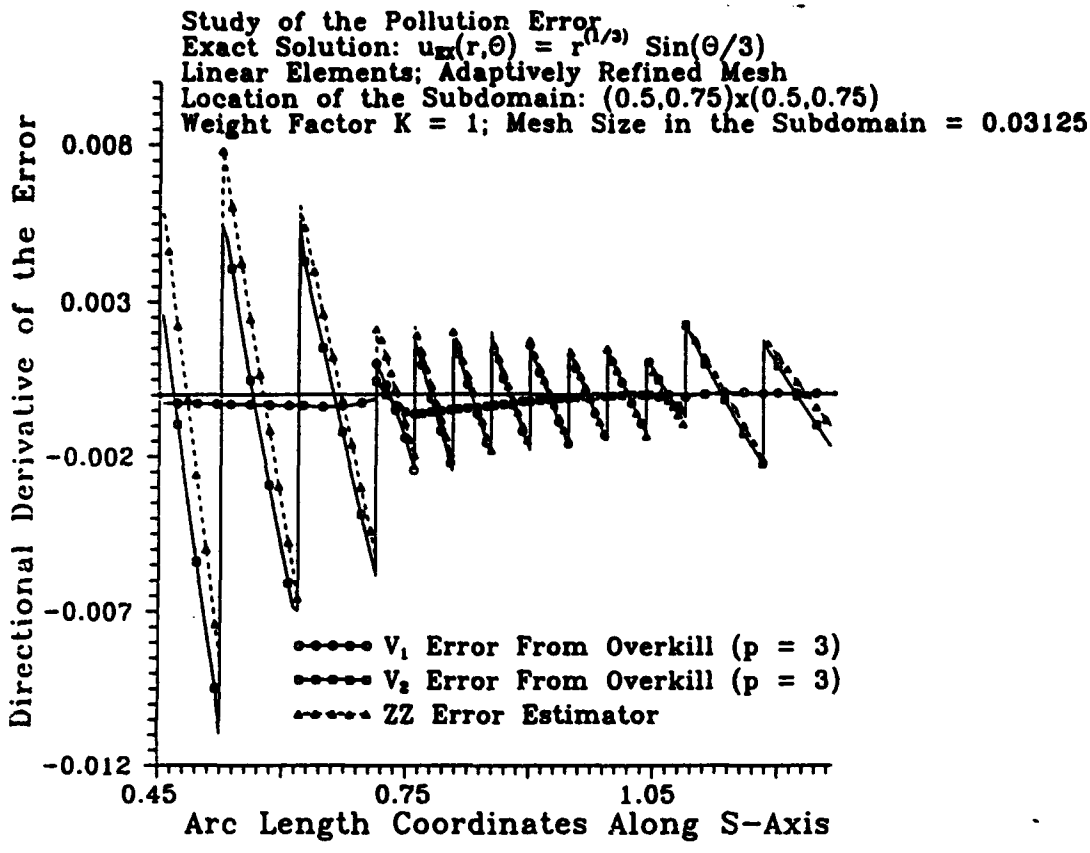

(a)

Figure 6.4. Control of the pollution-effect in a subdomain by employing weighted-equilibrated meshes. Linear elements, exact solution $u(r,\theta) = r^{\frac{1}{3}} \sin(\frac{\theta}{3})$; the mesh-size in the subdomain Ω_0 is $h = \frac{1}{32}$. Directional derivatives of the V_1 - and V_2 -components of the error and the ZZ estimator along the s axis for adaptive meshes generated using (a) $K = 1$ (b) $K = 2.5$ (c) $K = 5$. Note that for $K = 1$ and $K = 2.5$, $\left|\frac{\partial V_2}{\partial s}\right| \ll \left|\frac{\partial V_1}{\partial s}\right|$ but for $K = 5$, $\left|\frac{\partial V_2}{\partial s}\right| \gg \left|\frac{\partial V_1}{\partial s}\right|$, in the interior of the subdomain.

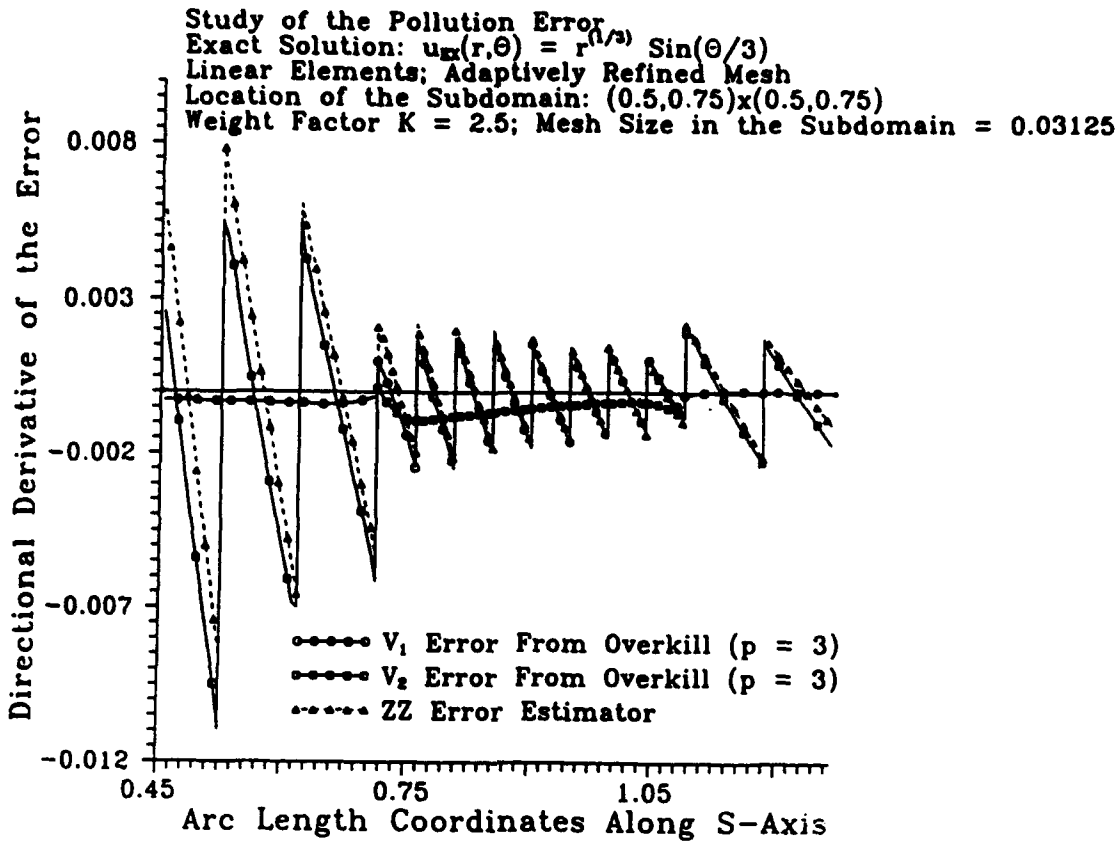

(b)

Figure 6.4. (continued)

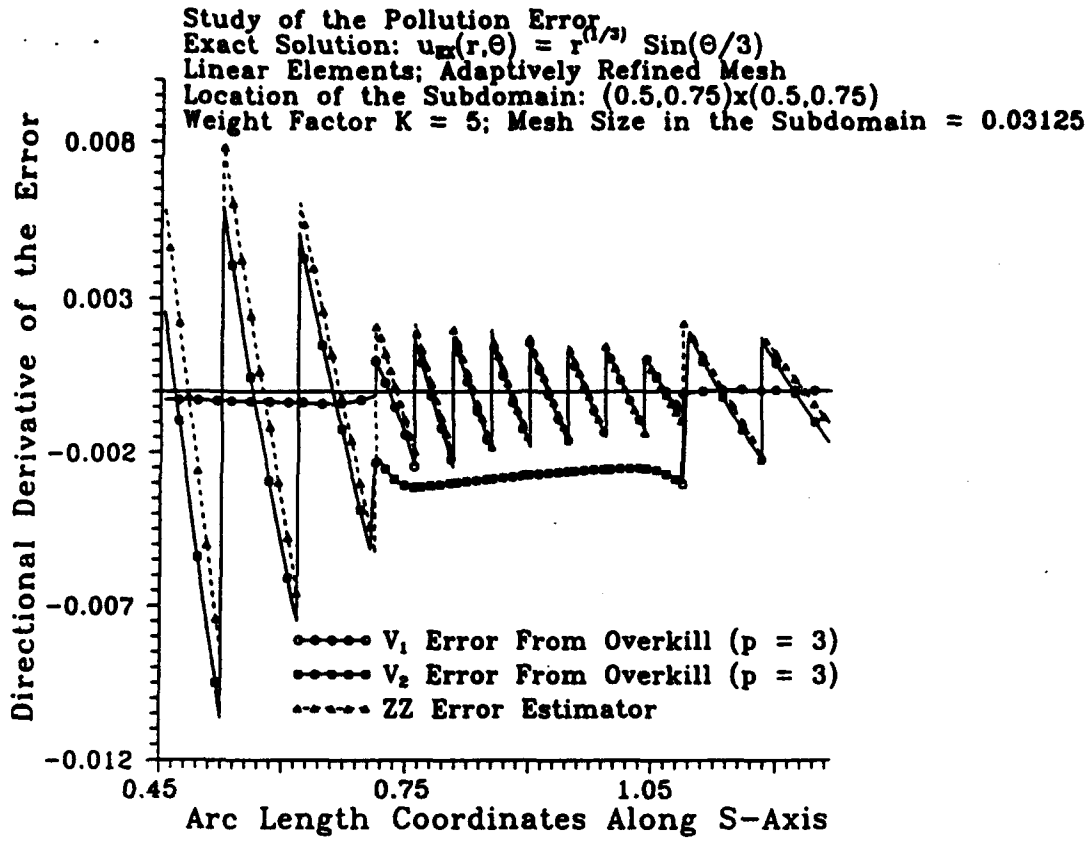

(c)

Figure 6.4. (continued)

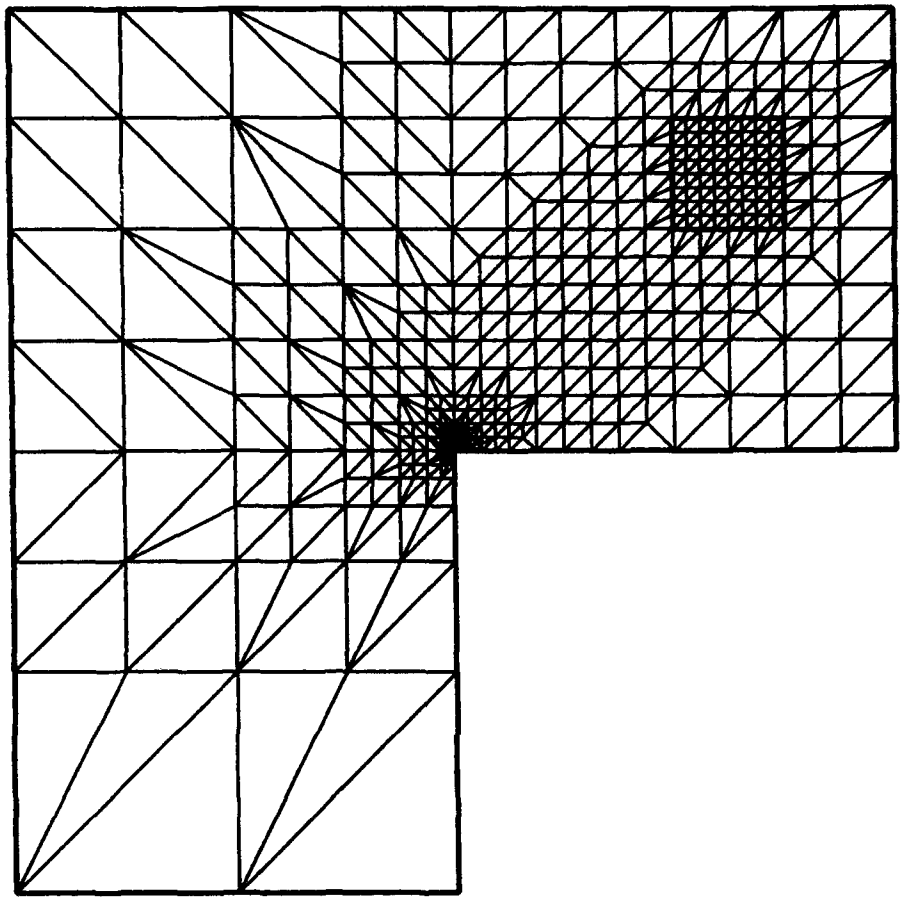

Figure 6.5. Control of the pollution-effect in a subdomain by employing weighted-equilibrated meshes. Quadratic elements, exact solution $u(r,\theta) = r^{\frac{1}{3}} \sin(\frac{\theta}{3})$; the mesh-size in the subdomain Ω_0 is $h = \frac{1}{32}$. The mesh outside Ω_0 is generated using adaptive refinement for $\zeta_{\Omega_0} = 0.07$ and $K = 1$. The effectivity index $\kappa_{\omega_0^h}$ in the eight-element mesh-cell ω_0^h at the center of the subdomain Ω_0 is 0.97.

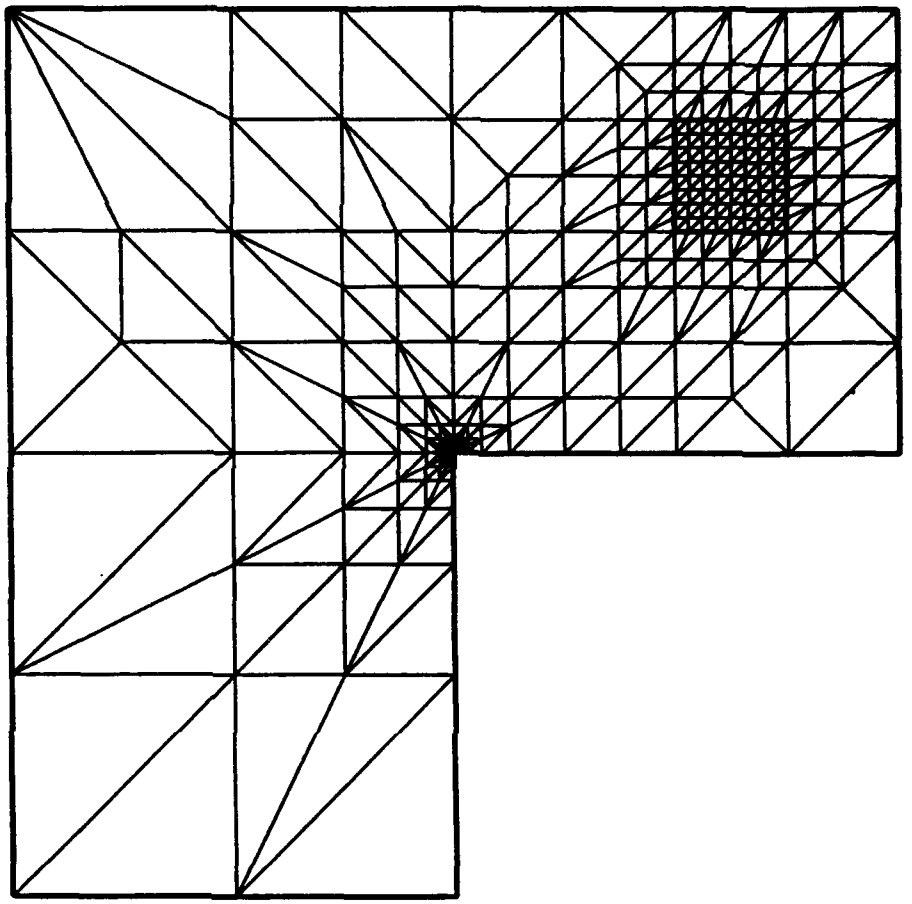

Figure 6.6. Control of the pollution-effect in a subdomain by employing weighted-equilibrated meshes. Cubic elements, exact solution $u(r,\theta) = r^{\frac{1}{3}} \sin(\frac{\theta}{3})$; the mesh-size in the subdomain Ω_0 is $h = \frac{1}{32}$. The mesh outside Ω_0 is generated using adaptive refinement for $\zeta_{\Omega_0} = 0.01$ and $K = 1$. The effectivity index $\kappa_{\omega_0^h}$ in the eight-element mesh-cell ω_0^h at the center of the subdomain Ω_0 is 0.97.

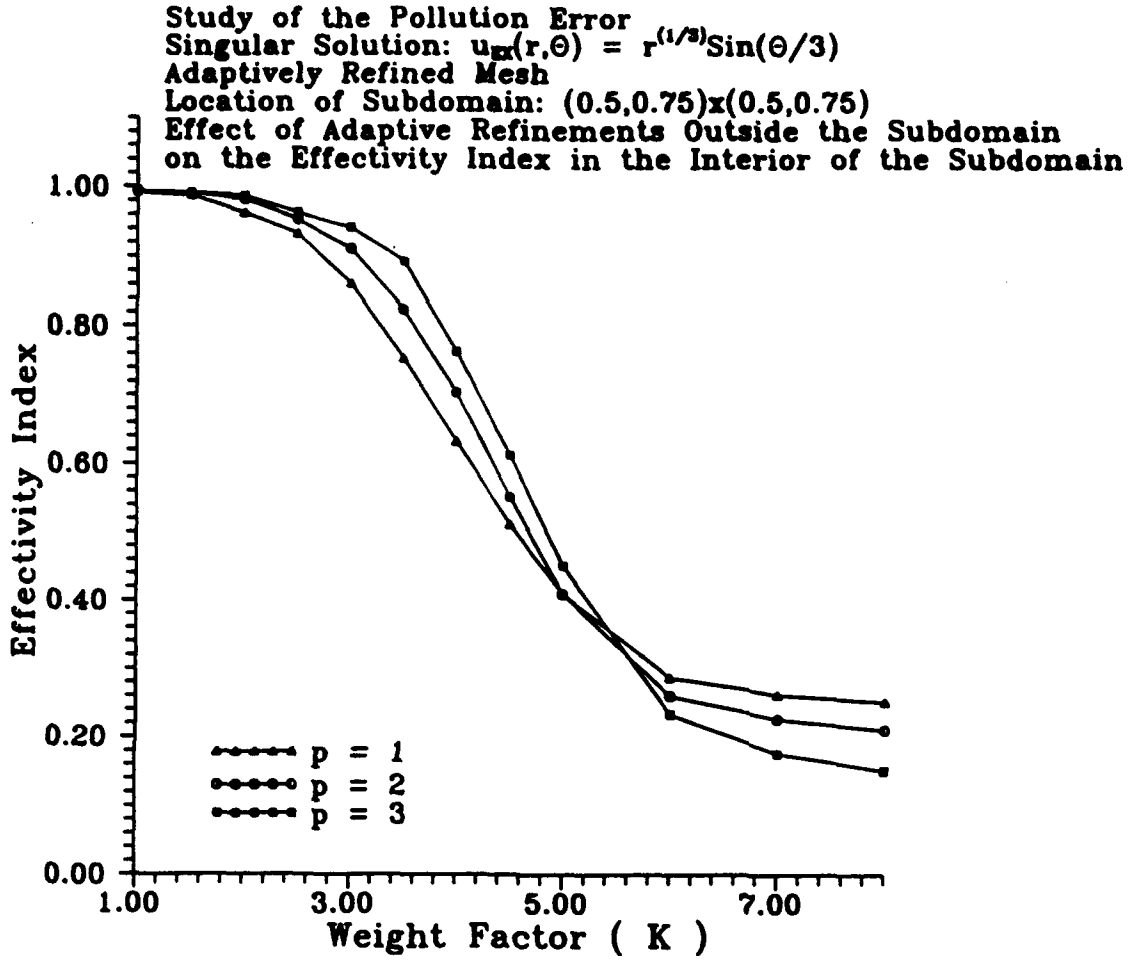

Figure 6.7. Control of the pollution-effect in a subdomain by employing weighted-equilibrated meshes. Exact solution $u(r,\theta) = r^{\frac{1}{3}}\sin(\frac{\theta}{3})$; the mesh-size in the subdomain Ω_0 is $h = \frac{1}{32}$. Comparison of the effectivity index vs. K curves for $p = 1, 2, 3$. Note that as the polynomial degree p of the elements is increased, it is possible to control the pollution-effect in the subdomain for larger values of the weight factor K.

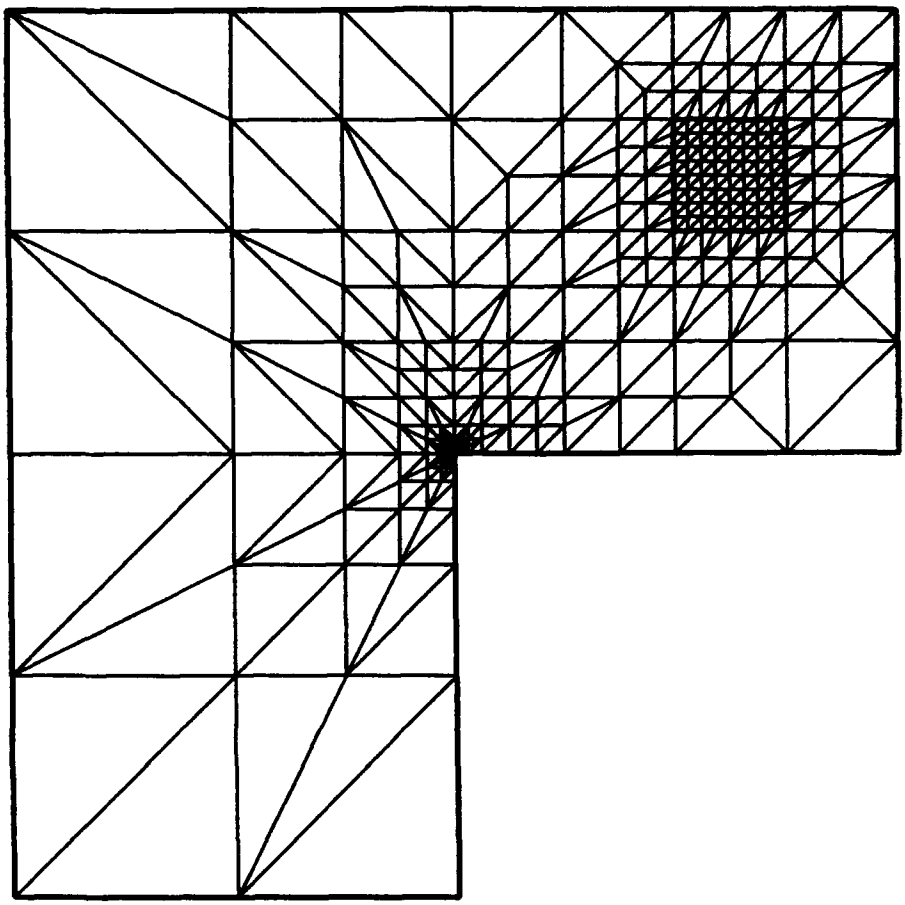

Figure 6.8. Control of the pollution-effect in a subdomain by employing weighted-equilibrated meshes. Quadratic elements, exact solution $u(r,\theta) = r^{\frac{1}{3}} \sin(\frac{\theta}{3})$; the mesh-size in the subdomain Ω_0 is $h = \frac{1}{32}$. The mesh outside Ω_0 is generated using adaptive refinement for $\zeta_{\Omega_0} = 0.07$ and $K = 3$. The effectivity index $\kappa_{\omega_0^h}$ in the eight-element mesh-cell ω_0^h at the center of the subdomain Ω_0 is 0.93.

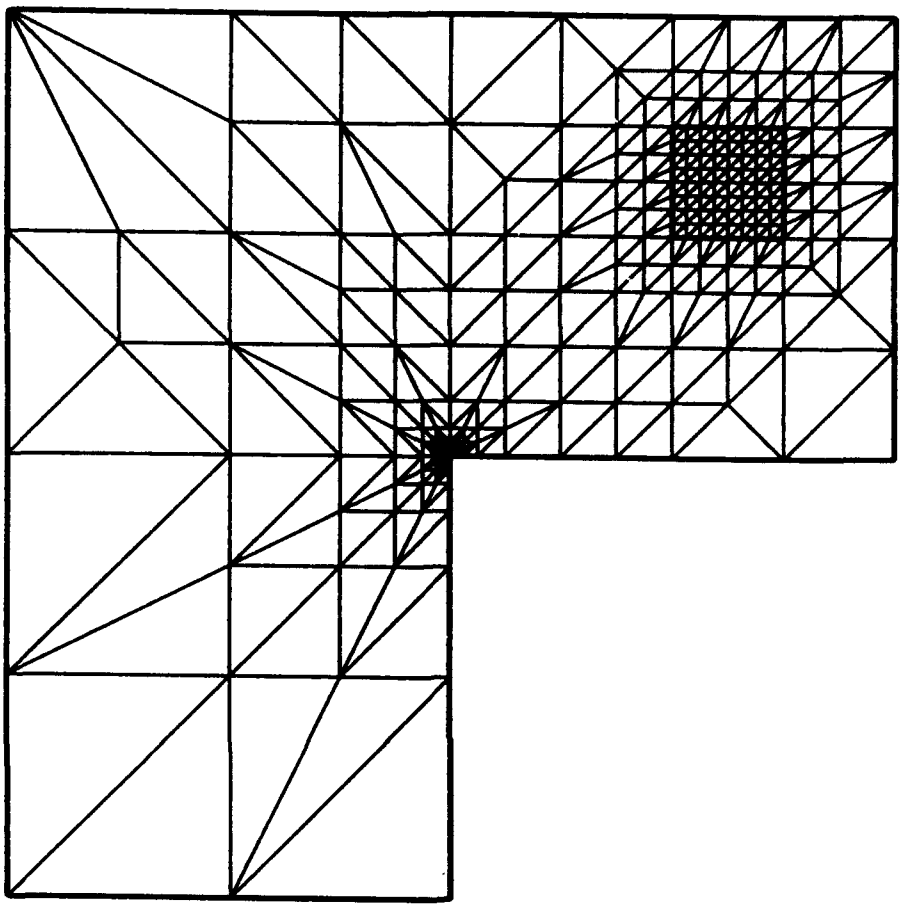

Figure 6.9. Control of the pollution-effect in a subdomain by employing weighted-equilibrated meshes. Cubic elements, exact solution $u(r,\theta) = r^{\frac{1}{3}} \sin(\frac{\theta}{3})$; the mesh-size in the subdomain Ω_0 is $h = \frac{1}{32}$. The mesh outside Ω_0 is generated using adaptive refinement for $\zeta_{\Omega_0} = 0.01$ and $K = 3.5$. The effectivity index $\kappa_{\omega_0^h}$ in the eight-element mesh-cell ω_0^h at the center of the subdomain Ω_0 is 0.93.

a. Effect of the distance of the subdomain Ω_0 from the singularity

We considered the L-shaped domain with a uniform-mesh subdomain $\Omega_0 := (0.25, 0.5)^2$ closer to the singular point than the subdomain in the examples given in Section 6.1. In Fig. 6.10 we show the mesh for linear elements ($p = 1$) for which the mesh-size in the subdomain is $h = \frac{1}{32}$ and the mesh outside the subdomain was generated using adaptive refinement for $\zeta_{\Omega_0} = 0.25$ and $K = 1$. In Fig. 6.11 we show the graph of the effectivity index, $\kappa_{\omega_0^h}$, in the mesh-cell ω_0^h at the center of the subdomain, plotted against the weight-factor K. Note that the effectivity index $\kappa_{\omega_0^h}$ remains close to one up to a value of $K = 2$ and then drops to small values faster when compared with the graph of Fig. 6.7. In Fig. 6.12 we show the weighted-equilibrated mesh of linear elements where the grid outside the subdomain is generated using $\zeta = 0.25$ and $K = 2$. Hence, we note that as the distance of the subdomain Ω_0 from the singular point increases, the permissible range of the weight-factor K increases in size and the pollution-effect in the subdomain can be controlled by employing coarser meshes outside the subdomain.

b. Effect of the strength of the singularity: Value of the exponent, α

We considered singularities with two different exponents $\left(\alpha = \frac{1}{3} \text{ and } \alpha = \frac{2}{3}\right)$ for quadratic elements and plotted the graph of the effectivity index $\kappa_{\omega_0^h}$ for the mesh-cell ω_0^h at the center of the subdomain $\Omega_0 := (0.5, 0.75)^2$ vs. the weight-factor K. In Fig. 6.13 we show the comparison of the effectivity index vs K curves for $\alpha = \frac{1}{3}$ and $\alpha = \frac{2}{3}$. From the graph, we note that $K_{\max} = 3$ for $\alpha = \frac{1}{3}$, while $K_{\max} = 3.5$ for $\alpha = \frac{2}{3}$. Hence we note that for $\alpha = \frac{2}{3}$ the permissible range of the weight-factor K increases in size and the values of the effectivity index are higher than the values of the effectivity index for $\alpha = \frac{1}{3}$, for all values of the weight-factor K.

c. Effect of the strength of the singularity: Value of the stress intensity factor, A

We considered the exact solution $u(r, \theta) = Ar^{\frac{1}{3}} \sin(\frac{1}{3}\theta)$ for $A = 0.02$, $A = 0.1$, $A = 0.5$, $A = 1$, $A = 10$ and $A = 50$ and linear elements. We plotted the graph of the effectivity index $\kappa_{\omega_0^h}$ for the mesh cell ω_0^h at the center of the subdomain $\Omega_0 := (0.5, 0.75) \times (0{,}5, 0.75)$ vs. the weight-factor K. In Fig. 6.14 we show the comparison of the graphs for $A = 0.02$, 0.1, 0.5, 1, 10 and 50. Note that as the value of stress-intensity factor A is increased, the value of the effectivity index drops for the same value of K. Hence we observe that for higher values of the stress intensity factor A, the permissible range of the weight-factor K decreases and more refinement is needed outside the subdomain in order to control the pollution-effect in the interior of the subdomain.

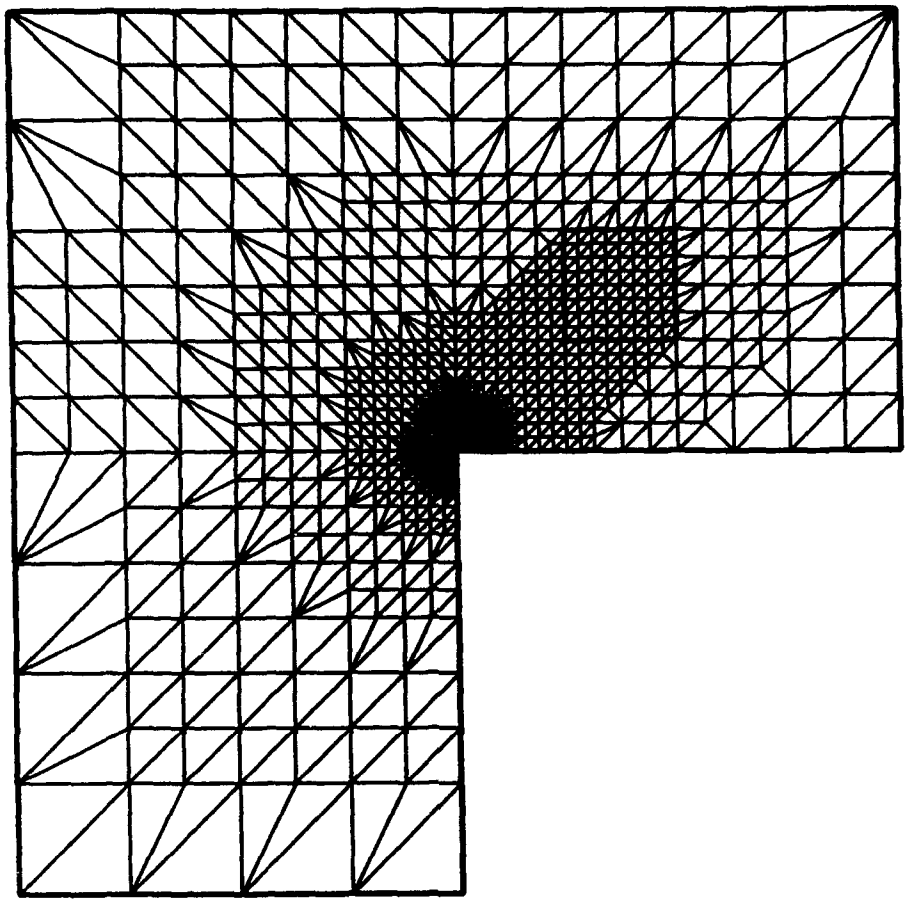

Figure 6.10. Control of the pollution-effect in a subdomain by employing weighted-equilibrated meshes. Effect of the distance of the subdomain from the singularity on the amount of refinement needed outside the subdomain in order to control the pollution-effect in Ω_0. Linear elements, exact solution $u(r,\theta) = r^{\frac{1}{3}} \sin(\frac{\theta}{3})$, location of the subdomain $\Omega_0 : (0.25, 0.5)^2$, mesh-size in the subdomain $h = \frac{1}{32}$. The mesh outside Ω_0 is generated using adaptive refinement for $\zeta_{\Omega_0} = 0.25$ and $K = 1$.

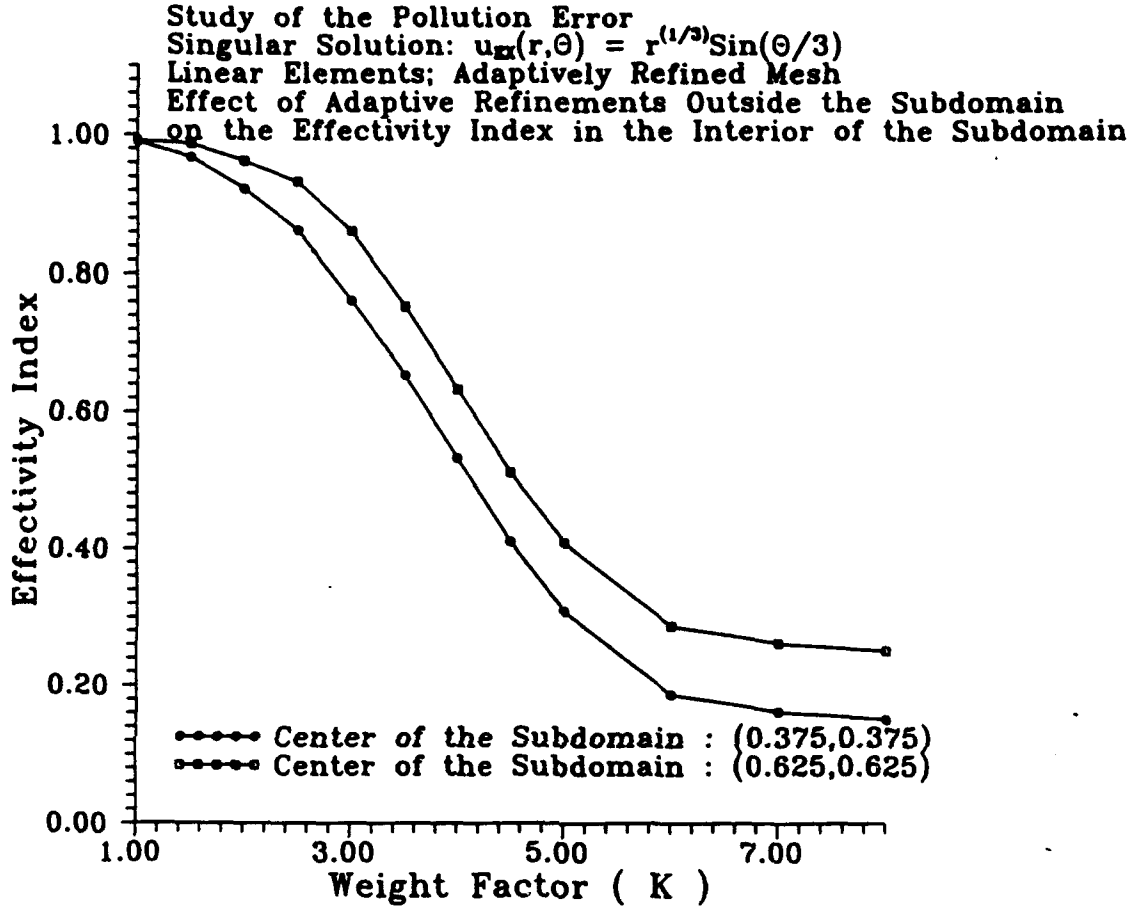

Figure 6.11. Control of the pollution-effect in a subdomain by employing weighted-equilibrated meshes. Effect of the distance of the subdomain Ω_0 from the singularity on the amount of refinement needed outside the subdomain in order to control the pollution-effect in Ω_0. Linear elements, exact solution $u(r,\theta) = r^{\frac{1}{3}}\sin(\frac{\theta}{3})$, location of the subdomain Ω_0 : $(0.25,0.5)^2$, mesh-size in the subdomain $h = \frac{1}{32}$. The mesh outside the subdomain is generated using adaptive refinement for $\zeta_{\Omega_0} = 0.25$ and $K = 1$. Note that as the distance of the subdomain from the singular point increases, it is possible to control the pollution-effect in Ω_0 for larger values of the weight-factor K.

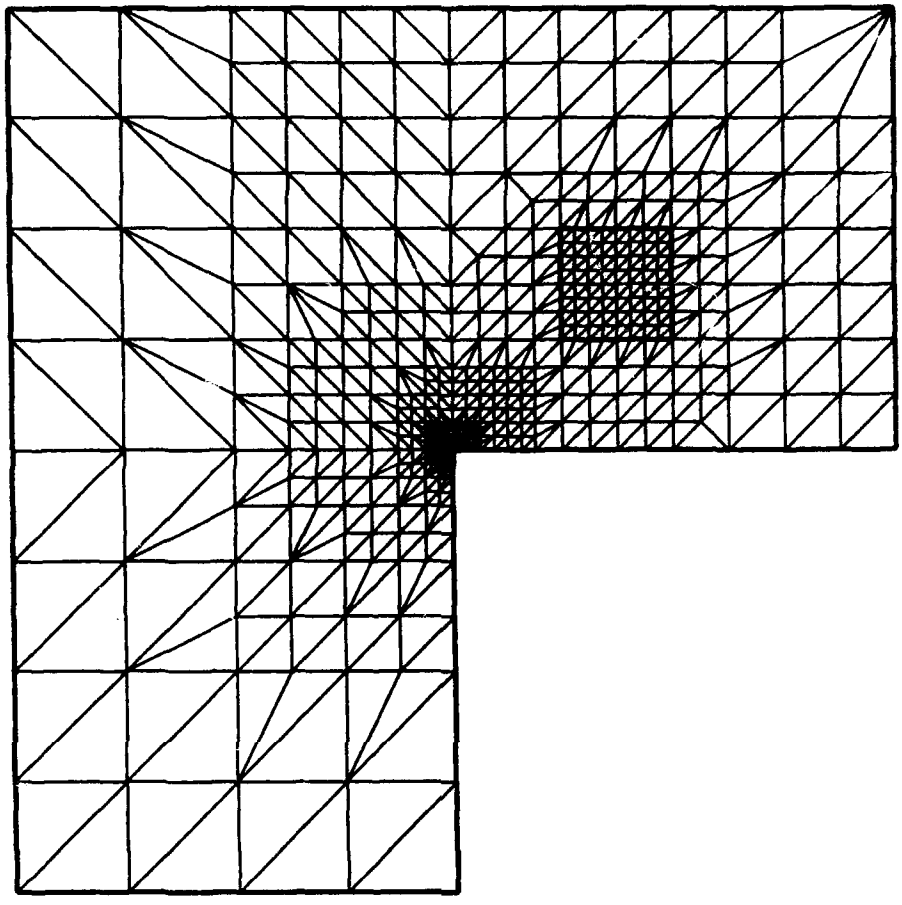

Figure 6.12. Control of the pollution-effect in a subdomain by employing weighted-equilibrated meshes. Effect of the distance of the subdomain from the singularity on the amount of refinement needed outside the subdomain in order to control the pollution-effect in the interior of the subdomain. Linear elements, exact solution $u(r,\theta) = r^{\frac{1}{3}} \sin(\frac{\theta}{3})$, location of the subdomain Ω_0 : $(0.25, 0.5)^2$, mesh-size in the subdomain $h = \frac{1}{32}$. The mesh outside the subdomain is generated using adaptive refinement for $\zeta_{\Omega_0} = 0.25$ and $K = 2$.

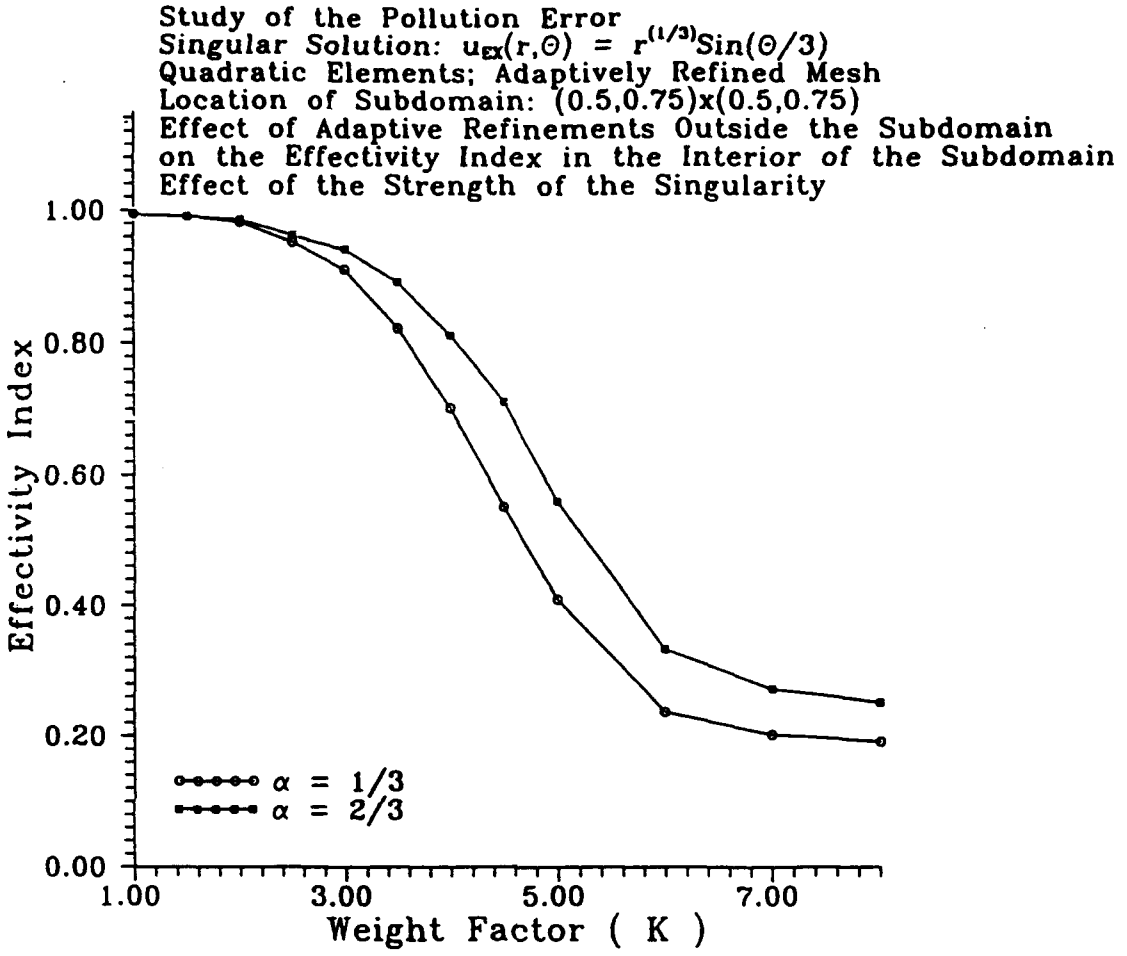

Figure 6.13. Control of the pollution-effect in a subdomain by employing weighted-equilibrated meshes. Effect of the exponent α on the amount of refinement needed outside outside the subdomain in order to control the pollution-effect in the interior of the subdomain. Quadratic elements, exact solution $u(r,\theta) = r^{\frac{1}{3}} \sin \frac{\theta}{3}$, mesh-size in the subdomain $\Omega_0 := (0.5,0.75)^2$, $h = \frac{1}{32}$. Note that as the value of the exponent increases (i.e. the solution becomes smoother), it is possible to control the pollution-effect in Ω_0 for larger values of the weight-factor K.

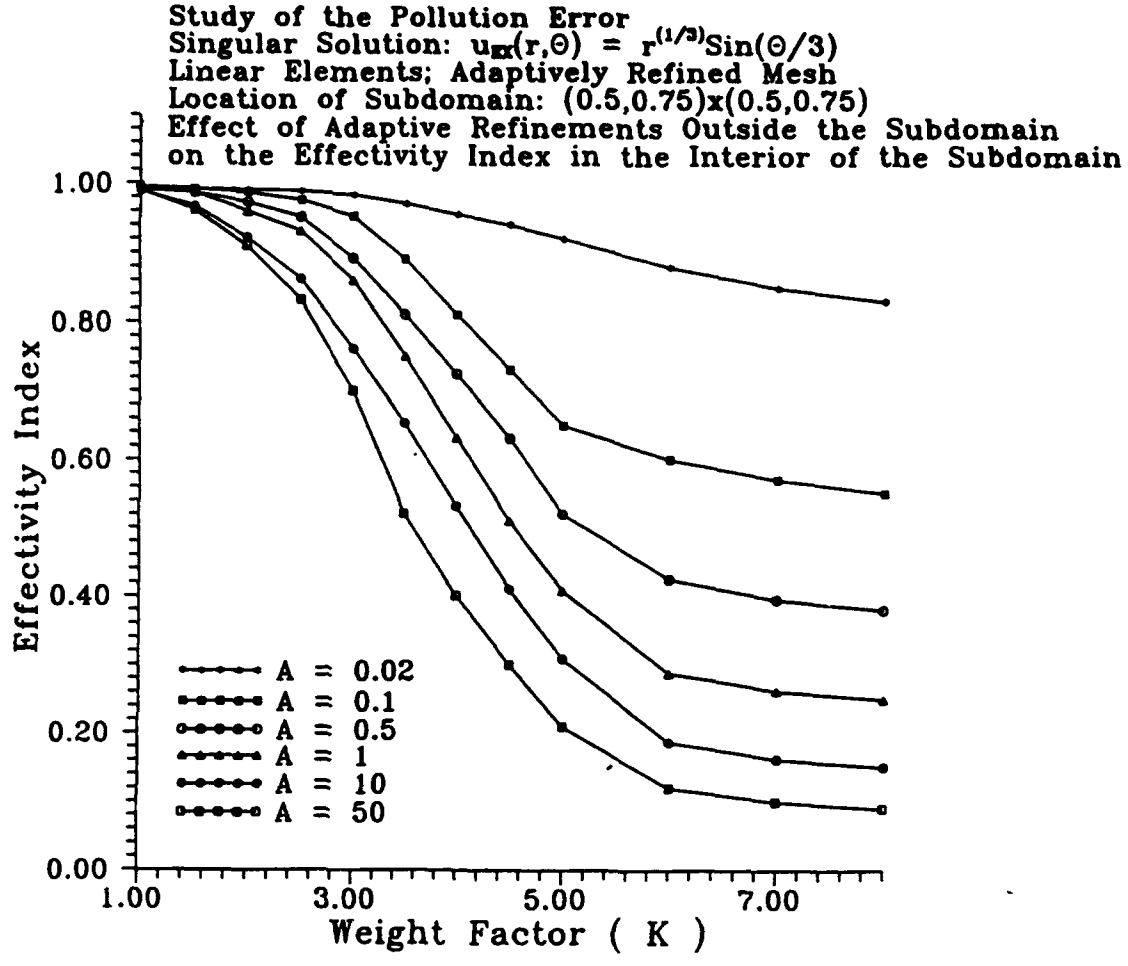

Figure 6.14. Control of the pollution-effect in a subdomain by employing weighted-equilibrated meshes. Effect of the stress-intensity factor A on the amount of refinement needed outside the subdomain in order to control the pollution-effect in the interior of the subdomain. Linear elements, exact solution $u(r,\theta) = r^{\frac{1}{3}} \sin \frac{\theta}{3}$, location of the subdomain $\Omega_0 := (0.5, 0.75)^2$, mesh-size in the subdomain $h = \frac{1}{32}$. Note that as A is decreases, it is possible to control the pollution-effect in Ω_0 for larger values of the weight-factor K.

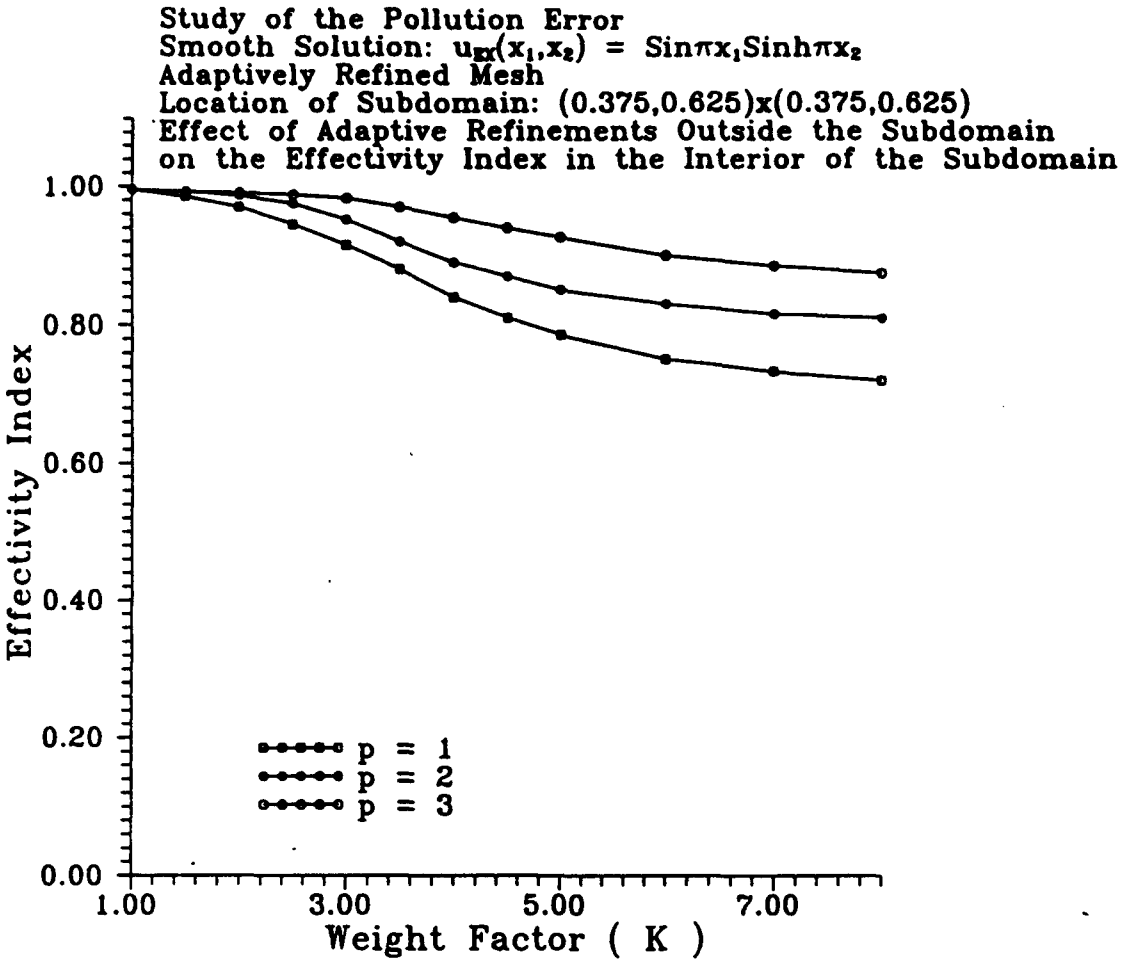

Figure 6.15. Control of the pollution-effect in a subdomain by employing weighted-equilibrated meshes. Smooth solution $u(x_1, x_2) = \sin \pi x_1 \sinh \pi x_2$, unit square domain shown in Fig. 5.2. Comparison of the effectivity index vs. K curves for $p = 1, 2, 3$. Note that as p increases, it is possible to control the pollution-effect in Ω_0 practically for all values of the weight-factor K.

d. Effect of the smoothness of the solution

We also considered the smooth solution $u(x_1, x_2) = \sin \pi x_1 \sinh \pi x_2$ in the square-domain $\Omega = (0,1)^2$ and plotted the graph of the effectivity index $\kappa_{\omega_0^h}$, for the mesh cell ω_0^h at the center of the subdomain $\Omega_0 := (0.375, 0.625)^2$ as shown in Fig. 5.2, vs. the weight factor K. In Fig. 6.15 we show the graphs for $p = 1, 2$ and 3. Note that the values of the effectivity index are greater than 0.8 for the all values of K.

6.3 Summary of the results for the control of the pollution-effect in a subdomain

In summary, we observe that

(i). It is possible to control the pollution-effect in an interior subdomain by using weighted-equilibrated grids which are less refined outside the subdomain than globally nearly equilibrated grids.

(ii). The amount of refinement outside the subdomain needed to control the pollution-effect in the subdomain depends on the strength of the singularities, the distance of the subdomain Ω_0 from the singular points, the mesh-size inside the subdomain and the polynomial degree p of the elements.

7 Summary

In this work we presented a numerical study of the pollution-error in the h-version of the finite-element method. We studied the effect of the pollution error on the local quality of error estimation for various classes of meshes and solutions used in practical engineering computations. In particular, we considered harmonic solutions with algebraic singularities of the type r^α and studied the pollution-effect for uniform meshes, globally adaptive (nearly equilibrated) meshes, locally refined meshes and weighted-equilibrated meshes.

The major conclusions of this study are:

1. When the mesh is globally adaptive (nearly equilibrated in the energy-norm) the pollution-effect is negligible and, for all practical purposes, we can guarantee the reliability of error estimation for all interior mesh-cells.

2. If the mesh is not nearly equilibrated in the energy-norm, the pollution-effect may be significant.

3. For uniform meshes, the pollution-effect is significant asymptotically when $2\alpha < p$, the polynomial degree of the elements. However when $2\alpha > p$, the pollution is negligible.

4. The accuracy of the finite element solution in a subdomain depends upon the relationship between the mesh inside the subdomain and the mesh outside the subdomain and the smoothness of the exact solution.

5. It is possible to control the pollution effect in a subdomain by employing weighted-equilibrated grids which are less refined outside the subdomain than the globally nearly equilibrated grids.

6. The reliability of local error estimation in an interior subdomain can be guaranteed only when the pollution-effect in the subdomain is negligible. If there is strong pollution, severe underestimation may occur and in general nothing can be said about the reliability of the local results of a-posteriori error estimation.

References

1. I. Babuška, Courant element: Before and after, Technical Note BN-1154, Institute for Physical Science and Technology, University of Maryland, October 1993.

2. I. Babuška, The problem of modeling the elastomechanics in engineering, Comput. Methods Appl. Mech. Engrg., 82 (1990) 155-182.

3. I. Babuška, B.A. Szabó and R.L. Actis, Hierarchic models for laminated composites, Inter. J. Numer. Methods Engrg., 33 (1992) 503-535.

4. I. Babuška and L. Li, The problem of plate modeling: Theoretical and computational results, Comput. Methods Appl. Mech. Engrg., 100 (1992) 249-293.

5. I. Babuška and L. Li, The $h-p$ version of the finite-element method in the plate modelling problem, Commun. Appl. Numer. Methods, 8 (1992) 17-26.

6. J.B. Ransom and N.F. Knight Jr., Global/Local analysis for composite panels, Computers & Structures, 37 (1990) 375-395.

7. J. Fish, N. Fares and A. Nath, Michromechanical elastic crack-tip stresses in a fibrous composite, Internat. J. Fracture 60 (1993) 135-146.

8. I. Babuška and W.C. Rheinboldt, Error estimates for adaptive finite element computations, SIAM J. Numer. Anal. 15 (1978) 736-754.

9. I. Babuška and W.C. Rheinboldt, A-posteriori error estimates for the finite element method, Internat. J. Numer. Methods Engrg. 12 (1978) 1597-1615.

10. I. Babuška and W.C. Rheinboldt, Adaptive approaches and reliability estimations in finite element analysis, Comput. Methods Appl. Engrg. 17, (1979) 519-540.

11. I. Babuška and W.C. Rheinboldt, Reliable error estimation and mesh adaptation for the finite element method, in: Computational Methods in Nonlinear Mechanics, edited by J.T. Oden, North Holland, Amsterdam (1980) 67-108.

12. I. Babuška and W.C. Rheinboldt, A posteriori error analysis of finite element solutions for one-dimensional problems, SIAM J. Numer. Anal. 8 (1981) 565-589.

13. I. Babuška and A. Miller, A-posteriori error estimates and adaptive techniques for the finite element method, Technical Note BN-968, Institute for Physical Science and Technology, University of Maryland (1981).

14. P. Ladeveze and D. Leguillon, Error estimate procedure in the finite element method and applications, SIAM J. Numer. Anal. 20 (1983) 485-509.

15. R.E. Bank and A. Weiser, Some a posteriori error estimators for elliptic partial differential equations, Math. Comp. 44 (1985) 283-301.

16. I. Babuška and A. Miller, A feedback finite element method with a posteriori error estimation: Part I. The finite element method and some basic properties of the a posteriori error estimator, Comput. Methods Appl. Mech. Engrg. 61, (1987) 1-40.

17. I. Babuška and D. Yu, Asymptotically exact a posteriori error estimator for biquadratic elements, Finite Elements in Analysis and Design 3, (1987) 341-354.

18. K. Eriksson and C. Johnson, An adaptive finite element method for linear elliptic problems, Math. Comp. 50 (1988) 361-383.

19. J.T. Oden, L. Demkowicz, W. Rachowicz and T.A. Westermann, Toward a universal h-p adaptive finite element strategy: Part 2, A Posteriori Error Estimates, Comput. Methods Appl. Mech. Engrg. 77 (1989) 113-180.

20. T.A. Westermann, A Posteriori Estimation of Errors in hp finite element methods for linear elliptic boundary value problems, M.Sc. Thesis, The University of Texas at Austin (1989).

21. R. Verfürth, A posteriori error estimators for the Stokes equation, Numer. Math. 55, (1989) 309-325.

22. J. Baranger and H. El-Amri, Estimateurs a posteriori d' erreur pour le calcul adaptatif d' ecoulements quasi-newtoniens, RAIRO Math. Model. Numer. Anal. 25 (1), (1991) 31-48.

23. R. Verfürth, A posteriori error estimation and adaptive mesh refinement techniques, preprint, (1992).

24. P. Ladeveze, J.P. Pelle and P. Rougeot, Error estimation and mesh optimization for classical finite elements, Engineering Computations 9, (1991) 69-80.

25. P. Ladeveze, P. Marin, J.P. Pelle and G.L. Gastine, Accuracy and optimal meshes in finite element computation for nearly compressible material, Comput. Methods Appl. Mech. Engrg. 94, (1992) 303-315.

26. M. Ainsworth and A. Craig, A posteriori error estimators in the finite element method, Numer. Math. 60, (1992) 429-463.

27. C. Johnson and P. Hansbo, Adaptive finite element methods in computational mechanics, Comput. Methods Appl. Mech. Engrg. 101, (1992) 143-181,

28. M. Ainsworth and J.T. Oden, A unified approach to a-posteriori error estimation using element residual methods, Numer. Math., 65 (1993) 23-50.

29. R. Durán and R. Rodriguez, On the asymptotic exactness of Bank-Weiser's estimator, Numer. Math. 62 (1992) 297-303.

30. R. Durán, M.A. Muschietti and R. Rodriguez, On the asymptotic exactness of the error estimators for linear triangular elements, Numer. Math. 59, (1991) 107-127.

31. R. Durán, M.A. Muschietti and R. Rodriguez, Asymptotically exact error estimators for rectangular finite elements, SIAM J. Numer. Anal. 29 (1), (1992) 78-88.

32. M.S. Shephard, Q. Niu and P.L. Baehmann, Some results using stress projectors for error indication in: J.E. Flaherty, P.J. Paslow, M.S. Shephard, J.D. Vasilakis, eds., Adaptive Methods for Partial Differential Equations SIAM, Philadelphia (1989) 83-99.

33. T. Strouboulis and K.A. Haque, Recent experiences with error estimation and adaptivity, Part I: Review of error estimators for scalar elliptic problems, Comput. Methods Appl. Mech. Engrg. 97, (1992) 399-436.

34. T. Strouboulis and K.A. Haque, Recent experiences with error estimation and adaptivity, Part II: Error estimation for h-adaptive approximations on grids of triangles and quadrilaterals, Comput. Methods Appl. Mech. Engrg. 100 (1992) 359-430.

35. O.C. Zienkiewicz and J.Z. Zhu, A simple error estimator and the adaptive procedure for practical engineering analysis, Internat. J. Numer. Methods Engrg. 24, (1987) 337-357.

36. O.C. Zienkiewicz and J.Z. Zhu, The superconvergent patch recovery and a posteriori error estimates. Part 1: The recovery technique, Internat. J. Numer. Methods Engrg. 33, (1992) 1331-1364.

37. O.C. Zienkiewicz and J.Z. Zhu, The superconvergent patch recovery and a posteriori error estimates. Part 2: Error estimates and adaptivity, Internat. J. Numer. Methods Engrg. 33 (1992) 1365-1382.

38. N.E. Wiberg and F. Abdulwahab, A posteriori error estimation based on superconvergent derivatives and equilibrium, Internat. J. Numer. Methods Engrg., 36 (1993) 2703-2724.

39. O.C. Zienkiewicz and J.Z. Zhu, The superconvergent patch recovery (SPR) and adaptive finite element refinement, Comput. Methods Appl. Mech. Engrg., 101 (1992) 207-224.

40. O.C. Zienkiewicz, J.Z Zhu and J. Wu, Superconvergent patch recovery techniques. Some further tests, Comm. Numer. Methods Engrg. 9 (1993) 251-258.

41. I. Babuška, R. Durán and R. Rodriguez, Analysis of the efficiency of an a-posteriori error estimator for linear triangular finite elements, SIAM J. Numer. Anal. 29 (4), (1992) 947-964.

42. I. Babuška, L. Plank and R. Rodriguez, Quality assessment of the a-posteriori error estimation in finite elements, Finite Elements in Analysis and Design 11 (1992) 285-306.

43. I. Babuška, L. Plank and R. Rodriguez, Basic problems of a-posteriori error estimation, Comput. Methods Appl. Mech. Engrg. 101 (1992) 97-112.

44. I. Babuška, T. Strouboulis and C.S. Upadhyay, A model study of the quality of a-posteriori estimators for linear elliptic problems, Part Ia: Error estimation in the interior of patchwise uniform grids of triangles, Tech. Note BN-1147, Institute for Physical Science and Technology, University of Maryland (1993).

45. I. Babuška, T. Strouboulis, C.S. Upadhyay, S.K. Gangaraj and K. Copps, Validation of a-posteriori error estimators by numerical approach, Tech. Note BN-1150, Institute for Physical Science and Technology, University of Maryland (1993).

46. V.A. Kondrat'ev, Boundary problems for elliptic equations in domains with conical or angular points, Transactions of the Moscow Mathematical Society (1967) 227-313.

47. I. Babuška, Finite element method for domains with corners, Computing 6 (1970) 264-273.

48. I. Babuška, The rate of convergence for the finite element, SIAM J. Numer. Anal. 8 (2) (1971) 304-315.

49. I. Babuška and M.B. Rosenzweig, A finite element scheme for domains with corners, Numer. Math. 20 (1972) 1-21.

50. I. Babuška, R.B. Kellogg and J. Pitkäranta, Direct and inverse error estimates for finite elements with mesh refinements, Numer. Math. 33 (1979) 447-471.

51. V.A. Kondrat'ev and O.A. Oleinik, Boundary-value problems for partial differential equations in non-smooth domains, Russian Math. Surveys 38(2) (1983) 1-86.

52. P. Grisvard, Elliptic Problems in Nonsmooth Domains (Pitman, London, 1985).

53. B.Q. Guo, The h-p Version of Finite Element Method in Two Dimensions. Mathematical Theory and Computational Experience, Ph.D. Dissertation, Department of Mathematics and Institute for Physical Science Technology, University of Maryland (1985).

54. I. Babuška and B.Q. Guo, Regularity of the solution of elliptic problems with piecewise analytic data. Part I. Boundary value problems for linear elliptic equations of second order, SIAM J. Math. Anal. 19 (1) (1988) 172-203.

55. I. Babuška and B.Q. Guo, Regularity of the solution of elliptic problems with piecewise analytic data. Part II: The trace space and applications to the boundary value problems with non-homogeneous boundary conditions, SIAM J. Math. Anal. 20 (1989) 763-781.

56. B.Q. Guo and I. Babuška, On the regularity of elasticity problems with piecewise analytic data, Tech. Note BN-1136, Institute for Physical Science and Technology, University of Maryland, College Park, 1992.

57. J.A. Nitsche and A.H. Schatz, Interior estimates for Ritz-Galerkin methods, Math. Comp. 28 (1974) 937-958.

58. J. Descloux, Interior regularity and local convergence of Galerkin finite element approximations for elliptic equations in: J.J.H. Miller, ed., Topics in Numerical Analysis II (Academic Press, London, 1975) 27-41.

59. J.H. Bramble, J.A. Nitsche and A.H. Schatz, Maximum-norm estimates for Ritz-Galerkin methods, Math. Comp. 29 (1975) 677-688.

60. A.H. Schatz and L.B. Wahlbin, Interior maximum norm estimates for finite element methods, Math. Comp. 31 (1977) 414-442.

61. A.H. Schatz and L.B. Wahlbin, Maximum norm estimates in the finite element method on plane polygonal domains. Part 1, Math. Comp. 32 (1978) 73-109.

62. A.H. Schatz and L.B. Wahlbin, Maximum norm estimates in the finite element method on plane polygonal domains. Part 2, refinements, Math. Comp. 33 (1979) 465-492.

63. A.H. Schatz, A weak discrete maximum principle and stability of the finite element method in L_∞ on plane polygonal domains, Math. Comp. 34 (1980) 77-91.

64. L.B. Wahlbin, On the sharpness of certain local estimates for $\overset{0}{H}{}^1$ Projections into Finite Element Spaces: Influence of a reentrant corner, Math. Comp. 42 (1984) 1-8.

65. L.B. Wahlbin, Local behavior in finite element methods, in: P.G. Ciarlet and J.L. Lions, eds., Handbook of Numerical Analysis, Vol. II (North-Holland, Amsterdam, 1991) 357-522.

66. I. Babuška and H.-S. Oh, Pollution problem of the p- and h-p versions of the finite element method, Comm. Appl. Numer. Methods 3 (1987) 553-561.

67. J. Peraire, M. Vahdati, K. Morgan and O.C. Zienkiewicz, Adaptive remeshing for compressible flow computations, J. Comp. Phys. 72 (1987) 449-466.

68. O.C. Zienkiewicz, J.Z. Zhu, and N.G. Gong, Effective and practical $h-p$ version adaptive analysis procedures for the finite element method, Internat. J. Numer. Methods Engrg. 28 (1989) 879-891.

The Laboratory for Numerical Analysis is an integral part of the Institute for Physical Science and Technology of the University of Maryland, under the general administration of the Director, Institute for Physical Science and Technology. It has the following goals:

To conduct research in the mathematical theory and computational implementation of numerical analysis and related topics, with emphasis on the numerical treatment of linear and nonlinear differential equations and problems in linear and nonlinear algebra.

To help bridge gaps between computational directions in engineering, physics, etc., and those in the mathematical community.

To provide a limited consulting service in all areas of numerical mathematics to the University as a whole, and also to government agencies and industries in the State of Maryland and the Washington Metropolitan area.

To assist with the education of numerical analysts, especially at the postdoctoral level, in conjunction with the Interdisciplinary Applied Mathematics Program and the programs of the Mathematics and Computer Science Departments. This includes active collaboration with government agencies such as the National Institute of Standards and Technology.

To be an international center of study and research for foreign students in numerical mathematics who are supported by foreign governments or exchange agencies (Fulbright, etc.).

Further information may be obtained from **Professor I. Babuška**, Chairman, Laboratory for Numerical Analysis, Institute for Physical Science and Technology, University of Maryland, College Park, Maryland 20742-2431.